©2014

Julie Kalansky

ALL RIGHTS RESERVED

INTERNAL AND FORCED VARIABILITY OF THE EQUATORIAL PACIFIC ON MILLENIAL AND CENTENNIAL TIME SCALES

By

JULIE KALANSKY

A dissertation submitted to the Graduate School-New Brunswick

Rutgers, The State University of New Jersey

In partial fulfillment of the requirements

For the degree of Doctor of Philosophy

Graduate Program in Oceanography

Written under the direction of

Yair Rosenthal

And approved by

_____

_____

_____

_____

New Brunswick, New Jersey

October 2014

ABSTRACT OF THE DISSERTATION

Internal and Forced Variability of the Equatorial Pacific on

Millennial and Centennial Time Scales

by JULIE KALANSKY

Dissertation Director: Yair Rosenthal

Although the equatorial Pacific (EP) is important to climate on interannual and decadal time scales relatively little is known about its variability and its role in the climate system on longer time scales. The main objectives of this thesis are to examine the centennial and millennial temperature variability of different regions in the EP, to determine the cause of this variability and to understand the impact of this variability on the climate system. The primary temperature proxy used is Mg/Ca from *Neogloboquadrina dutertrei*, a planktonic foraminifera that lives between 75-150 m. Other proxies include alkenone Uk'37 ratios to reconstruct sea surface temperature (SST) and Mg/Ca from benthic foraminifera to reconstruct bottom water temperature. Additionally, $\delta^{18}O$ is used as a temperature and salinity proxy and $\delta^{13}C$ is used as a water mass tracer. Reconstructions are from the eastern equatorial Pacific (EEP) in chapter 2 and 3, and the reconstruction in chapter 4 is from the Indonesian Throughflow (ITF). The second chapter focuses on the entire Holocene and the third and fourth chapters focus on the Common Era.

The primary results from both locations and all timescales suggest the millennial and centennial dynamics are distinct from interannual and decadal dynamics. Prior to 8

kyr B.P. EEP thermostad temperatures are warm which is arguably caused by the Southern Westerly Winds being located farther South. After 8 kyr, thermostad temperatures show millennial and centennial variability, implying that in absence of a strong climate signal from the southern high latitudes, centennial variability in the EEP thermodstad is dominated by intrinsic variability. Intrinsic variability also affects SSTs in the EEP for the last 2,500 as SSTs are not responding solar variability or Northern Hemisphere temperatures. In the ITF, thermocline temperatures vary due to modulations in the regional monsoon. Neither data from the EEP nor ITF indicate that ENSO modulations are influencing centennial variability. The results from both regions caution against using ENSO to explain centennial variability and suggest the role of the EP in the climate system on centennial and longer time scales is more moderate than on interannual to decadal time scales.

Acknowledgements

Foremost, I would like to thank my advisor, Yair Rosenthal. As an advisor he has struck the delicate balance of letting me struggle and make mistakes but never so much that I felt defeated. Through this, I have learned an immense amount and feel that this dissertation is driven by my ideas. He has been incredibly supportive of my decisions both scientifically and personally for which I am extremely grateful. Yair, thank you for all your teaching, mentoring and support over the past 5 years.

My committee members, Tony Broccoli, Rob Sherrell and Gabe Vecchi, have given me ideas of topics to research in order to better explain the significance and relevance of my data. They have also been helpful in ensuring that I have not over interpreted my data. All three are extremely busy, but each member has found time to meet with me regularly and has provided insightful comments and encouragement. For this, thank you.

Several people at IMCS and at EPS have been instrumental in my graduate career and the completion of this project. The Rosenthal lab group has provided an immense amount of scientific and moral support throughout the years. Kat Essswein taught me how to clean and run foraminifera for trace metals. Tali Babila, Stella Woodard, Audrey Morley and I spent countless hours discussing core top calibrations, fixing and maintaining the ICP-MS and providing encouragement and support. Jim Wright, Rick Mortlock and Nicole Abdul helped me run isotope samples and were always available to discuss age models, foraminiferal habitats and size effects, and data quality. I looked forward my trips over to Geology, largely because of these three. Through the Geophysical Data analysis class and by always having their doors open John Wilkin and

Bob Chant taught me how to use Matlab and helped me through several data analysis roadblocks. In addition, Eli Hunter, Aboozar Tabatabai, and Xinzhong Zhang were always willing to help me with Matlab and data analysis questions. Thank you for your patience and willingness to help. I would like to thank Anna Hermes, Cat Beck, Maria Lagerström, Jeana Drake, Mansha Seth-Pasricha, Jack McSweeney, Silke Severman, Kim Thamatrakoln and Becca Barnes for their camaraderie, feedback on presentations and encouragement.

Shai has taught me to be more assertive and has pushed me out of my comfort zone. His sense of humor and enterprising personality have made these past five years a time of exhilaration and enjoyment. Along with that, however, he has consistently given me the support and steadiness that allowed me to reach my goal. He is the perfect husband for me. Thank you, Shai. My family has gently and thoughtfully encouraged me to keep on track and finish strong. Especially in these last few months, my extended family has been pivotal by providing much needed help and favors. Lastly, I would like to thank my mom, whose home science lessons, and example, are likely why I initially became interested in science.

TABLE OF CONTENTS

Page

TABLE OF CONTENTS
(continued)

Page

List of Tables

Lists of Figures

CHAPTER ONE

INTRODUCTION

1.1 Thesis Introduction

The observational record has shown the equatorial Pacific (EP) to have an important role in climate variability on both interannual and decadal time scales. The influence of EP variability extends as far as Europe and Antarctica [*Ding et al.*, 2011; *Hoerling et al.*, 2001] and can have severe impacts on society [*McPhaden et al.*, 2006]. For example, the 1982-1983 El Niño event is estimated to have resulted in over 2,000 deaths and to have cost an estimated $13 billon [*Fagan*, 1999]. Changes in the EP have such far-reaching effects because the equatorial currents transport large amounts of heat and can communicate changes rapidly to other regions of the globe via atmospheric teleconnections [*Alexander et al.*, 2002]. As a consequence, the extent of the heat storage in the EP affects global temperatures [*Roemmich and Gilson*, 2011; *Trenberth et al.*, 2014]. For example, it has recently been argued to be the mechanism responsible for the recent hiatus in global temperature increase [*England et al.*, 2014; *Kosaka and Xie*, 2013; *Meehl et al.*, 2013]. Although the EP is a critical component of the climate system on interannual and decadal timescales, relatively little is known about the EP on millennial and centennial time scales. In reference to the possibility that the region affects centennial and millennial climate change, Pierrehumbert [2000] called the EP a “sleeping dragon” due its large role in heat transport, strong coupling between the ocean and atmosphere and oceanic connection to the Indian Ocean.

Observational and modeling studies suggest that the dynamics of interannual and centennial variability are different. El Niño Southern Oscillation (ENSO) results from coupled ocean-atmosphere feedbacks. Bjerknes [1969] first described the ocean-

atmosphere coupling when he showed that weaker trade winds reduce upwelling and increase sea surface temperatures (SST) in the eastern equatorial Pacific (EEP). Reduced upwelling further weakens the trade winds due to a reduction in the zonal SST gradient producing a positive feedback. Using a relatively simple model, Clement et al. [1996] showed that the Bjerknes feedback functions to cool the EEP during periods of uniformed heating. Her study suggests the strengthening of Pacific zonal SST gradient and atmospheric winds, which reduces the ability of perturbations, such as those associated with ENSO, to change sea-surface temperatures. For example, increased Boreal summer insolation would have shifted the Pacific Intertropical Convergence Zone (ITCZ) northward, increasing cross equator atmospheric flow, equatorial upwelling and cooling the eastern equatorial Pacific which would stabilize the zonal Pacific SST pattern against atmospheric perturbations. However, a more recent study using the ensemble mean from several global climate models (GCM) suggests that the dynamics are different in response to increased greenhouse gases [*DiNezio et al.*, 2009]. Unlike the Clement et al. [1996] study, under enhanced greenhouse gases, the GCM ensemble mean shows that the westerly winds decreased though this did not change the zonal SST gradient. Increased stratification and enhanced vertical mixing in the EEP helped to maintain the SST gradient [*DiNezio et al.*, 2009]. In addition to forced changes in the EP, models have shown the EP to vary due to unforced centennial variability. The unforced EP centennial variability resembles changes that are more similar to ENSO than when forced by greenhouse gases, although the unforced variability causes larger changes in the western equatorial Pacific (WEP) rather than EEP, which is the opposite of ENSO [*Karnauskas et al.*, 2012].

In the WEP heat and fresh water are transported to the Indian Ocean through the Indonesian Throughflow (ITF). This oceanic teleconnection responds and contributes to the EP variability through coupled oceanic and atmospheric feedbacks. Modeling studies tested opened/closed scenarios of the ITF and showed that when the ITF is closed the trade winds relax, the EEP SST increases and the tilt of the thermocline decreases [*Song et al.*, 2007]. In the closed ITF scenario ENSO becomes more energetic and warm events become more frequent [*Song et al.*, 2007]. Additionally, recent observational studies indicate that changes the trade winds affect the transport through the ITF with weaker winds reducing the transport [*Sprintall et al.*, 2009]. The feedback between changes in the ITF and the EP are unclear from observational data at any timescale. In particular, data availability and complex bathymetry has limited studies examining decadal to centennial variability in the ITF.

Equatorial Pacific centennial and millennial variability, specifically of the ITF and EEP, is the focus of this thesis. Studying centennial and millennial timescales is important because it helps differentiate how the climate system, and in this case the tropical Pacific, responds to internal variability and external forcing, such as solar and high latitude climate. In addition to gaining a better understanding of the climate system, studying past climate variability helps to improve our understanding of how increased greenhouse gas emissions may affect the region. Currently, most of our understanding of the EP on centennial and millennial timescales has come from models due to the limited data availability in the region. Observational data only extend to the mid 1800s, requiring the use of proxy records to extend the data farther back in time and under different climate background conditions. Corals have annual resolution and exact dating and thus

constitute an archive of past dynamic changes on annual and inter-annual scales. However, coral records typically only extend for several hundred years. Reconstructions from sediment cores have the possibility of extending back thousands of millennia, but often are limited by low sedimentation rates making it difficult to study centennial and millennial timescales. The data presented in this thesis are unique in that they come from continuous high resolution sediment cores which allow the data to extend several millennia, but also have the resolution to determine centennial scale variability in equatorial Pacific mean climate state. This enables me to begin to address the broad questions of how has the EP varied in past and what is the impact of this variability? To address these questions I will use data from the last 2,000 and 10,000 years.

To study the variability in the EP on these time scales, I use various proxies to reconstruct water column structure. Throughout the thesis, subsurface water column temperature estimates are determined from Mg/Ca ratios in the tests (shells) of foraminifera. Core top and culture studies have shown that the amount of Mg incorporated into the foraminiferal test increases with temperature [*Anand et al.*, 2003; *Elderfield et al.*, 2006; *Mashiotta et al.*, 1999; *Rosenthal et al.*, 1997]. Both benthic (*Uvigerina spp.*) and thermocline dwelling (*Neogloboquadrina dutertrei*) foraminifera are used to reconstruct different depths in the water column. SST reconstructions are from alkenone Uk'37 measurements. Coccolithophores, a type of phytoplankton algae that lives in the euphotic zone, produce alkenones, and organic compound (ketone) in which the degree of unsaturation of the alkenone (2 or 3 double bonds in the hydrocarbon chain) is dependent upon temperature. The degree of unsaturation increases when the temperature is colder [*Prahl et al.*, 1988]. In addition, the $\delta^{18}O$ of the foraminifera is also

used to approximate changes in temperature and salinity and the $\delta^{13}C$ is used here as a water mass tracer. Reconstructions from multiple depths enable an analysis of the distribution of heat within the water column and coupling between the different depths.

As mentioned previously, the heat storage in the tropical Pacific has large implications for global temperatures on interannual and decadal time scales. By reconstructing subsurface temperatures in the first two chapters I examine potential links between the heat storage in the EEP and regional and global climate variability. Recently Indo-Pacific-Warm-Pool (IPWP) intermediate water temperatures from the Holocene suggest that on millennial timescales, subsurface temperature varies more than surface temperatures helping to mitigate the effects of changes in the climate system [*Rosenthal et al.*, 2013]. EEP temperature data from the water mass below the thermocline, referred to as the thermostad or 13˚C Water, are used in Chapter 3 to determine if the thermostad plays a similar role in heat storage and address the origin of this temperature change. The third chapter of the thesis looks at changes in SST and subsurface (~125 m) temperatures in the EEP to determine if centennial variability corresponds to Northern Hemisphere (NH) temperature anomalies, particularly the Little Ice Age. If so, this would indicate that the EP may also be important to global temperature on centennial time scales as it has been shown to be on shorter time scales [*England et al.*, 2014; *Roemmich and Gilson*, 2011].

ENSO dynamics are often used as an analog for describing variability that occurs on centennial and millennial time scales, however, models suggest this is not necessarily appropriate [*DiNezio et al.*, 2010; *DiNezio et al.*, 2009]. Tierney et al. [2010] use precipitation records from the Indo Pacific Warm Pool (IPWP) to argue that shifts in the

location of the ITCZ rather than ENSO are primarily responsible for the variability. In Chapter 4, subsurface temperature data from the EEP and in Chapter 5 thermocline water temperature data from the ITF are compared to ENSO reconstructions to determine if variability in these records could be explained by ENSO modulations. Both these chapters address the question; can ENSO modulations explain centennial scale climate variability in the tropical Pacific?

The relative importance of internal variability versus externally forced changes in the tropical Pacific, particularly the EEP, is unclear [*DiNezio et al.*, 2013; *Hoerling et al.*, 2010]. The observational record has shown the EEP undergoes rather large transitions, such as in 1976/77, that are not associated with any particular climate forcing, such as a volcano. Such events indicate that the EEP is susceptible to large changes due to internal variability, meaning it is intrinsic to the dynamics of the EP. Although not the focus, data from Chapter 3 show multicentennial variability that cannot be linked to any climate events, suggesting the importance of internal variability in this region. Chapter 4 addresses this more directly by comparing the SST and subsurface data to NH climate, volcanic and solar variability. Similar to Chapter 4, Chapter 5 compares ITF thermocline water temperatures to NH temperatures, the regional monsoon systems, and solar variability as potential causes of changes in thermocline water temperatures in the ITF. The importance is to determine the extent to which temperatures can vary as a result of internal dynamics. This provides a better understanding of what changes in the EP may be a result of anthropogenic change.

The common theme throughout the thesis is to understand millennial and centennial variability of the EP through the use of temperature proxies. The various

chapters examine different time scales and different regions. The data are analyzed to determine the importance of heat storage in the EEP (Chapters 3 and 4). Chapters 4 and 5 study the relationship between ENSO and centennial variability. Finally all of the chapters address the question of forced versus internal variability. The thesis provides answers to several of the proposed questions concerning variability in the EP, all of which suggest distinct mechanistic differences between centennial to millennial time scales and interannual to decadal time scales.

1.2 References

Alexander, M. A., et al. (2002), The Atmospheric Bridge: The Influence of ENSO Teleconnections on Air-Sea Interaction over the Global Oceans, *Journal of Climate*, *15*(16), 2205-2231.

Anand, P., et al. (2003), Calibration of Mg/Ca thermometry in planktonic foraminifera from a sediment trap time series, *Paleoceanography*, *18*(2).

Bjerknes, J. (1969), Atmospheric Teleconnections from the Equatorial Pacific *Monthly Weather Review*, *97*(3), 163-172.

Clement, A. C., et al. (1996), An ocean dynamical thermostat, *Journal of Climate*, *9*(9), 2190-2196.

DiNezio, P., et al. (2010), Reconciling Differing Views of Tropical Pacific Climate Change, *Eos, Transactions American Geophysical Union*, *91*(16), 141-142.

DiNezio, P. N., et al. (2009), Climate Response of the Equatorial Pacific to Global Warming, *Journal of Climate*, *22*(18), 4873-4892.

DiNezio, P. N., et al. (2013), Detectability of Changes in the Walker Circulation in Response to Global Warming, *Journal of Climate*, *26*(12), 4038-4048.

Ding, Q., et al. (2011), Winter warming in West Antarctica caused by central tropical Pacific warming, *Nature Geoscience*, *4*(6), 398-403.

Elderfield, H., et al. (2006), Calibrations for benthic foraminiferal Mg/Ca paleothermometry and the carbonate ion hypothesis, *Earth and Planetary Science Letters*, *250*(3-4), 633-649.

England, M. H., et al. (2014), Recent intensification of wind-driven circulation in the Pacific and the ongoing warming hiatus, *Nature Clim. Change*, *4*(3), 222-227.

Fagan, B. (1999), *Floods, Famine and Emperors; El Nino and the Fate of Civilizations*, Basic Books, New York.

Hoerling, M., et al. (2010), Regional Precipitation Trends: Distinguishing Natural Variability from Anthropogenic Forcing, *Journal of Climate*, *23*(8), 2131-2145.

Hoerling, M. P., et al. (2001), Tropical Origins for Recent North Atlantic Climate Change, *Science*, *292*(5514), 90-92.

Karnauskas, K. B., et al. (2012), A Pacific Centennial Oscillation Predicted by Coupled GCMs, *Journal of Climate*, *25*(17), 5943-5961.

Kosaka, Y., and S. P. Xie (2013), Recent global-warming hiatus tied to equatorial Pacific surface cooling, *Nature*, *501*(7467), 403-+.

Mashiotta, T. A., et al. (1999), Glacial-interglacial changes in Subantarctic sea surface temperature and d18O-water using foraminiferal Mg, *Earth and Planetary Science Letters*, *170*(4), 417-432.

McPhaden, M. J., et al. (2006), ENSO as an integrating concept in Earth science, *Science*, *314*(5806), 1740-1745.

Meehl, G. A., et al. (2013), Externally Forced and Internally Generated Decadal Climate Variability Associated with the Interdecadal Pacific Oscillation, *Journal of Climate*, *26*(18), 7298-7310.

Pierrehumbert, R. T. (2000), Climate change and the tropical Pacific: The sleeping dragon wakes, *Proceedings of the National Academy of Sciences of the United States of America*, *97*(4), 1355-1358.

Prahl, F. G., et al. (1988), Further Evaluation of Long-Chain Alkenones as Indicators of Paleoceanographic Conditions, *Geochimica Et Cosmochimica Acta*, *52*(9), 2303-2310.

Roemmich, D., and J. Gilson (2011), The global ocean imprint of ENSO, *Geophys. Res. Lett.*, *38*(13), L13606.

Rosenthal, Y., et al. (1997), Temperature control on the incorporation of magnesium, strontium, fluorine, and cadmium into benthic foraminiferal shells from Little Bahama Bank: Prospects for thermocline paleoceanography, *Geochimica Et Cosmochimica Acta*, *61*(17), 3633-3643.

Rosenthal, Y., et al. (2013), Pacific Ocean Heat Content During the Past 10,000 Years, *Science*, *342*(6158), 617-621.

Song, Q., et al. (2007), The role of the Indonesian Throughflow in the Indo-Pacific climate variability in the GFDL Coupled Climate Model, *Journal of Climate*, *20*(11), 2434-2451.

Sprintall, J., et al. (2009), Direct estimates of the Indonesian Throughflow entering the Indian Ocean: 2004-2006, *Journal of Geophysical Research-Oceans*, *114*.

Tierney, J. E., et al. (2010), Coordinated hydrological regimes in the Indo-Pacific region during the past two millennia, *Paleoceanography*, *25*(1), PA1102.

Trenberth, K. E., et al. (2014), Earth's Energy Imbalance, *Journal of Climate*, *27*(9), 3129-3144.

CHAPTER TWO

EXPANDED METHODS SECTION

2.1 Introduction

Although each chapter includes its own methods section, this chapter will expand on those methods and explain why certain core locations were used and certain decisions about what data to present in the dissertation were made.

2.2 Coring Process

The cores in this dissertation are from two different research cruises. The cores from the Eastern Equatorial Pacific (EEP) were taken on aboard the Knorr on a research cruise in the early spring of 2009. The research cruise gathered cores from the Peru Margin to the Galapagos. The Indonesian Throughflow (ITF) cores were taken aboard an Indonesian ship, the Baruna Jaya VIII, in 2003. The cruise was within the ITF and collected cores in the Makassar Straight, Java Sea and the Flores Sea.

In both locations, the EEP and in the ITF the cores were taken near the coast. The proximity to the coast increases the sedimentation rate because terrigenious sediment is transported via rivers. High sedimentation rate cores (with ~100cm/1ky sedimentation rates) are necessary to document the Common Era (CE).

In order to compile a continuous record, records from multiple cores are spliced together. Multi-cores enter the sediment without much impact and preserve the sediment water interface. Gravity cores have a larger weight on top and typically impact the surface sediment, but preserve the top couple of meters. For the ITF record (Chapter 5) only a multi-core and gravity core were taken, and unfortunately there is no overlap in the age model causing a gap in the record. In the EEP an additional long piston core was

taken. Long cores are able to recover several meters of sediment to potentially extend records much farther in time. However, often times long cores are missing the top layers of sediment due to the extreme force on impact. For Chapter 4, the cores located in the EEP were spliced together by using the complete multi-core and then using data from the gravity core once the multicore ended. The end of the multi-core was determined by a radiocarbon date.

2.3 Proxy Records

The choice of the proxy records presented here was primarily based upon the availability of foraminifera and calibrations. Initially, for sea surface temperature (SST) in the EEP I anticipated using both alkenones and the Mg/Ca of a surface dwelling foraminifera. However, in the sediment from the EEP, there were not abundant surface dwelling foraminifera, including *Globigerinoides ruber*, *Globigerinoides sacculifer*, and the upwelling species *Globigerina bulloides*, to produce a continuous Mg/Ca SST record. Surface dwelling foraminifers were more common in the EEP cores prior to 6 kyr possibly due to an increase of advected nutrient rich water to the region [*Faul*, 2000]. SST reconstructions do not suggest cooler temperature which is associated with upwelling. Because of the reduced number of surface dwellers, a Mg/Ca SST record could not be generated. A Holocene alkenone SST record has been generated, however, it will be part of a manuscript by a different author and thus is not included in this dissertation. Instead I referrer to the published SST record of Chazen et al. [2009] which is slightly farther south (11˚S) along the Peru Margin, but is in the region where the subsurface water upwells.

Various different benthic foraminifera were indentified with the possibility that they could be used to reconstruct bottom water temperature. However, the only other

benthic foraminifera that was continuous and abundant throughout the core besides *Uvigerina,* was *Cassidulina subglobosa*. A core top calibration of *C. subglobosa*, from the EEP and the ITF showed the sensitivity of the Mg/Ca ratio to temperature is low (m=0.0032), indicating that generating a temperature record would be difficult. A Mg/Ca and isotope record for *Uvgerina* from the EEP was generated for the last 2,000 years. During this period forcings are relatively small suggesting that the temperature variability would be small as well. The *Uvigerina* temperature estimates and the $\delta^{18}O$ values do not parallel each other, nor did the *C. subgloboa* and *Uvigerina* Mg/Ca values, suggesting that variability internal to the proxy temperature was greater than the temperature signal.

2.4 Trace Metal Analysis

The foraminifera were cleaned according the method outlined in Baker et al. 2003 with the reductive cleaning as described by Boyle and Keigwin [1985] and modified by Boyle and Rosenthal [1996]. The samples were dissolved in 100 uL of 0.0065 M HNO3 and diluted with 300 uL of 0.5 N HNO3, such that the final calcium concentrations ranged between 2.5-5.5 mmol.

Trace metal ratios were determined at Rutgers University, using a Thermo Finnigan Element XR sector-field inductively couple mass spectrometer (ICP-MS). The samples were introduced into the ICP-MS through a self-aspirating introduction system, which included a cyclonic quartz spray chamber with the addition of anhydrous ammonia gas at a rate of approximately 7 mL/min. The ammonia gas was used to reduce the memory effect of boron in order to make accurate B/Ca measurements [*Al-Ammar et al.*, 2000]. Although B/Ca measurements will not be discussed here, they may be used at a later date. In addition to Mg/Ca ratios, several other element ratios were measured, including Al/Ca, Fe/Ca, Mn/Ca and Ti/Ca, to monitor possible contamination from

oxides and silicates. All previously mentioned elements were measured in low resolution (Δm/M=300) except Fe/Ca, which was measured in medium resolution (Δm/m=4000) to avoid the large ArO interference on Fe56.

Several corrections were made to the samples in order to calculate the final trace metal ratios. Each element was blank corrected [*Rosenthal et al.*, 1999] and ratios were calculated online using the ICP-MS software (version 2.0). Offline, although minor, the interference of $Sr86^{++}$ on Ca43 values was corrected by using $Sr87^{++}$. Samples were then converted into mmol/mol ratios and drift corrected using a spiked gravimetric standards, which has a Mg/Ca value of 6.34 mmol/mol [*Andreasen et al.*, 2006]. Because the samples had different concentrations of Ca, the samples were also matrix corrected. The spiked gravimetric standard was diluted to various Ca concentrations ranging between 1.5 mmol and 8 mmol Ca to determine how element ratios change with Ca concentrations. A best fit linear or logarithmic line for each trace metal ratio was fit and used to correct for any offsets due to calcium concentrations. The Mg/Ca matrix correction was always less than 2% of the original value. The long term precision of the data was based upon the replication of three in house consistency standards from 2011 with Mg/Ca values of 1.44 mmol/mol (CS1), 3.49 mmol/mol (CS2), and 8.71 mol/mol (CS3). For the time period of the data generated presented in this thesis, the standard deviations were 0.83%, 0.71% and 0.66% respectively (Figure 2-1). Samples were eliminated if the Mn/Ca, Fe/Ca, or Al/Ca were above the 100 umol/mol threshold indicating likely contamination [*Barker et al.*, 2003]. Additionally, if any of the aforementioned element ratios were 2 sigma higher than other samples in the run, the sample was also eliminated because of the potential influence of contamination on the Mg/Ca values.

2.5 References

Al-Ammar, A. S., et al. (2000), Elimination of boron memory effect in inductively coupled plasma-mass spectrometry by ammonia gas injection into the spray chamber during analysis, *Spectrochimica Acta Part B-Atomic Spectroscopy*, *55*(6), 629-635.

Andreasen, D. H., et al. (2006), Fidelity of radially viewed ICP-OES and magnetic-sector ICP-MS measurement of Mg/Ca and Sr/Ca ratios in marine biogenic carbonates: Are they trustworthy together?, *Geochemistry Geophysics Geosystems*, *7*.

Barker, S., et al. (2003), A study of cleaning procedures used for foraminiferal Mg/Ca paleothermometry, *Geochemistry Geophysics Geosystems*, *4*.

Boyle, E., and Y. Rosenthal (1996), Chemical Hydrography of the South Atlantic During the Last Glacial Maximum: Cd vs. d13C, in *The South Atlantic*, edited, pp. 423-443, Springer Berlin Heidelberg.

Boyle, E. A., and L. D. Keigwin (1985), Comparison of Atlantic and Pacific paleochemical records for the last 215,000 years: changes in deep ocean circulation and chemical inventories, *Earth and Planetary Science Letters*, *76*(1-2), 135-150.

Chazen, C. R., et al. (2009), Abrupt mid-Holocene onset of centennial-scale climate variability on the Peru-Chile Margin, *Geophysical Research Letters*, *36*.

Faul, K. L., A. Christina Ravelo, M. L. Delaney (2000), Reconstructions of upwelling, productivity, and photic zone depth in the eastern equatorial Pacific Ocean using planktonic foraminiferal stable isotopes and abundances, *The Journal of Foraminiferal Research*, *30.2*, 110-125.

Rosenthal, Y., et al. (1999), Precise determination of element/calcium ratios in calcareous samples using sector field inductively coupled plasma mass spectrometry, *Analytical Chemistry*, *71*(15), 3248-3253.

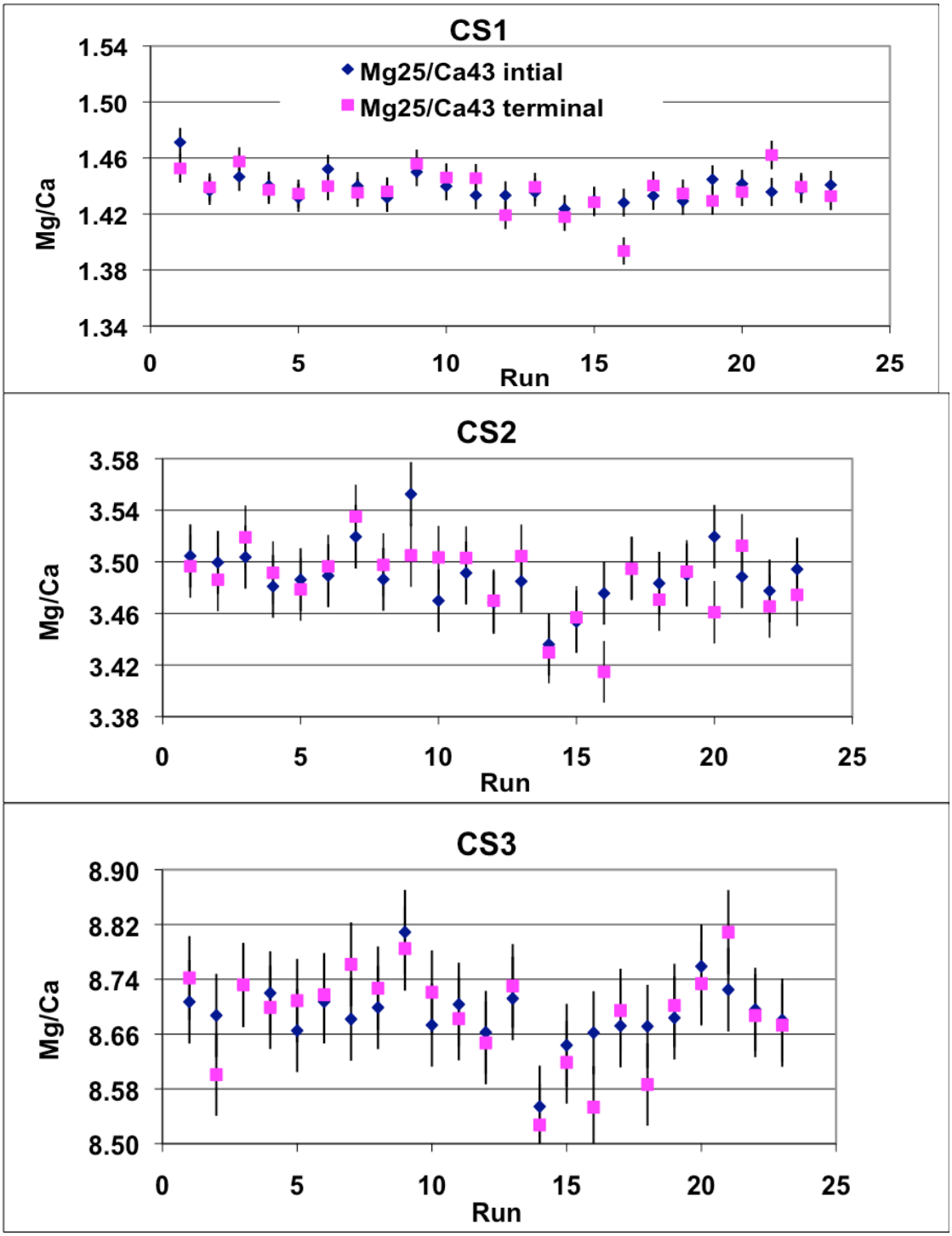

Figure 2-1. For each run from throughout the duration of this dissertation, the initial (blue diamonds) and terminal (pink squares) consistency standard 2011 Mg/Ca values are

plotted. The error bars represent the standard deviation, which are 0.74%, 0.70% and 0.66% for CS1, CS2, CS3 respectively.

CHAPTER THREE

SOUTHERN OCEAN LINKS TO THE EASTERN EQUATORIAL PACIFIC THERMOSTAD DURING THE HOLOCENE

3.1 Abstract

Temperature reconstructions from a shallow core (375 m) from the Peru Margin are used to test the influence of Subantarctic Mode Water (SAMW) on the eastern equatorial Pacific thermostad and the effect of southern high latitude climate on interior ocean heat content. The Mg/Ca temperature estimates, based on planktonic and benthic foraminifera (*Neogloboquadrina dutertrei* and *Uvigerina spp.*, respectively) show higher temperatures in the early Holocene followed by a cooling of ~2° by 8 kyr. The temperature signal is similar in direction and timing to a rather robust Holocene climate signal from the southern high latitudes suggesting it originated there and was advected to the core site. Based on the *N. dutertrei* and *Uvigerina* $\delta^{13}C$ records and that the origin of the thermostad has been previously traced to SAMW, we conclude that SAMW acted as a conduit transporting the southern high latitude climate to the interior of the equatorial Pacific. We propose the early Holocene warmth is related to a southward migration of the Subtropical Front, which enabled greater influence of warm subtropical waters to the region of SAMW formation. The SAMW temperature signal was then transported to the thermostad in the equatorial Pacific. The subsurface temperature signal in the equatorial Pacific appears to be larger than the surface temperature expression in the cold tongue, indicating that the proposed mechanism may be important for sequestering heat in the ocean interior.

3.2 Introduction

Interior ocean heat content (OHC) is an important component of the climate system as it sequesters excess energy and mitigates the effects of a changing climate [*Levitus et al.*, 2012], The mechanisms and locations by which the heat enters and spreads in the ocean interior remain an active area of research [*Balmaseda et al.*, 2013]. Strengthening of equatorial trade winds has been argued to increase OHC [*England et al.*, 2014; *Kosaka and Xie*, 2013] as have changes in the Atlantic Meridional Overturning Circulation [*Balmaseda et al.*, 2013]. In addition to these observational studies, modeling studies suggest that the Southern Ocean is important in controlling OHC due to the outcropping of intermediate and deep isopycnal layers that transport water into the interior ocean [*Cai et al.*, 2010; *Gregory*, 2000]. The impact of the Southern Ocean on OHC might be particularly relevant on centennial and longer time scales because the response of density structures is long due to the coupling with changes in northern high latitudes [*Jones et al.*, 2011]. Supporting the influence of the Southern Ocean on OHC on millennial timescales, a recent study by Rosenthal et al. [2013] argues that Holocene changes in Pacific OHC originated both in the northern and southern high latitudes. The evidence for a link to the Southern Ocean is, however, tenuous.

A rather robust change of southern high latitude climate during the early Holocene allows us to test the extent of the influence of the Southern Ocean on Pacific OHC on centennial and longer time scales. Several different reconstructions suggest that the southern high latitudes were warmer prior to 8 kyr B.P. Sea surface temperature (SST) records from the southwest Pacific show warmer temperatures during the early Holocene which cooled by 8 kyr [*Luer et al.*, 2009; *Pahnke and Sachs*, 2006; *Sikes et al.*, 2002; *Sikes et al.*, 2009]. The increased SST has been attributed to a more poleward

location of the Subtropical Front [*Bostock et al.*, 2013; *Luer et al.*, 2009; *Marr et al.*, 2013; *Moros et al.*, 2009; *Sikes et al.*, 2002]. The southern position of the Subtropical Front was likely a basin wide adjustment as SST on the eastern side of the Pacific, at 41˚S, also show a similar temperature trend [*Kaiser et al.*, 2005]. The early Holocene warmth has also been documented further south in the Atlantic sector of the Southern Ocean and near the West Antarctic Peninsula [*Bianchi and Gersonde*, 2004; *Shevenell et al.*, 2011]. Ice core $\delta^{18}O$ reconstructions of Antarctic air temperatures also show warmer temperatures between ~11-10 kyr and cooling by ~8.5 kyr [*Masson-Delmotte et al.*, 2011; *Mulvaney et al.*, 2012], and records from southern Chile indicate decreased precipitation around 8 kyr likely reflecting SST cooling [*Lamy et al.*, 2010]. In summary, the early Holocene is associated with increased Antarctic and Southern Ocean temperatures, a more poleward position of the Subtropical Front and greater precipitation in the Chilean Fjords. These early Holocene changes have variably been attributed to orbital forcing [*Masson-Delmotte et al.*, 2011; *Shevenell et al.*, 2011] changes in the intensity and location of the southern westerly winds (SWW) [*Lamy et al.*, 2010; *Moros et al.*, 2009; *Shevenell et al.*, 2011], and the bipolar seesaw [*Lamy et al.*, 2010; *Stenni et al.*, 2011].

For changes in the southern high latitude to enter the ocean intermediate waters and affect low latitude ocean heat content of the upper 700 m, the signal would have to propagate via Subantarctic Mode Water (SAMW) or Antarctic Intermediate Water (AAIW). Compared to AAIW, SAMW is shallower and less dense and is the focus is the focus of this paper. SAMW is the northern most Southern Ocean water mass that is subducted into the ocean interior and transports heat, salinity, nutrients and CO_2, from the southern high latitudes equatorward [*Banks and Bindoff*, 2003; *Sabine et al.*, 2004;

Sarmiento et al., 2004]. SAMW forms in the Southern Ocean north of the Subantarctic Front [*Hartin et al.*, 2011] during the winter when mixed layers can exceed 400 m [*Dong et al.*, 2008; *Hanawa and Talley*, 2001].

In the Pacific, Argo float data indicate SAMW temperature and salinity signals extend as far north as 30˚S [*Herraiz-Borreguero and Rintoul*, 2011], whereas $\Delta^{14}C$ and $\delta^{13}C$, the more conservative tracers, suggest SAMW reaches the equator [*Spero and Lea*, 2002; *Toggweiler et al.*, 1991]. The carbon isotope data are supported by a model tracer experiment which shows that SAMW is the origin of equatorial Pacific subsurface (~150-300 m) water mass [*Qu et al.*, 2009]. This water mass is referred to as the 13˚C Water and is more broadly defined as the Equatorial Pacific thermostad [*Tsuchiya*, 1981]. The difference between the Argo float and the carbon isotope data is likely because temperature is an active tracer, meaning it affects the fluid properties, whereas the carbon isotope ratio is a passive tracers. However if a SAMW temperature signal were sufficiently strong, the carbon isotopes imply it could reach the thermostad impacting the interior OHC in the equatorial region. Here we use sediment cores from the eastern equatorial Pacific to test the hypotheses that SAMW is the origin of the thermostad and that SAMW is a major conduit of southern high latitude climate to the equatorial Pacific. Based on the previous reconstructions, if these hypotheses are true, then the reconstructed thermostad should be warmer prior to 8 kyr B.P.

3.3 Geological and oceanographic setting

Reconstructions are from KNR 195-5 CDH23, a giant piston core, recovered from the Peru Margin (3˚45'S, 81˚08'W, 374 m water depth). The Peru Margin shelf slope is approximately 60 km wide, extends to a depth of about 400 m and bounded by a steep

slope with a gradient of ~70 m per kilometer (Figure 3-1) [*Ryan et al.*, 2009]. The reconstructions are based on *Neogloboquadrina dutertrei*, a thermocline dwelling planktonic foraminifer and *Uvigerina spp.*, an infaunal benthic foraminifer. In the EEP, *N. dutertrei* calcifies between 75-150 m, which is below the shallow thermocline [*Rincon-Martinez et al.*, 2011]. *Uvigerina* is usually found in the first 1-2 cm of the sediment [*McCorkle et al.*, 1997], such that it records bottom water temperature. The σ_θ values of the two water masses being reconstructed are 26.1 and 26.7 kg/m^3, for *N. dutertrei* and *Uvigerina* respectively, and are associated with the density surface just above and below the thermostad.

The equatorial Pacific thermostad is a depth interval of relatively uniform temperature below the EUC [*Lukas*, 1986]. It has been defined as the water mass between approximately 5˚N to 5˚S with a temperature range between 11-14˚C and it lies between the σ_θ values of 26.2-26.65 kg/m^3 [*Tsuchiya*, 1981]. The thermostad is bounded to the north and south by the subsurface counter currents (SSCC) with the thermostad becoming wider and thicker in the east. In the west the thermostad is found between ~225-275 m whereas in the east it is between ~150-300 m (Figure 3-2). The formation and the thickening of the thermostad has been attributed to the mixing at the base of the EUC, due to the high shear from the current [*Toggweiler et al.*, 1991] and through diapycnal fluxes along the SSCC [*Rowe et al.*, 2000]. Mixing of warmer water along the EUC explains how higher density SAMW (σ_θ = 26.9–27.15 kg/m^3) can be transformed into the warmer, less dense water of the thermostad [*Toggweiler et al.*, 1991].

The pathway of SAMW from the Southern Ocean to the EEP is likely via the New Guinea Coastal Undercurrent (NGCUC). In the Pacific basin, once SAMW subducts

it travels northwestward with some SAMW reaching the Solomon Sea near Papua New Guinea [*Herraiz-Borreguero and Rintoul*, 2011]. From there it likely enters the New Guinea Coastal Undercurrent. This is also supported by adjoint tracer model experiments which show that the thermostad originated in SAMW formation regions but enters the equatorial region through the Western Boundary Currents [*Qu et al.*, 2009]. The water then travels eastward across the equatorial pacific to reach the EEP.

3.4 Methods

3.4.1 Age Model

The age model for CDH23 is based on 17 radiocarbon dates from *N. dutertrei* (Table 3-1) and converted to calendar age using a reservoir age of 500 years and the Fairbank et al. [2005] calibration. The average sedimentation rate for the core is about 100 cm/kyr (Figure 3-3) and it was sampled at 8cm, ~80 year, intervals. All ages in the chapter are thousand years before present (B.P.), which is considered 1950.

3.4.2 Analysis

Between 15-20 tests of *N. dutertrei* from 355-425μm size fraction and 10-15 *Uvigerina spp*. specimens from greater 200 μm were split for isotope and trace metal analysis. However, *Uvigerina* abundance decreased between 600-750 cm in the core only permitting either trace metal or isotope measurements due to limited material. For trace metal analysis, foraminifera were cleaned according the method outlined in Barker et al. [2003] with the reductive cleaning of Rosenthal et al. [1997]. The samples were dissolved in 100 μL of 0.065 M HNO_3 and diluted with 300 μL of 0.5 N HNO_3, such that the final calcium concentrations ranged from 1-5 mM.

Trace metal ratios were determined at Rutgers University, using a Thermo Finnigan Element XR sector-field inductively coupled plasma mass spectrometer (ICP-

MS). In addition to Mg/Ca ratios we measured Al/Ca, Fe/Ca, Mn/Ca and Ti/Ca, to monitor possible contamination from oxides and silicates. The raw data were corrected for the interference of Sr^{86++} on Ca^{43}, matrix effects [*Andreasen et al.*, 2006] and instrumental drift [*Rosenthal et al.*, 1999]. The Mg/Ca matrix correction was always less than 2% of the original value. Samples were then converted into mmol/mol ratios and drift corrected using a spiked gravimetric standard, which has a Mg/Ca value of 6.34 mmol/mol [*Rosenthal et al.*, 1999]. The long term precision of the data was based upon the replication of three in house consistency standards with Mg/Ca values of CS1: 1.44 mmol/mol, CS2: 3.49 mmol/mol, and CS3: 8.71 mol/mol. For the time period of the data presented here, the standard deviations were 0.83%, 0.71% and 0.66% respectively. Samples were eliminated if the Mn/Ca, Fe/Ca, or Al/Ca were above the 100 µmol/mol threshold indicating likely contamination [*Barker et al.*, 2003]. Additionally, if any of the aforementioned elemental ratios were 2 sigma higher than other samples in the run, the sample was also eliminated because of the potential influence of contamination on the Mg/Ca values. Based on these criteria 2 *Uvigerina* samples and no *N. dutertrei* samples were excluded.

Carbon and isotope analyses were preformed at Rutgers University on a Micromass (FISONS) Optima Isotope Ratio Mass Spectrometer. The samples were drift corrected if necessary using an in house standard. The standard is run against the international NBS19 [*IUPAC*, 1994] biannually. Throughout all the runs the standard deviation was ±0.05‰ for $\delta^{13}C$ and ±0.1‰ for $\delta^{18}O$. Isotope values are reported in PDB. The $\delta^{18}O$ of calcite was corrected for sea level by fitting a polynomial to coral sea level data from [*Bard et al.*, 1996; *Bard et al.*, 2010; *Fairbanks*, 1990; *Lighty et al.*, 1982;

Peltier and Fairbanks, 2006] and then assuming a 0.1‰ change in $\delta^{18}O$ per 10 meters of sea level change [*Fairbanks and Matthews*, 1978]. Assuming no change in $\delta^{18}O_{sw}$ other than due to ice volume, using the Shackleton and Vincent [1978] equation and the standard deviation of the standards, the temperature error of $\delta^{18}O_c$ is ±0.4˚C.

3.4.3 Temperature Calibrations

Subthermocline temperature was estimated from Mg/Ca of *N. dutertrei* using the multi-species planktonic calibration from Anand et al. [2003]. This calibration was used because it calculates the most realistic temperatures based on core top analysis of *N. dutertrei* in the region (Figure 3-4). Discrete $\delta^{18}O$ of seawater ($\delta^{18}O_{sw}$) measurements from a CTD cast conducted during the coring cruise were converted to $\delta^{18}O$ of carbonate ($\delta^{18}O_c$) values using the Shackleton and Vincent [1978] equation. The core top $\delta^{18}O_c$ values of the *N. dutertrei* were then compared to the calculated water $\delta^{18}O_c$ values to estimate the calcification depth of *N. dutertrei*, which was determined to be between 100 and 130 m (Figure 3-4). This is slightly shallower than the top of the thermostad. The Anand et al. [2003] multi species calibration calculates a temperature of 14.7±1.3 (SE)˚C, which includes standard error from the core top measurements and the error associated with the calibration (Appendix 3-1). The core top determined temperature is within the measured modern temperature range at these depths (14-15˚C) [*Locarnini*, 2010]. The error in the downcore temperature anomaly estimates is reduced to ±1.1˚C because it only incorporates the error on the slope of the calibration and using a three point running average further reduces the error on the temperature anomaly to ±0.8˚C (Appendix 3-1).

Uvigerina core top calibrations provide a range of sensitivities as reviewed in Bryan and Marchitto [2008]. All the available calibrations produce temperatures that are

2-6˚C colder than the bottom water temperature at the core site. Different regional core top studies produce different calibrations [*Bryan and Marchitto*, 2008; *Elderfield et al.*, 2006, unpublished data] suggesting that a regional calibration is optimal when estimating temperatures from Mg/Ca of *Uvigerina*. Because there are insufficient cores tops from the Peru Margin to produce a regional calibration, we used the linear calibration from Bryan and Marchitto [2008] (Mg/Ca = (0.7±0.05) + (0.084±0.005)*T) and adjusted the intercept to fit the bottom water temperature. This calibration was chosen because it is a compilation of much of the published core top data. The intercept was adjusted to 0.26. This value was used because it calculates an average temperature for the last 100 years that matches the bottom water temperature at the core site of 10˚C. Similar to the *N. dutertrei* calibration, the intercept is only significant in the estimates of the absolute temperature, not the temperature anomaly. The standard error associated with the *Uvigerina* temperature estimates is ± 1.8˚C, the error of the temperature anomaly is ± 1.6˚C and the error of the 3-point running average smoothed data is ± 1.1˚C. The errors are calculated using the standard error from the calibration as well as the core top measurements. The *Uvigerina* temperature estimates were corrected for sea level change using an approximated temperature gradient of 1˚C per 60 m based on temperature profiles from the cruise. This corrects for the assumption that as sea level increased throughout the Holocene, the benthic temperature would decrease solely due to the core becoming deeper. Most of the Mg/Ca temperature estimates are coherent with changes in sea level corrected $\delta^{18}O_c$ (Figure 3-5), supporting the sign and timing of the *Uvigerina* Mg/Ca determined temperature variations.

3.5 Results

Both the *Uvigerina* and *N. dutertrei* records show warmer temperatures prior to 8 kyr (Figure 3-5). Between 10.7 and 9 kyr the *N. dutertrei* temperature varies between 15 and 17˚C. The temperature decreases relatively rapidly to 14˚C by 8.8 kyr and then continues to decrease to approximately 13˚C by 8 kyr. From 8 kyr to the end of the record multicentennial temperature variability is between 12 and 15˚C. A spectral analysis of the temperature record between from 8 kyr and the top of the core does not indicate any significant periodicities. The sea level corrected $\delta^{18}O_c$ values vary between 0.5 and 0.3‰ from 10-9 kyr and become more enriched to 0.8‰ by 8.8 kyr indicating warmer and/or fresher thermostad waters in the early Holocene. The Mg/Ca estimated temperature change from 10-8 kyr is approximately 2.5 ±0.8˚C, whereas, assuming there is no change in the $\delta^{18}O_{sw}$, the $\delta^{18}O_c$ indicate about a 1.3±0.4˚C temperature change. The difference between the $\delta^{18}O_c$ and Mg/Ca temperature estimates suggests lower $\delta^{18}O_{sw}$ and implies decreased salinity.

Uvigerina determined bottom water temperature from 10.7-9 kyr varies between 11.5and 12.5˚C and decreases rapidly to 10.5˚C by 8.8 kyr. For the remainder of the record the *Uvigerina* temperature varies from 9.5-11.5˚C. Between 9.3 and 8.8 kyr the sea level corrected *Uvigerina* $\delta^{18}O_c$ becomes more enriched from 1.5 to 1.8‰ indicating a 1.3˚±0.4˚C decrease in temperature assuming there is no change in $\delta^{18}O_{sw}$ other than ice volume during this time (Figure 3-5). The Mg/Ca estimates a 2 ±1.1˚C which is within the error of the ice-volume corrected $\delta^{18}O_c$ estimate.

The $\delta^{13}C$ of *Uvigerina* and *N. dutertrei* increase during the Holocene (Figure 3-5). The $\delta^{13}C$ of *N. dutertrei* increases from ~1 to 1.4‰ and the *Uvigerina* $\delta^{13}C$ increases

from -0.4 to 0.1‰ by 6 kyr. During the remainder of the Holocene *N. dutertrei* $\delta^{13}C$ varies between ~1.25 and 1.45‰ and the $\delta^{13}C$ of *Uvigerina* varies between 0 and 0.2‰.

3.6 Discussion

3.6.1 Origin and Transport of the Temperature signal

The warmth and subsequent cooling in the early Holocene in both the *Uvigerina* and *N. dutertrei* records is similar in timing to temperature records from the southern high latitudes (Figure 3-6). This suggests that the early Holocene warming in the EEP subsurface originated from the Southern Hemisphere. To determine if SAMW is the main conduit of this temperature signal, it has to be established that the signal was not caused by changes in regional winds or transported via the subtropics.

If the temperature signal were communicated to the subsurface through changes in regional winds, there would likely be a surface signal through changes in the Intertropical Convergence Zone (ITCZ) location or SST. The along shore winds in the region are stronger when the ITCZ is farther north which increases upwelling and cools SST [*Fiedler*, 1994; *Mitchell and Wallace*, 1992]. Modeling studies have shown that interhemispheric temperature differences affect the location of the ITCZ and the ITCZ migrates towards the hemisphere with more heating [*Broccoli et al.*, 2006; *Chiang and Friedman*, 2012; *Gibbons et al.*, 2014; *Yoshimori and Broccoli*, 2009]. The cooling in the southern hemisphere should shift the ITCZ northward between 9 and 8 kyr and proxy records should record this shift, however, there is no uniform signal to suggest that ITCZ shifted northward during this cooling [*Benway et al.*, 2006; *Haug et al.*, 2001; *Pahnke et al.*, 2007]. Additionally, a northward shift in the ITCZ should cool SST due to stronger winds enhancing upwelling. Both the alkenone record from the core site (Herbert et al. in prep), and other lower resolution records [*Koutavas and Sachs*, 2008; *Lea et al.*, 2000;

Pena et al., 2008] from around the region do not show a cooling between 9 and 8 kyr. Thus we conclude that the Holocene subsurface temperature signal was not a result of changes in regional winds.

Modeled tracer experiments and recent changes in the equatorial Pacific heat content indicate the subtropics may affect the temperatures of subthermocline water in the EEP and thus may be the origin of the early Holocene warmth [*England et al.*, 2014; *Meehl et al.*, 2013; *Qu et al.*, 2009]. If Subtropical surface waters are the origin of the warmth in the early Holocene they should be warmer during this period, but this is not reproduced in the proxy records. Records from 33-36˚S off Chile do not indicate a coherent pattern of SST change between 10 and 8 kyr [*Mohtadi et al.*, 2008], and one record even shows cooling during this period [*Kim et al.*, 2002]. A SST reconstruction from the subtropical north Pacific (25˚N) shows warmer SST from ~12-11 kyr, but it cools by 10 kyr [*Marchitto et al.*, 2010]. Neither subtropical nor EEP SST reconstructions indicate that either region is the origin of the early Holocene warmth.

The passive tracers, $\delta^{13}C$ and εNd provide additional support that the Southern Ocean is the origin of the early Holocene warmth. The increasing $\delta^{13}C$ values until 6 kyr in both the *N. dutertrei* and *Uvigerina* $\delta^{13}C$ are reproduced throughout the subtropical and equatorial oceans suggesting these trend likely have a common origin rather than reflecting local change in productivity (Figure 3-7). Spero and Lea [2002] hypothesized that changes in Southern Ocean $\delta^{13}C$ is transported to intermediate and thermocline waters via SAMW and AAIW. The $\delta^{13}C$ increase from the early Holocene to about 6 kyr is a rather robust feature and seen in several $\delta^{13}C$ reconstructions. The gradual increase in $\delta^{13}C$ is attributed to reinvigorated North Atlantic Deep Water contributing lower nutrient

and higher $\delta^{13}C$ water, reduced fractionation during the air-sea exchange due to warmer climates and an increase in the $^{12}CO_2$ being taken up by the terrestrial biosphere [*Spero and Lea*, 2002]. The *N. dutertrei* $\delta^{13}C$ record from ODP 1240 indicates the feature is common to the equatorial Pacific thermocline and thermostad [*Pena et al.*, 2008]. A similar signal is documented in the $\delta^{13}C$ of *G. ruber* in the Arabian Sea [*Sirocko et al.*, 1993] and in both *G. ruber* and *G. inflata* in the southwest Pacific [*Carter et al.*, 2008]. In addition to the $\delta^{13}C$ records, *N. dutertrei* εNd data from ODP 1240 indicate increased influence of the Southern Ocean between 11 and 8 kyr supporting the connection between the EEP thermostad and the Southern Ocean. In the EEP AAIW is deeper (~600 m) [*Fiedler and Talley*, 2006] than the calcification depth of *N. dutertrei* and the shelf/slope suggesting that SAMW is a more likely candidate for the transport of the $\delta^{13}C$ signal and εNd rather than AAIW.

Although εNd and $\delta^{13}C$ *N. dutertrei* records from ODP 1240 support the influence of the Southern Ocean on the EEP thermostad, the *N. dutertrei* temperature reconstruction from ODP 1240 shows decreased temperatures during the early Holocene [*Pena et al.*, 2008]. Both the Peru Margin and ODP 1240 temperature records are from the EEP thermostad and should be affected by similar dynamics making the difference difficult to reconcile. Possible explanations for the difference in the records include: the the *N. dutertrei* and *Uvigerina* data from the Peru Margin reflect a change in the coastal waters whereas the *N. dutertrei* record from ODP 1240 is more representative of the open ocean, the depth of the thermostad is different at the two locations or a change in depth habitat of *N. dutertrei*.

If the warmth in the early Holocene recorded in the Peru Margin temperature reconstructions is a coastal signal, it likely originated from off the coast of Southern Chile, near where AAIW is presently formed, and then transported along the narrow shelf along Chile and Peru. Records of SST from along the South American shelf do not show a similar warm early Holocene indicating the temperature signal would have been transported in the subsurface [*Chazen et al.* 2009, *Kim et al.* 2002]. The Chile-Peru Deep Coastal Current, is northward flowing, however the current is typically deeper than 300 m [*Chaigneau et al.* 2013]. If this current were the main conduit of the Southern Ocean temperature signal, I would expect a larger temperature change in the *Uvigerina* data compared to the *N. dutertrei* data. Further, the water mass tracer data, $\delta^{13}C$ and εNd at ODP 1240, indicate the influence of the Southern Ocean suggesting that the Southern Ocean does not only affect coastal waters in the EEP. The available evidence does not indicate that the early Holocene warmth recorded in the Peru Margin temperature records is a result of coastal hydrography.

Temperature and density transects along 86˚W indicate that the thermostad is deeper at the equator near ODP 1240 (Figure 3-8) than at 4˚S on the Peru Margin. This may explain the differences between the two records. If *N. dutertrei* is not living in the thermostad at ODP 1240 it may be recording the temperature of a different water mass explaining why the temperatures at the two sites differ. Additionally, the depth habitat of *N. dutertrei* may change. The *Uvigerina* record from the Peru Margin also records and early Holocene warm period suggesting a change in depth habitat is not the primary cause of the temperature signal from the Peru Margin. In contrast, the *N. dutertrei* record from ODP 1240 is not constrained by a benthic record and such a change in depth habitat of N.

dutertrei at ODP 1240 remains as a possible explanation for the difference between the two temperature records.

3.6.2 Mechanism to explain warm early Holocene SAMW

We next consider what caused SAMW to be warmer in the early Holocene, but to do so, we need to consider the deglacial history of the Southern Ocean. A current hypothesis for the rise in deglacial CO_2 is a poleward SWW shift which caused Antarctica to warm and increased upwelling in the Southern Ocean [*Anderson et al.*, 2009; *Denton et al.*, 2010; *Toggweiler et al.*, 2006]. The rise of CO_2 is thought to occur in two steps, the first during Heinrich stadial 1 (18-14.7 kyr) and the second between 13 and 9 kyr [*Anderson et al.*, 2009; *Pedro et al.*, 2010]. This would suggest that the warmth in the early Holocene was related to a southward position of the SWW and that the cooling was caused by a northward shift of the SWW. Precipitation records and Southern Ocean temperature records have also been used to argue for a more poleward position of the SWW in the early Holocene and an equatorward shift between 9-8 kyr [*Lamy et al.*, 2010; *Shevenell et al.*, 2011].

Using this evidence as a basis, the question remains: how did a southward position of the SWW cause warmer SAMW? As mentioned previously, proxy data suggest the southward migration of the SWW caused a more southerly position of the Subtropical Front [*Kaiser et al.*, 2005; *Moros et al.*, 2009; *Pahnke and Sachs*, 2006; *Sikes et al.*, 2002]. With the Subtropical Front farther south, it is possible that more warm subtropical water reached the SAMW formation region, thus warming SAMW. Observational studies have shown that eddies are important in transporting warm, subtropical waters into SAMW formation regions [*Hartin et al.*, 2011; *Herraiz-Borreguero and Rintoul*, 2010]. Thus if the Subtropical Front was shifted poleward, this

would allow for a greater transport of warm subtropical water via eddies to enter the SAMW formation region increasing in the temperature of the subducted SAMW, which eventually reached the thermostad in the equatorial Pacific.

The influence of SAMW on the thermostad may be unique to the early Holocene. Although the $\delta^{13}C$ records suggest Southern Ocean influence throughout the Holocene, the εNd from ODP1240 indicates a greater influence of Southern Ocean in the EEP only between 10 and 8 kyr [*Pena et al.*, 2013]. These proxy data agrees with models which predict that stronger and more poleward SWW increase the winter mixed layer causing enhanced subduction of SAMW, particularly in the Pacific basin [*Downes et al.*, 2011]. The difference between the *N. dutertrei* $\delta^{18}O_C$ and Mg/Ca estimates of the temperature change in the early Holocene implies that the thermostad water was fresher as well as warmer. This is also coherent with a greater influence of Southern Ocean sourced water as it is fresher than waters sourced from the subtropics [*Fiedler and Talley*, 2006]. The early Holocene change in the southern high latitudes was robust and a rather large transition in the climate system that had influence as far north as the equatorial Pacific, likely as a result of changes in ocean-atmosphere dynamics, not necessarily orbital forcing as has been proposed previously [*Rosenthal et al.*, 2013; *Shevenell et al.*, 2011].

3.6.3 Implications for Ocean Heat Content and Future Anthropogenic Change

The data presented here partially support the recent paper by Rosenthal et al. [2013], which argues that high latitudes are important in affecting OHC. The intermediate water (600-900 m) temperatures from the Indonesia Through Flow (ITF) are also warmer between 10 and 8 kyr but by only ~1˚C rather than by ~2˚C (Figure 3-9). This implies that southern high latitude climate signals affected AAIW as well as SAMW. After 8 kyr,

the two records diverge with the ITF temperature record showing stronger cooling of about ~1.5˚C, while the EEP temperature records do not show a long term trend (Figure 3-9). The difference after 8 kyr may result from a weaker influence of the Southern Ocean in the equatorial region [*Pena et al.*, 2013] and several other possible processes, including greater subtropical influence in the EEP and/or Northern Hemisphere influence in the ITF, affecting the temperature records.

The temperature anomalies in the subsurface of the EEP are not affecting the surface with the same magnitude. The thermostad water is thought to join the Peru-Chile Undercurrent [*Chaigneau et al.*, 2013] and eventually to upwell in the cold tongue [*Qu et al.*, 2010]. A high resolution SST reconstruction from the cold tongue at 11˚S does show temperatures that are ~0.5˚C higher in between 9.5 and 8.9 kyr (Figure 3-9) [*Chazen et al.*, 2009]. This may be a result of the surfacing of the temperature signal from the thermostad, however, it is not as strong as a signal as is seen in the subsurface. Part of the thermostad temperature signal may be dissipated via subsurface eddies farther south in the Peru Chile Undercurrent, which have been documented by Argo floats [*Johnson and McTaggart*, 2010]. The weak surface expression implies that the temperature signal from the southern high latitudes largely remains sequestered from the surface once it is subducted, supporting that changes in the interior ocean heat content may help distribute heat associated with climate change [*Levitus et al.*, 2012; *Rosenthal et al.*, 2013].

The SWW have become stronger and shifted poleward in response to a positive Southern Annular Mode over the past 50 years [*Thompson and Solomon*, 2002; *Thompson et al.*, 2011]. Can the early Holocene with more poleward SWW be used as an analogue to future climate change? Similar to the early Holocene, chlorofluorocarbon

measurements imply increased transport of SAMW for the last two decades [*Waugh et al.*, 2013]. However, unlike the early Holocene, SAMW is becoming cooler and fresher [*Boning et al.*, 2008]. Cooling of SAMW is likely related to air-sea fluxes, whereas warming is related to frontal shifts [*Meijers et al.*, 2011]. This implies the changes in SAMW during the last 50 years have been dominated by air-sea fluxes and the early Holocene might have been influenced by shifting fronts. The difference may be due to time scales since the recent trend in the SWW has only occurred for ~50 years and the early Holocene wind shift was sustained for millennia. Since the recent SWW shift likely will not continue past 2045 due to the recovery of stratospheric ozone [*Barnes et al.*, 2014], the Holocene events documented here may not be an appropriate analogue for future change. Nonetheless, the temperature records from the EEP do imply the importance of dynamics in contributing to EEP OHC on centennial and millennial time scales, however, the efficiency of this mode depends on the background climate state of the Southern Ocean.

3.7 References

Anderson, R. F., et al. (2009), Wind-Driven Upwelling in the Southern Ocean and the Deglacial Rise in Atmospheric CO2, *Science*, *323*(5920), 1443-1448.

Andreasen, D. H., et al. (2006), Fidelity of radially viewed ICP-OES and magnetic-sector ICP-MS measurement of Mg/Ca and Sr/Ca ratios in marine biogenic carbonates: Are they trustworthy together?, *Geochemistry Geophysics Geosystems*, *7*.

Balmaseda, M. A., et al. (2013), Distinctive climate signals in reanalysis of global ocean heat content, *Geophysical Research Letters*, *40*(9), 1754-1759.

Banks, H. T., and N. L. Bindoff (2003), Comparison of Observed Temperature and Salinity Changes in the Indo-Pacific with Results from the Coupled Climate Model HadCM3: Processes and Mechanisms*, *Journal of Climate*, *16*(1), 156-166.

Bard, E., et al. (1996), Pleistocene sea levels and tectonic uplift based on dating of corals from Sumba Island, Indonesia, *Geophysical Research Letters*, *23*(12), 1473-1476.

Bard, E., et al. (2010), Deglacial Meltwater Pulse 1B and Younger Dryas Sea Levels Revisited with Boreholes at Tahiti, *Science*, *327*(5970), 1235-1237.

Barnes, E. A., et al. (2014), Delayed Southern Hemisphere Climate Change Induced by Stratospheric Ozone Recovery, as Projected by the CMIP5 Models, *Journal of Climate*, *27*(2), 852-867.

Benway, H. M., et al. (2006), Eastern Pacific Warm Pool paleosalinity and climate variability: 0-30 kyr, *Paleoceanography*, *21*(3).

Bianchi, C., and R. Gersonde (2004), Climate evolution at the last deglaciation: the role of the Southern Ocean, *Earth and Planetary Science Letters*, *228*, 407-424.

Boning, C. W., et al. (2008), The response of the Antarctic Circumpolar Current to recent climate change, *Nature Geoscience*, *1*(12), 864-869.

Bostock, H. C., et al. (2013), A review of the Australian-New Zealand sector of the Southern Ocean over the last 30 ka (Aus-INTIMATE project), *Quaternary Science Reviews*, *74*(0), 35-57.

Broccoli, A. J., et al. (2006), Response of the ITCZ to Northern Hemisphere cooling, *Geophysical Research Letters*, *33*(1).

Bryan, S. P., and T. M. Marchitto (2008), Mg/Ca-temperature proxy in benthic foraminifera: New calibrations from the Florida Straits and a hypothesis regarding Mg/Li, *Paleoceanography*, *23*(2), PA2220.

Cai, W. J., et al. (2010), Simulations of Processes Associated with the Fast Warming Rate of the Southern Midlatitude Ocean, *Journal of Climate*, *23*(1), 197-206.

Carter, L., et al. (2008), Southwest Pacific modulation of abrupt climate change during the Antarctic Cold Reversal-Younger Dryas, *Palaeogeography, Palaeoclimatology, Palaeoecology*, *260*, 284-298.

Chaigneau, A., et al. (2013), Near-coastal circulation in the Northern Humboldt Current System from shipboard ADCP data, *Journal of Geophysical Research: Oceans*, *118*(10), 5251-5266.

Chazen, C. R., et al. (2009), Abrupt mid-Holocene onset of centennial-scale climate variability on the Peru-Chile Margin, *Geophysical Research Letters*, *36*.

Chiang, J. C. H., and A. R. Friedman (2012), Extratropical Cooling, Interhemispheric Thermal Gradients, and Tropical Climate Change, *Annual Review of Earth and Planetary Sciences, Vol 40*, *40*, 383-412.

Denton, G. H., et al. (2010), The Last Glacial Termination, *Science*, *328*(5986), 1652-1656.

Dong, S., et al. (2008), Southern Ocean mixed-layer depth from Argo float profiles, *Journal of Geophysical Research: Oceans (1978-2012)*, *113*(C6).

Downes, S. M., et al. (2011), Impacts of wind stress on the Antarctic Circumpolar Current fronts and associated subduction, *Geophysical Research Letters*, *38*(11), L11605.

Elderfield, H., et al. (2006), Calibrations for benthic foraminiferal Mg/Ca paleothermometry and the carbonate ion hypothesis, *Earth and Planetary Science Letters*, *250*(3-4), 633-649.

England, M. H., et al. (2014), Recent intensification of wind-driven circulation in the Pacific and the ongoing warming hiatus, *Nature Clim. Change*, *4*(3), 222-227.

Fairbanks, R. G., and R. K. Matthews (1978), The Marine Oxygen Isotope Record in Pleistocene Coral, Barbados, West Indies, *Quaternary Research*, *10*, 181-196.

Fairbanks, R. G. (1990), The Age and Origin of the "Younger Dryas Climate Event" in Greenland Ice Cores, *Paleoceanography*, *5*(6), 937-948.

Fairbanks, R. G., et al. (2005), Radiocarbon calibration curve spanning 0 to 50,000 years BP based on paired 230Th/234U/238U and 14C dates on pristine corals, *Quaternary Science Reviews*, *24*(16-17), 1781-1796.

Fiedler, P. C. (1994), Seasonal and interannual variability of coastal zone color scanner phytoplankton pigments and winds in the eastern tropical Pacific, *J. Geophys. Res.*, *99*(C9), 18371-18384.

Fiedler, P. C., and L. D. Talley (2006), Hydrography of the eastern tropical Pacific: A review, *Progress in Oceanography*, *69*(2-4), 143-180.

Gibbons, F. T., et al. (2014), Deglacial delta O-18 and hydrologic variability in the tropical Pacific and Indian Oceans, *Earth and Planetary Science Letters*, *387*, 240-251.

Gregory, J. M. (2000), Vertical heat transports in the ocean and their effect an time-dependent climate change, *Climate Dynamics*, *16*(7), 501-515.
Hanawa, K., and L. D. Talley (2001), Mode waters, *International Geophysics Series*, *77*, 373-386.
Hartin, C. A., et al. (2011), Formation rates of Subantarctic mode water and Antarctic intermediate water within the South Pacific, *Deep Sea Research Part I: Oceanographic Research Papers*, *58*(5), 524-534.
Haug, G. H., et al. (2001), Southward Migration of the Intertropical Convergence Zone Through the Holocene, *Science*, *293*(5533), 1304-1308.
Herraiz-Borreguero, L., and S. R. Rintoul (2010), Subantarctic Mode Water variability influenced by mesoscale eddies south of Tasmania, *Journal of Geophysical Research: Oceans*, *115*(C4), C04004.
Herraiz-Borreguero, L., and S. R. Rintoul (2011), Subantarctic mode water: distribution and circulation, *Ocean Dynamics*, *61*(1), 103-126.
IUPAC (1994), Commission on Atomic Weights and Isotopic Abundances, *Pure and Applied Chemistry*, *66*, 2423-2444.
Johnson, G. C., and K. E. McTaggart (2010), Equatorial Pacific 13 degrees C Water Eddies in the Eastern Subtropical South Pacific Ocean, *Journal of Physical Oceanography*, *40*(1), 226-236.
Jones, D. C., et al. (2011), The transient response of the Southern Ocean pycnocline to changing atmospheric winds, *Geophysical Research Letters*, *38*.
Kaiser, J., et al. (2005), A 70-kyr sea surface temperature record off southern Chile (Ocean Drilling Program Site 1233), *Paleoceanography*, *20*(4).
Kim, J. H., et al. (2002), Last deglacial sea-surface temperature evolution in the Southeast Pacific compared to climate changes on the South American continent, *Quaternary Science Reviews*, *21*(18-19), 2085-2097.
Kosaka, Y., and S. P. Xie (2013), Recent global-warming hiatus tied to equatorial Pacific surface cooling, *Nature*, *501*(7467), 403-+.
Koutavas, A., and J. P. Sachs (2008), Northern timing of deglaciation in the eastern equatorial Pacific from alkenone paleothermometry, *Paleoceanography*, *23*(4), PA4205.
Lamy, F., et al. (2010), Holocene changes in the position and intensity of the southern westerly wind belt, *Nature Geoscience*, *3*(10), 695-699.
Lea, D. W., et al. (2000), Climate Impact of Late Quaternary Equatorial Pacific Sea Surface Temperature Variations, *Science*, *289*(5485), 1719-1724.
LeGrande, A. N., and G. A. Schmidt (2006), Global gridded data set of the oxygen isotopic composition in seawater, *Geophysical Research Letters*, *33*(12), L12604.
Levitus, S., et al. (2012), World ocean heat content and thermosteric sea level change (0–2000 m), 1955–2010, *Geophysical Research Letters*, *39*(10), L10603.
Lighty, R. G., et al. (1982), Acropora Palmata Reef Framework: A Reliable Indicator of Sea Level in the Western Atlantic for the Past 10,000 Years, *Coral Reefs*, *1*, 125-130.
Locarnini, R. A., A. V. Mishonov, J. I. Antonov, T. P. Boyer, H. E. Garcia, O. K. Baranova, M. M. Zweng, and D. R. Johnson (2009), Temperature, edited by N. A. N. 68, U.S. Government Printing Office, Washington D.C.
Luer, V., et al. (2009), Radiolarian-based sea surface temperatures and paleoceanographic changes during the Late Pleistocene‚ÄìHolocene in the subantarctic southwest Pacific, *Marine Micropaleontology*, *70*(3‚Äì4), 151-165.
Lukas, R. (1986), The termination of the Equatorial Undercurrent in the eastern Pacific, *Progress In Oceanography*, *16*(2), 63-90.
Marchitto, T. M., et al. (2010), Dynamical Response of the Tropical Pacific Ocean to Solar Forcing During the Early Holocene, *Science*, *330*(6009), 1378-1381.

Marr, J. P., et al. (2013), Southwest Pacific Ocean response to a warming world: Using Mg/Ca, Zn/Ca, and Mn/Ca in foraminifera to track surface ocean water masses during the last deglaciation, *Paleoceanography*, *28*(2), 347-362.

Masson-Delmotte, V., et al. (2011), A comparison of the present and last interglacial periods in six Antarctic ice cores, *Climate of the Past*, *7*(2), 397-423.

McCorkle, D. C., et al. (1997), Vertical distributions and stable isotopic compositions of live (stained) benthic foraminifera from the North Carolina and California continental margins, *Deep Sea Research Part I: Oceanographic Research Papers*, *44*(9), 983-1024.

Meehl, G. A., et al. (2013), Externally Forced and Internally Generated Decadal Climate Variability Associated with the Interdecadal Pacific Oscillation, *Journal of Climate*, *26*(18), 7298-7310.

Meijers, A. J. S., et al. (2011), Frontal movements and property fluxes: Contributions to heat and freshwater trends in the Southern Ocean, *Journal of Geophysical Research-Oceans*, *116*.

Mitchell, T. P., and J. M. Wallace (1992), The Annual Cycle in Equatorial Convection and Sea Surface Temperature, *Journal of Climate*, *5*(10), 1140-1156.

Mohtadi, M., et al. (2008), Deglacial pattern of circulation and marine productivity in the upwelling region off central-south Chile, *Earth and Planetary Science Letters*, *272*(1-2), 221-230.

Moros, M., et al. (2009), Holocene climate variability in the Southern Ocean recorded in a deep-sea sediment core off South Australia, *Quaternary Science Reviews*, *28*(19,Äì20), 1932-1940.

Mulvaney, R., et al. (2012), Recent Antarctic Peninsula warming relative to Holocene climate and ice-shelf history, *Nature*, *489*(7414), 141-U204.

Pahnke, K., and J. P. Sachs (2006), Sea surface temperatures of southern midlatitudes 0–160 kyr B.P, *Paleoceanography*, *21*(2), PA2003.

Pahnke, K., et al. (2007), Eastern tropical Pacific hydrologic changes during the past 27,000 years from D/H ratios in alkenones, *Paleoceanography*, *22*(4).

Pedro, J. B., et al. (2010), The last deglaciation: timing the bipolar seesaw, *Clim. Past Discuss.*, *7*(1), 397-430.

Peltier, W. R., and R. G. Fairbanks (2006), Global glacial ice volume and Last Glacial Maximum duration from an extended Barbados sea level record, *Quaternary Science Reviews*, *25*(23-24), 3322-3337.

Pena, L. D., et al. (2008), El Nino-Southern Oscillation-like variability during glacial terminations and interlatitudinal teleconnections, *Paleoceanography*, *23*(3), PA3101.

Pena, L. D., et al. (2013), Rapid changes in meridional advection of Southern Ocean intermediate waters to the tropical Pacific during the last 30 kyr, *Earth and Planetary Science Letters*, *368*(0), 20-32.

Qu, T., et al. (2010), The Obduction of Equatorial 13˚C Water in the Pacific Identified by a Simulated Passive Tracer, *Journal of Physical Oceanography*, *40*(10), 2282-2297.

Qu, T. D., et al. (2009), Origin and Pathway of Equatorial 13 degrees C Water in the Pacific Identified by a Simulated Passive Tracer and Its Adjoint, *Journal of Physical Oceanography*, *39*(8), 1836-1853.

Rincon-Martinez, D., et al. (2011), Tracking the equatorial front in the eastern equatorial Pacific Ocean by the isotopic and faunal composition of planktonic foraminifera, *Marine Micropaleontology*, *79*, 24-40.

Rosenthal, Y., et al. (1997), Temperature control on the incorporation of magnesium, strontium, fluorine, and cadmium into benthic foraminiferal shells from Little Bahama Bank: Prospects for thermocline paleoceanography, *Geochimica Et Cosmochimica Acta*, *61*(17), 3633-3643.

Rosenthal, Y., et al. (1999), Precise determination of element/calcium ratios in calcareous samples using sector field inductively coupled plasma mass spectrometry, *Analytical Chemistry*, *71*(15), 3248-3253.
Rosenthal, Y., et al. (2013), Pacific Ocean Heat Content During the Past 10,000 Years, *Science*, *342*(6158), 617-621.
Rowe, G. D., et al. (2000), Pacific equatorial subsurface countercurrent velocity, transport, and potential vorticity, *Journal of Physical Oceanography*, *30*(6), 1172-1187.
Ryan, W. B. F., et al. (2009), Global Multi-Resolution Topography synthesis, *Geochemistry Geophysics Geosystems*, *10*.
Sabine, C. L., et al. (2004), The oceanic sink for anthropogenic CO2, *Science*, *305*(5682), 367-371.
Sarmiento, J. L., et al. (2004), High-latitude controls of thermocline nutrients and low latitude biological productivity, *Nature*, *427*(6969), 56-60.
Schlitzer, R. (2011), Ocean Data View, edited.
Shackleton, N. J., and E. Vincent (1978), Oxygen and carbon isotope studies in recent foraminifera from the southwest Indian ocean, *Marine Micropaleontology*, *3*(1), 1-13.
Shevenell, A. E., et al. (2011), Holocene Southern Ocean surface temperature variability west of the Antarctic Peninsula (vol 470, pg 250, 2011), *Nature*, *472*(7342).
Sikes, E. L., et al. (2002), Glacial-interglacial sea surface temperature changes across the subtropical front east of New Zealand based on alkenone unsaturation ratios and foraminiferal assemblages, *Paleoceanography*, *17*(2), 2-1-2-13.
Sikes, E. L., et al. (2009), Southern Ocean seasonal temperature and Subtropical Front movement on the South Tasman Rise in the late Quaternary, *Paleoceanography*, *24*(2), PA2201.
Sirocko, F., et al. (1993), Century-scale events in monsoonal climate over the past 24,000 years, *Nature*, *364*, 322-324.
Spero, H. J., and D. W. Lea (2002), The Cause of Carbon Isotope Minimum Events on Glacial Terminations, *Science*, *296*(5567), 522-525.
Stenni, B., et al. (2011), Expression of the bipolar see-saw in Antarctic climate records during the last deglaciation, *Nature Geosci*, *4*(1), 46-49.
Thompson, D. W. J., and S. Solomon (2002), Interpretation of Recent Southern Hemisphere Climate Change, *Science*, *296*(5569), 895-899.
Thompson, D. W. J., et al. (2011), Signatures of the Antarctic ozone hole in Southern Hemisphere surface climate change, *Nature Geoscience*, *4*(11), 741-749.
Toggweiler, J. R., et al. (1991), The Peru Upwelling and the Ventilation of the South Pacific Thermocline, *J. Geophys. Res.*, *96*(C11), 20467-20497.
Toggweiler, J. R., et al. (2006), Midlatitude westerlies, atmospheric CO2, and climate change during the ice ages, *Paleoceanography*, *21*(2), PA2005.
Tsuchiya, M. (1981), The Origin of the Pacific Equatorial 13˚C Water, *Journal of Physical Oceanography*, *11*(6), 794-812.
Waugh, D. W., et al. (2013), Recent Changes in the Ventilation of the Southern Oceans, *Science*, *339*(6119), 568-570.
Yoshimori, M., and A. J. Broccoli (2009), On the link between Hadley circulation changes and radiative feedback processes, *Geophysical Research Letters*, *36*.

Table 3-1. The radiocarbon dates for CDH23. A reservoir age of 500 years has been subtracted from carbon-14 year values shown. The radiocarbon year was converted to calendar year using the Fairbanks et al. (2005) calibration.

Core	ID	Depth (cm)	Carbon-14 year ± 1 sigma	calendar year ± 1 sigma
CDH23	OS- 77623	30	1180±40	1091±56
CDH23	OS-101833	42	1610±20	1505±33
CDH23	OS-101834	118	2500±20	2611±76
CDH23	OS 77579	160	2920±35	3061±64
CDH23	OS-77576	260.5	3480±35	3745±58
CDH23	OS-77575	350.5	4040±40	4504±61
CDH23	OS-84123	400	4300±35	4853±20
CDH23	OS- 77546	460.5	4790±50	5540±62
CDH23	OS-84122	500	5220±30	5958±33
CDH23	OS-84108	550	5730±35	6510±49
CDH23	OS-84168	600	6010±45	6847±62
CDH23	OS-77574	660.5	6400±40	7326±49
CDH23	OS-84121	781	7450±40	8281±57
CDH23	OS-77580	850.25	8140±45	9062±56
CDH23	OS-84120	900	8100±45	9023±41
CDH23	OS-77547	1000.25	8720±60	9675±102
CDH23	OS-84115	1100	9420±40	10648±54

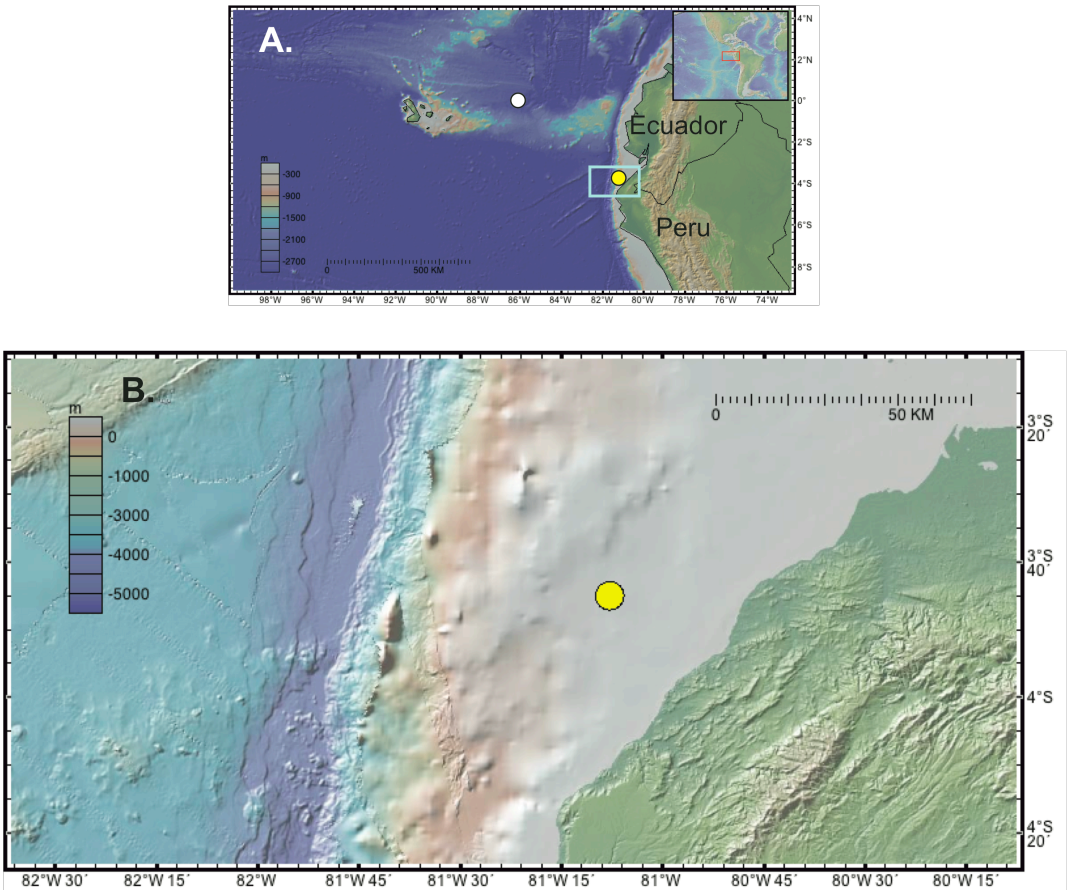

Figure 3-1. (A) Location of core discussed in this chapter (yellow circle) and location of core ODP 1240 (2941 m water depth). (B) Expanded view of light blue box in (A), showing detail of bathymetry in region of core location. Figures generated using geomapapp.org.

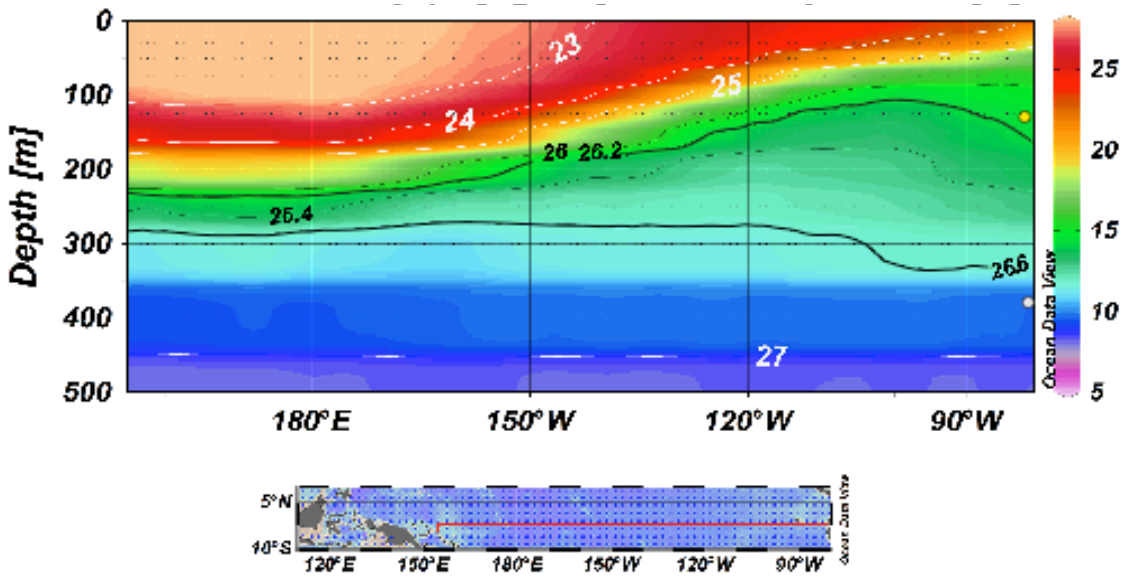

Figure 3-2. Neutral density isopycnals are contoured on top of temperatures (color bar) from across the Pacific centered at 3-5˚S. The thermostad ranges from 11-14˚C and 26.2-26.6 kg/m^3. The yellow circle at right indicates the approximate depth of calcification for *N. dutertrei* and the white circle below it indicates the depth of the core-top *Uvigerina* calcification. The image was made with ODV [*Schlitzer*, 2011] using the data from World Ocean Atlas 2009 [*Locarnini*, 2009].

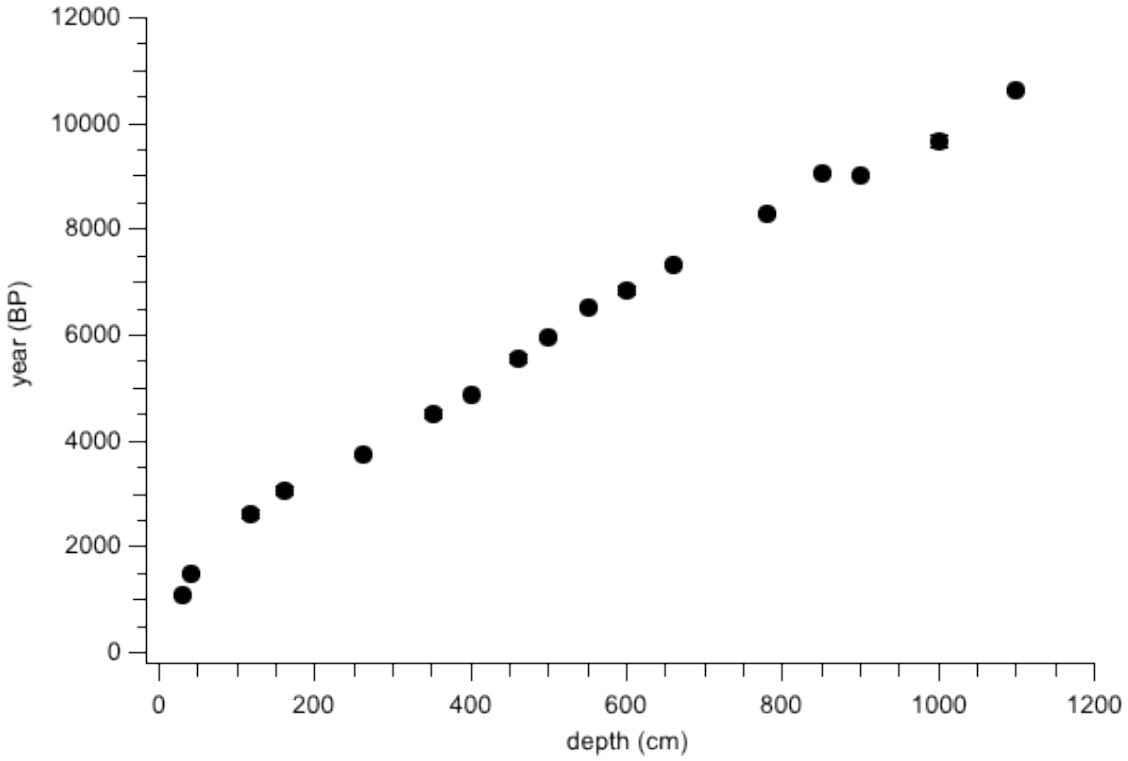

Figure 3-3. Calendar year estimated from *N. dutertrei* radiocarbon dates using a 500 year reservoir age and the Fairbanks et al. (2005) calibration. The error bars on the ages are indicated but are small than symbols in most cases. The sedimentation rate is relatively constant throughout the core.

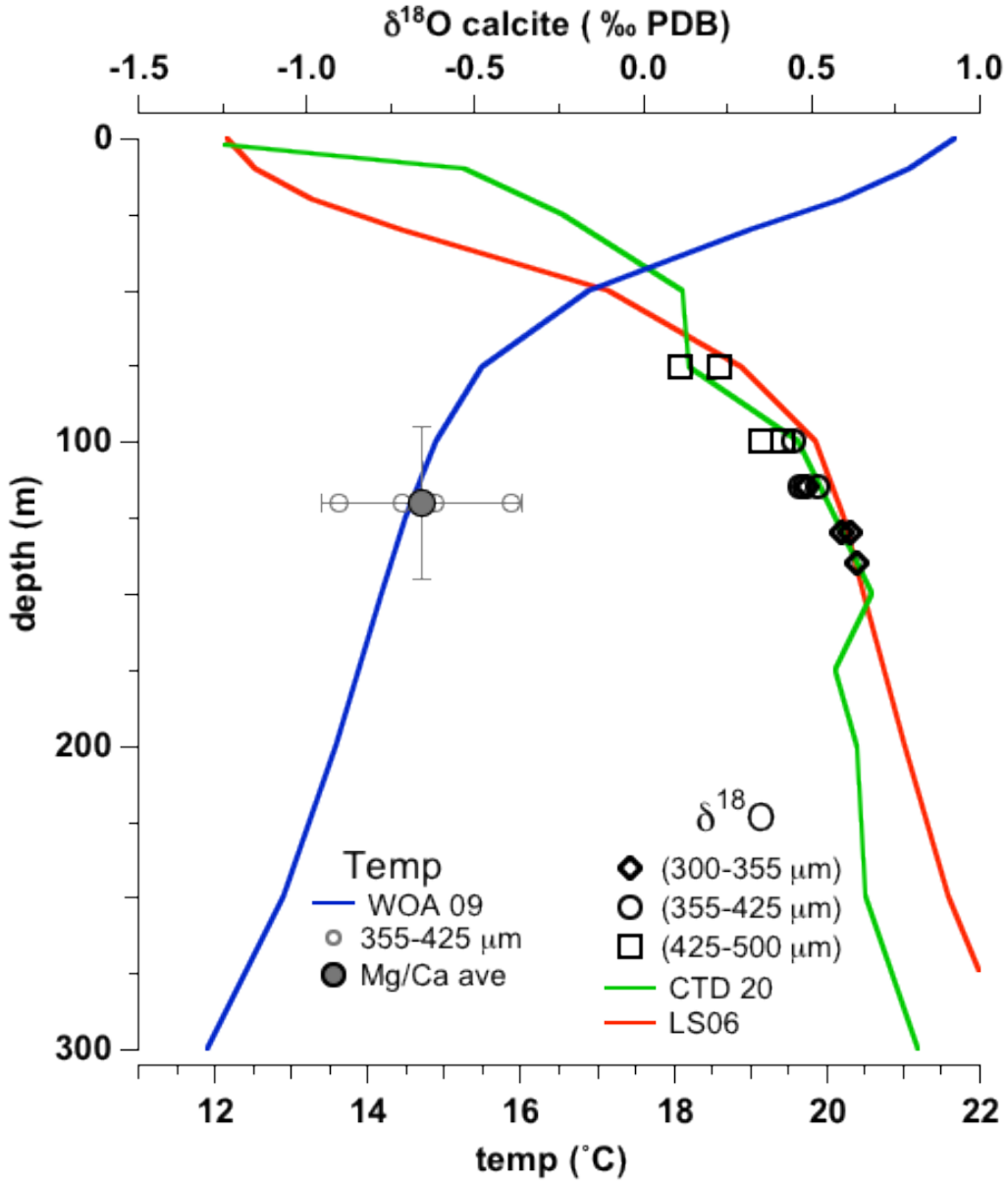

Figure 3-4. Core top *N. dutertrei* $\delta^{18}O_C$ (black markers) are plotted on water column profiles of $\delta^{18}O_{SW}$ (discrete $\delta^{18}O_{SW}$ samples taken during the cruise (green) and derived from the $\delta^{18}O$ model of LeGrand and Schmidt [2006] (red)). The $\delta^{18}O_{SW}$ values were converted to $\delta^{18}O_C$ using the Shackleton and Vincent (1978) equation. The open black symbols represent the $\delta^{18}O_C$ for the different size fractions of *N. dutertrei*. The calcification depth for the size the 355-425 µm *N. dutertrei* (open circle) was determined to be between 100-130 m. Core tope *N. dutertrei* Mg/Ca temperature estimates (grey open circles) and average are plotted on a temperature profile from World Ocean Atlas 2009 [*Locarnini*, 2009]

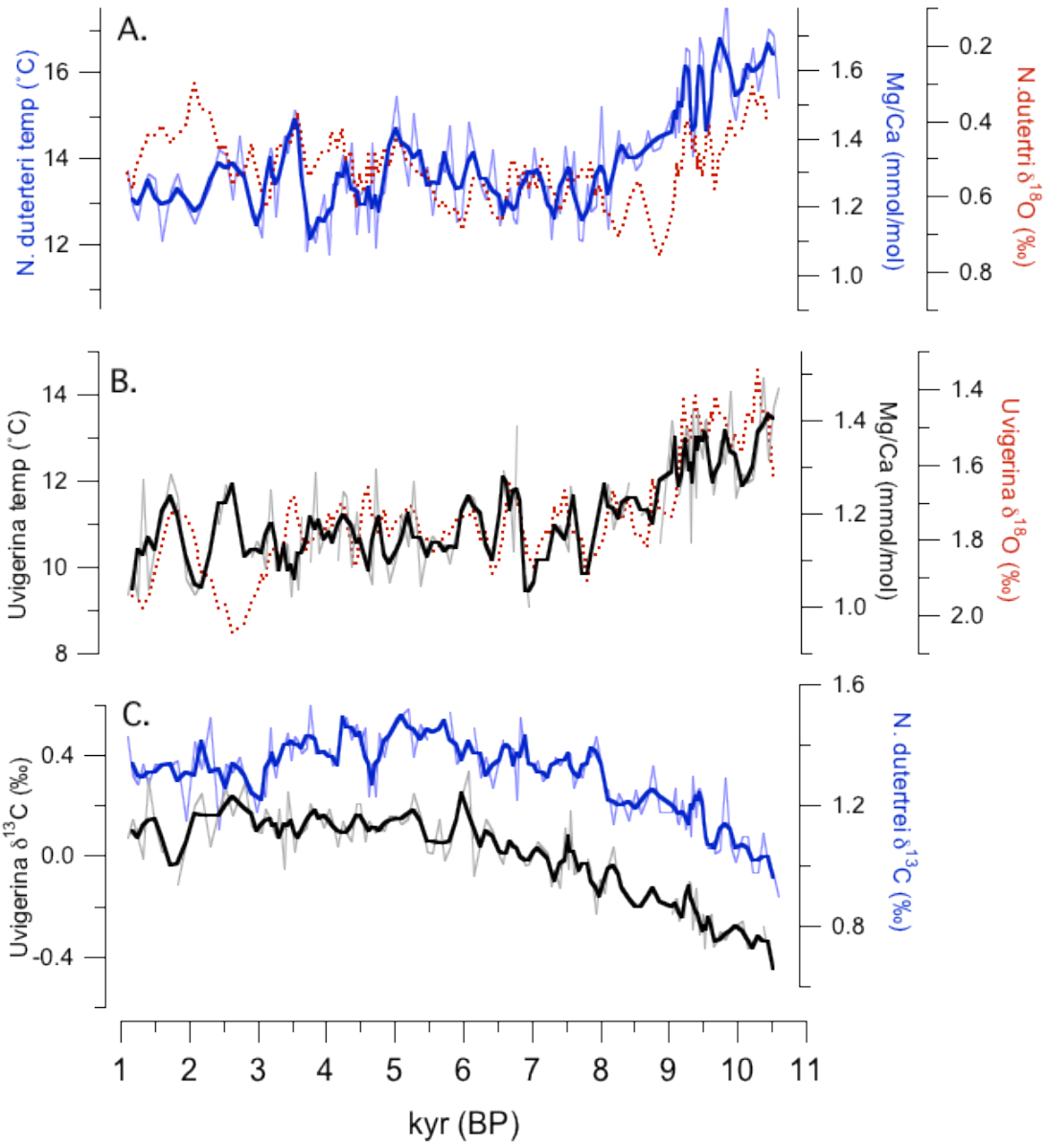

Figure 3-5. *N. dutertrei* (blue) and *Uvigerina* (black) individual data (thin line) and 3-point running average (thick line) from the Holocene. (A) Subthermocline temperature reconstructions are estimated from Mg/Ca of *N. dutertrei* using the Anand et al. 2003 multi species calibration. $\delta^{18}O_C$ (red dashed line) has been corrected for sea level (refer to text). (B) Same as A, but for *Uvigerina* and temperature are estimated using the Bryan et al. 2008 calibration and temperature is corrected for sea level. (C) *N. dutertrei* and *Uvigerina* $\delta^{13}C$ records

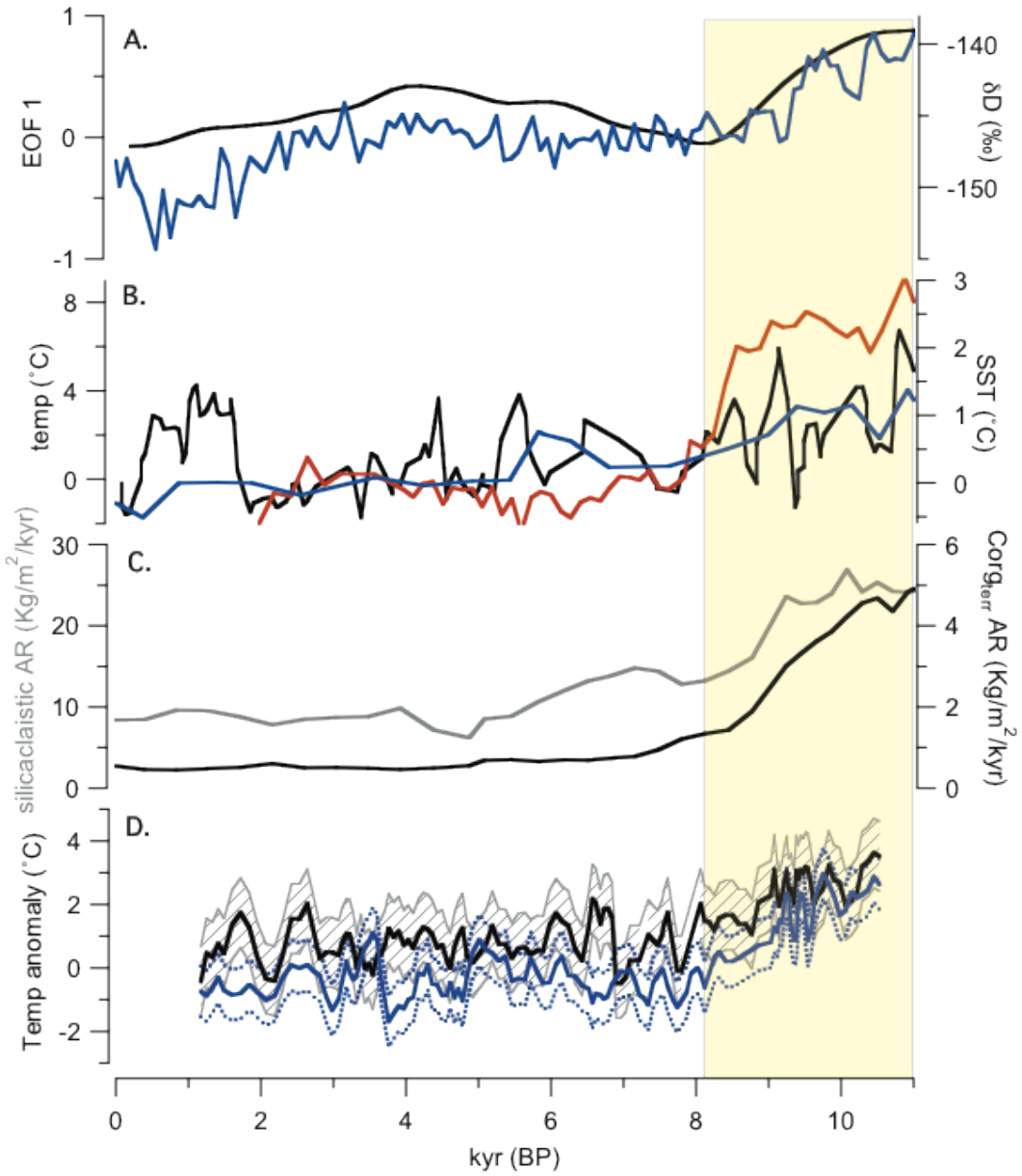

Figure 3-6. Southern Hemisphere high latitude temperature and precipitation records plotted along with *Uvigerina* and *N. dutertrei* temperature anomalies from the EEP. The yellow shaded area is the period of early Holocene warmth. (A) Antarctic temperature records from and EOF of 5 ice core $\delta^{18}O$ records (black line) [*Masson-Delmotte et al.*, 2011] and James Ross ice core δD (blue line) [*Mulvaney et al.*, 2012] (B) Ocean temperature records (0-150m) from the Pacific sector of the Southern Ocean (black line) [*Shevenell et al.*, 2011], SST from MD97 2021 (45˚S, 174˚E) (red line) [*Pahnke and Sachs*, 2006] and SST from ODP 1233 (41˚S, 74˚W) (blue line) [*Kaiser et al.*, 2005] (C) Accumulation rates as proxies for precipitation from the Chilean Fjords (53˚S) [*Lamy et al.*, 2010] (D) *N. dutertrei* (blue) and *Uvigerina* (black) temperature reconstructions from the EEP (this study). Note the different temperature scales on the axes

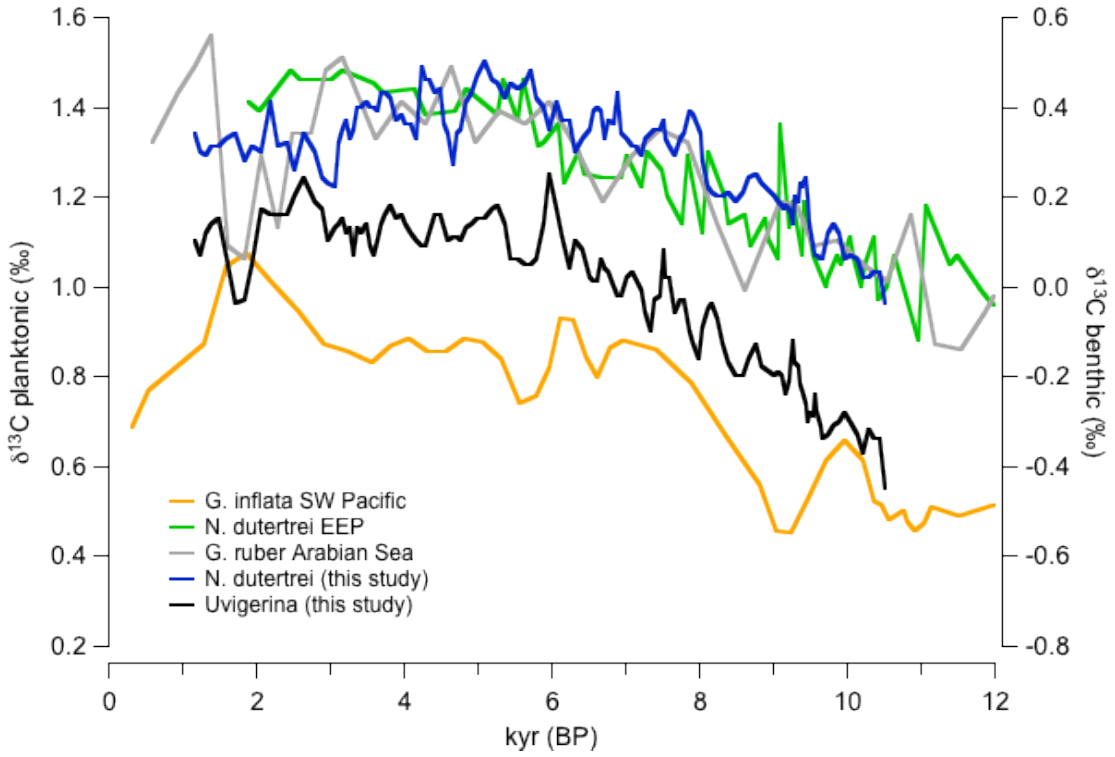

Figure 3-7. Planktonic $\delta^{13}C$ records from various locations around the globe show a similar increase in $\delta^{13}C$ values until around 6 kyr. Grey line [*Sirocko et al.,* 1993], orange line [*Carter et al.,* 2008], green line [*Pena et al*., 2013], *N. dutertrei* (this study) (blue line). *Uvigerina* (this study) (black line) is the only benthic specie.

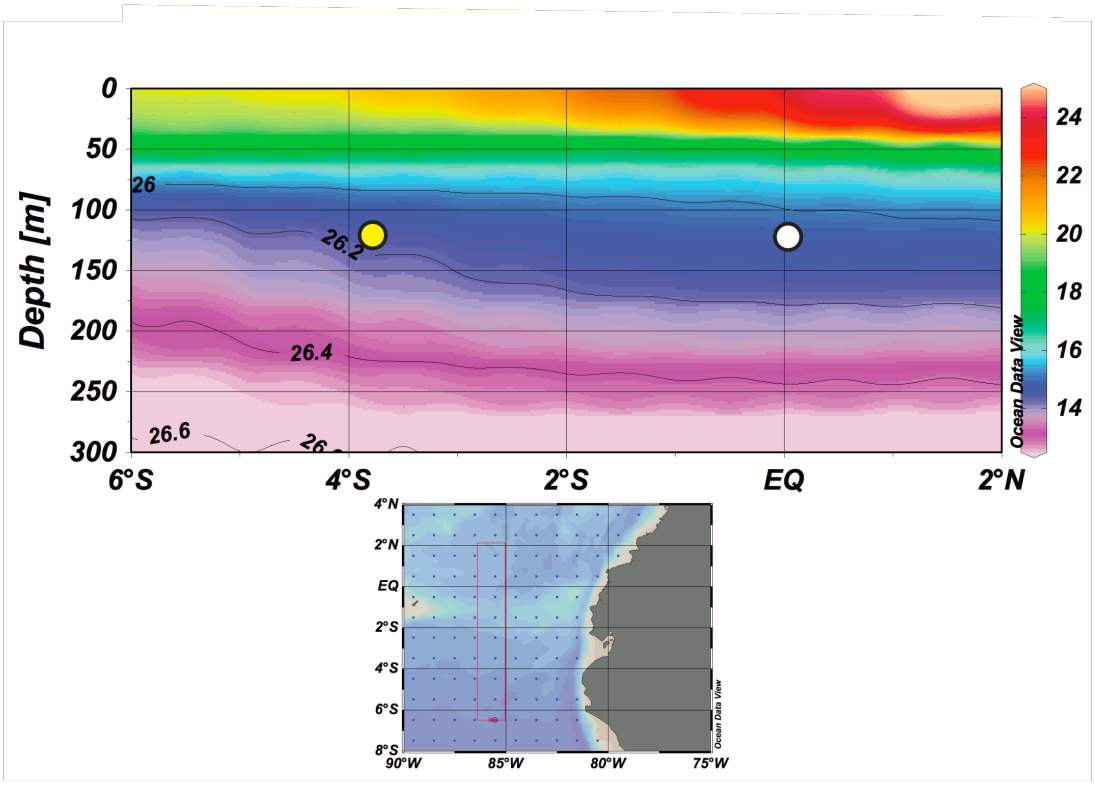

Figure 3-8. Temperature during austral summer (Jan, Feb, Mar) from the surface to 300 along the 86˚W parallel is plotted versus latitude. Contours are of neutral density (kg/m^3) and the yellow circle is approximate latitude of the Peru Margin core and the white circle is the latitude of ODP 1240. The bottom image is a map of the region and the red line is the transect plotted above. The image was made with ODV [*Schlitzer*, 2011] using the data from World Ocean Atlas 2009 [*Locarnini*, 2009].

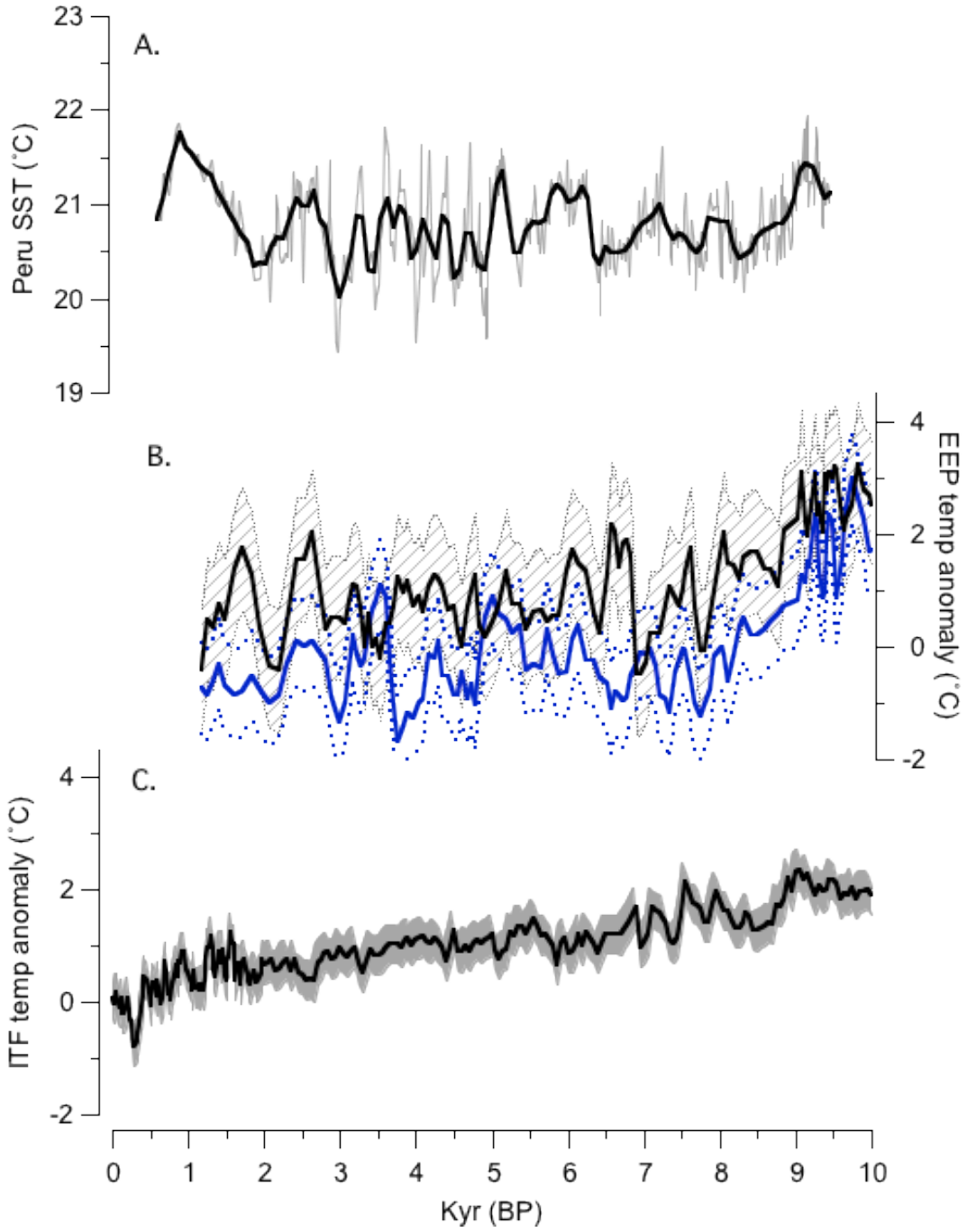

Figure 3-9. (A) SST temperature records from 11˚S [*Chazen et al.*, 2009] plotted along with (B) the EEP *N. dutrertrei* (blue) and *Uvigerina* (black) and (C) the ITF 600-900 m [*Rosenthal et al.*, 2013] temperature anomalies. The ITF and the EEP subsurface temperature records are warmer during the early Holocene, but the signal is not as pronounced in SST farther south

CHAPTER FOUR

EXTERNAL FORCING AND INTERNAL VARIABILITY INFLUENCE ON THE EASTERN EQUATORIAL PACIFIC TEMPERATURES DURING THE COMMON ERA

4.1 Abstract

Using a high resolution sediment core from off the coast of northern Peru in the eastern equatorial Pacific (EEP), we generate an alkenone sea surface temperature (SST) record and *Neogloboquadrina dutertrei* sub-thermocline temperature (STT) record for the last 2,500 years. By reconstructing both SSTs and STTs, we examine the EEP upper water column response to external forcing including solar variability, large volcanic eruptions and Northern Hemisphere temperatures. The SST record increases non-monotonically by 0.8˚C and does not parallel Northern Hemisphere temperatures or respond to solar variability or volcanic eruptions. In contrast, the STTs are ~0.3˚C colder during the Little Ice Age and prior to 1800 CE and low STTs correspond to periods of low radiative forcing indicating that STTs are affected by external forcings. Because SSTs and STTs are decoupled, the signals from external forcings are likely transported to the base of the thermocline via the subtropics rather than surface water directly above. After 1800 CE STTs increase, which is prior to Northern Hemisphere temperatures, but when several equatorial Pacific records also change, suggesting a rather large transition in the equatorial Pacific caused by variability intrinsic to the equatorial Pacific. The cool STTs during the Little Ice Age implies that on centennial time scales the subsurface is in equilibrium with the ocean-atmosphere system. However, the relationship between radiative forcing and multi-decadal STT variability suggests a dynamic response to radiative changes that persist in the subsurface for several decades.

4.2 Introduction

The tropical Pacific influences global precipitation patterns and ocean heat content on interannual and decadal time scales [*Alexander et al.*, 2002; *Deser et al.*, 2004; *England et al.*, 2014; *Kosaka and Xie*, 2013; *Roemmich and Gilson*, 2011]. Warming in the eastern equatorial Pacific (EEP), which occurs during El Niño events, weakens the Walker circulation causing droughts in southeast Asia and flooding along the coast of North and Central America [*Dai and Wigley*, 2000]. Multidecadal variability in EEP temperatures is associated with the Pacific Decadal Oscillation (PDO), which affects fisheries, north Pacific storm tracks, precipitation patterns in southwestern North America [*Mantua and Hare*, 2002] and may be linked to the recent hiatus in global surface temperatures [*England et al.*, 2014; *Kosaka and Xie*, 2013]. The importance of EEP interannual and decadal variability in the global climate system has been well documented over the years [*Barlow et al.*, 2001; *Hoerling et al.*, 2010; *McPhaden and Zhang*, 2004; *Rasmusson and Carpenter*, 1982; *Zhang et al.*, 1997], however, what drives this variability and its impact on the climate system on longer time scales, particularly centennial, remains less certain.

The relative importance of external forcing versus internal variability for the EEP is unclear [*DiNezio et al.*, 2013; *Hoerling et al.*, 2010; *Karnauskas et al.*, 2012]. External forcing refers to changes that originate from outside the tropical Pacific such as radiative forcing (solar and volcanic) and high latitude temperatures, whereas internal variability is intrinsic or chaotic variability of the equatorial Pacific. Internal variability of the EEP cold tongue, rather than external forcing has been suggested to explain sea surface temperature (SST) changes in the last 30-60 years [*DiNezio et al.*, 2013; *Hoerling et al.*, 2010]. Unforced GCM millennial runs support the importance of internal variability

[*Karnauskas et al.*, 2012; *Wittenberg*, 2009]. Additionally, turbulent mixing has been shown to affect the seasonal SST in the equatorial cold tongue by as much as 2˚C [*Moum et al.*, 2013]. Although turbulent mixing is thought to be important on short timescales, it may influence SST enough such that it suppresses the affects of external forcing on SST. Internal variability and turbulent mixing in the EEP are not mutually exclusive; both may be working together to inhibit or augment the influence of external forcing.

Currently, our understanding of how the Pacific varies on centennial time scales depends primarily on models, which suggest that the dynamics are different from observed interannual and decadal variability [*Collins et al.*, 2010; *DiNezio et al.*, 2009; *Karnauskas et al.*, 2012; *Sen Gupta et al.*, 2012]. On interannual time scales the tropical Pacific is not in steady state which allows for a strong coupling between the wind field and upper water column temperatures, strengthening the Bjerknes feedback [*DiNezio et al.*, 2011]. In contrast, on centennial time scales the ocean reaches steady state and the tropical Pacific undergoes basin wide adjustments [*DiNezio et al.*, 2009]. Unforced models predict that centennial variability in the tropical Pacific can cause the zonal SST gradient to vary by as much as 0.5˚C and cause a change in the subsurface with the western equatorial Pacific (WEP) warming while the EEP cools [*Karnauskas et al.*, 2012]. During model experiments where CO_2 is doubled to 560 ppm, SST increases across the tropical Pacific, the thermocline shoals and the tilt of the thermocline is reduced [*DiNezio et al.*, 2009]. These 2xCO_2 model results are driven by a decrease in easterly winds due to increased evaporation and humidity [*DiNezio et al.*, 2009], whereas the unforced centennial variability is related to changes in the easterly winds driven by the east-west SST gradient [*Karnauskas et al.*, 2012].

Here we present multidecadal resolution SST and subthermocline temperature (STT) records from the EEP using sediment cores from the Peru Margin (KNR1955 16MC-A and 14GGC, 3˚ 45'S, 81˚ 08' W, 374 m water depth, Figure 4-1). Because the data span the last 2,000 years the findings are relevant to current climate conditions as the orbital forcing and ice sheets are similar to today. The multidecadal resolution allows us to focus on centennial time scales and to examine the importance of internal variability versus external forcing EEP. Additionally, by comparing these data to previously published data we examine the role of the EEP in global climate anomalies and ENSO modulations.

4.3 Hydrography

Surface hydrography in the EEP south of the equator varies between the warm wet season (December-March) and the cold, dry season (July-September) (Figure 4-2) [*Garces-Vargas et al.*, 2005; *INOCAR*, 2005; *Twilley et al.*, 2001]. From July to September the Northern Hemisphere heats up and the Intertropical Convergence Zone (ITCZ) moves north resulting in stronger along shore winds [*Mitchell and Wallace*, 1992], increased upwelling [*Fiedler*, 1994] and a strong front along the equator marking the boundary between the cool water in the south and the warmer water from the Panama Basin [*Chelton et al.*, 2001; *Raymond et al.*, 2004]. The surface temperature is 19˚C and decreases to about 15˚C at 100 m [WOA09, *Locarnini*, 2009]. During the warm season (December to March), cross equatorial winds weaken and upwelling is reduced (Figure 4-2). The temperature increases to ~23.5˚C at the surface and decreases to ~14.5˚C at 100 m [WOA09, *Locarnini*, 2009].

The main surface current at the core site is the recently documented Ecuador-Peru Coastal Current (EPCC) which flows southward north of 5˚S and reaches as deep as 200

meters [*Chaigneau et al.*, 2013]. This has also been referred to as the El Niño Current [*Delecluse et al.*, 1998]. However, the El Niño Current was theorized to occur primarily during the warm season when the along shore winds are weaker whereas the EPCC appears to be present year round. The EPCC is associated with the surfacing of the Equatorial Under Current (EUC) and carries equatorial subsurface water and equatorial surface water [*Chaigneau et al.*, 2013] [*Lukas*, 1986]. Although the EPCC is present year round, it is strongest between April and June [*Chaigneau et al.*, 2013], which is when Lukas [1986] documented high salinity values associated with the EUC in the region. It is not clear what drives the EPCC; it may be related to Kelvin waves, or wind stress curl or some combination of both [*Chaigneau et al.*, 2013]. In the subsurface, Tsuchiya Jets, or eastward flowing currents are present below the EUC and off the equator centered around 5˚S (Figure 4-2) [*Johnson and Moore*, 1997].

The water in the EUC and below is transported to the core region through two main pathways, the interior pycnocline flow and the western boundary currents [*Johnson and McPhaden*, 1999; *Lee and Fukumori*, 2003; *Qu et al.*, 2009]. The transport between the western boundary currents and the interior is variable and related to the wind [*Lee and Fukumori*, 2003; *Zilberman et al.*, 2013]. Enhanced equatorial winds cause increased interior flow and decreased western boundary though the two partially compensate for each other [*Lee and Fukumori*, 2003]. The water below the main thermocline originates largely in southern and northern subtropical mode waters, though the Southern Hemisphere is the dominant contributor [*Johnson and McPhaden*, 1999; *Lee and Fukumori*, 2003; *Qu et al.*, 2009]. On multi-decadal to centennial time scales the source water to this region has been traced back to Subantarctic Mode Water [*Qu et al.*, 2009;

Toggweiler et al., 1991].

Although the core is located close to the coast, it does represent regional EEP hydrographic variability. Using NOAA's extended reconstructed SST (ERSST), which is based on historical measurements [*Smith et al.*, 2008], we find that correlations between the core site and other global grid points show that SST near the core site and the SST of the equatorial Pacific cold tongue are strongly correlated (r~0.7) even after ENSO variability is filtered out (Figure 4-3). This implies that although the core site is close to the coast, the SST is varying similarly to the rest of the cold tongue. In the subsurface, buoy temperature data from 100 m at 110˚W, 2˚S and from 75 m at 81˚W, 2˚S are significantly correlated ($r=0.4$, $p<0.01$) and after removing the seasonal signal the correlation increases to 0.89 ($p<0.01$) (Figure 4-4). These data support the contention that the core site is representative of the larger EEP to the west.

4.4 Methods

4.4.1 Coring and Age Model

The complete records are based on two cores, the multi-core, 16MC-A, which the preserves the sediment water interface (58 cm) and the longer gravity core, 14GGC (218 cm). The two core were spliced together by using the complete multi-core and then using data from the gravity core beginning at 13 cm or 1460 CE, which is when the multi-core ends based upon the radiocarbon date from the bottom of the multi-core.

The age model is based on 8 radiocarbon dates (Table 4-1) with 6 dates from 14GGC, and 2 dates from 16 MC. The radiocarbon dates were measured on *Neogloboquadrina dutertrei* at the WHOI AMS facility. The radiocarbon ages were converted to calendar ages by applying a 500 year reservoir age and then using the Fairbanks et al. [2005] calibration. The reservoir age is a best estimate based on a

combination of all relevant data. Coral radiocarbon data from the Galapagos calculate an average surface reservoir age of 340 years, but it varies by as much as 100 years throughout the 300 year record [*Druffel et al.*, 2007]. Similarly, a gastropod shell from Guayaquil, Ecuador indicates that the reservoir age is 385 years [*Taylor and Berger*, 1967]. In contrast, the reservoir age model of Butzin et al. [*Butzin et al.*, 2005] estimates that the reservoir age is 540 years. Thus, the range for the reservoir age is between approximately 350 and 550 years. The presence of the Suess effect, which represents a decrease in the $\Delta^{14}C$ of atmospheric CO_2 due to the burning of fossil fuels [*Tans et al.*, 1979], is indentified in the core by the decrease in $\delta^{13}C$ in both *N. dutertrei* and organic carbon (Figure 4-5). This helps to constrain the reservoir age. The decrease in $\delta^{13}C$ in both records occurs at 10.5 cm and corresponds to a calendar date 1840 CE using a reservoir age of 350 years. This is too early compared to the atmospheric change in $\delta^{13}C$ and the Suess effect measured in corals [*Druffel and Suess*, 1983; *Francey et al.*, 1999]. Using a reservoir age of 450 and 550 places the initiation of the Suess effect at 1910 and 1930, respectively, which is closer to what is expected based on coral measurements [*Druffel and Suess*, 1983]. At this time it is difficult to constrain the reservoir age between 450 and 550 years, and such, an average of the two was used in calculating the age model and was assumed not to vary through the 2500 year record.

The largest error in the age model is due to the reservoir age. The *N. dutertrei* data are plotted using a reservoir age of 450 and 550 years to illustrate the difference in the age model caused by the uncertainty in the reservoir age (Figure 4-4). Throughout most of the record the difference is about 100 years, however, by 1700 the difference is only approximately 20 years. This is because the multi-core is forced by the top of the core,

which has been set to the year the core was recovered, 2009. Support for using the recovery year for the age at the top of the core is provided by the presence of the Suess effect at 10.5 cm, suggesting about 100 years have past since its the initiation.

4.4.2 Analytical methods

Subthermocline temperature measurements are based on the Mg/Ca values of *N. dutertrei*, which is a thermocline dwelling, non-symbiont planktonic species of foraminifera and is often associated with upwelling [*Mohtadi et al.*, 2009; *Thunell and Reynolds*, 1984]. Approximately 15-20 *N. dutertrei* tests (500-750 μg of calcite) from the 355-425 μm size fraction, were crushed lightly between glass slides. The calcite pieces were then mixed and split for trace metal analysis (~400 μg) and isotope analysis (~100-150 μg). For trace metal and isotope analysis 16MC was sampled every cm and the 14GGC was sampled every other cm. The foraminifera used for trace metal analysis were cleaned according the method outlined in Barker et al. [*Barker et al.*, 2003] with a reductive cleaning [*Rosenthal et al.*, 1997]. The samples were dissolved in 100 μL of 0.065 M HNO_3 and diluted with 300 μL of 0.5 N HNO_3, such that the final calcium concentrations ranged from 2.5-5.5 mM.

Trace metal ratios were determined at Rutgers University, using a Thermo Finnigan Element XR sector-field inductively couple mass spectrometer (ICP-MS). In addition to Mg/Ca ratios, Al/Ca, Fe/Ca, Mn/Ca and Ti/Ca were measured to monitor for possible contamination from oxides and silicates. The samples were corrected for the interference of Sr^{86++} on Ca^{43}, the matrix effect of variable Ca concentration, and instrumental drift [*Andreasen et al.*, 2006; *Rosenthal et al.*, 1999]. Samples were then converted into mmol/mol ratios using a spiked gravimetric standard, which has a Mg/Ca value of 6.34 mmol/mol [*Rosenthal et al.*, 1999]. The Mg/Ca matrix correction was

always less than 2% of the original value. The long term precision of the data is based upon the replication of three in house consistency standards with Mg/Ca values as follows: CS1: 1.44 mmol/mol, CS2: 3.49 mmol/mol, and CS3: 3 8.71 mol/mol. For the time period of the data presented in this paper, the standard deviations were 0.83%, 0.71% and 0.66% respectively. No samples indicated signs of contamination and thus none were eliminated.

Isotope analyses were measured at Rutgers University on a Micromass (FISONS) Optima Mass Spectrometer. The samples were drift corrected if necessary using an in house standard. The working standard is run against the international NBS19 [*IUPAC*, 1994] biannually. The standard deviation was ±0.05‰ for $\delta^{13}C$ and ±0.1‰ for $\delta^{18}O$ throughout all the runs. Isotope values are reported in relative to the PDB standard.

Alkenones were extracted from 0.8-1.0 g of freeze dried sediment using a Dionex 200 accelerated solvent extractor. The samples were then analyzed with a Gas Chromatograph with flame ionization detector using a method modified from Herbert et al. [*Herbert et al.*, 1998]. The long term error is ±0.2˚C based on repeat analysis of a composite sediment sample, whereas the replicates were always better than ±0.1˚C. All the alkenone measurements were made at Brown University in Dr. Tim Herbert's lab. Total alkenone concentration, C_{37}tot, is the total C_{37} di- and triunsaturated ketone measured relative to mass of dried sample. The total C_{37} was normalized to an internal standard. Both 14GGC and 16MC were sampled every cm for alkenone SST and tot C_{37} analysis.

4.5 Temperature Calibrations

The Prahl et al. [1988] calibration was used to calculate SST from the Uk'37 ratio. A larger regional core top calibration using the Uk'37 to temperature relationship

based on data in Kienast et al. [2012] was also tested. This produced temperatures that were 0.05˚C cooler than the Prahl et al. [1988] calibration. Because the difference between a regional EEP and the Prahl et al. [1988] calibration was less than the analytical error in the temperature measurements, the Prahl et al. [1988] calculation was used in order to be more comparable to other data sets using the same calibration.

Comparing the alkenone temperatures to the ERSST data, indicates the alkenone temperatures are biased to the warmer season although the alkenone SST reconstructions likely capture general temperature trends (Figure 4-6). During the past 150 years, the alkenone SST average is 23.6 ± 0.1 (1σ)˚C whereas the annual average of the ERSST data is 22.8 ± 1.9 (1σ)˚C. The alkenone SST is closest to, albeit still higher than, the April-June (AMJ) seasonal average of 23.2±1.3 ˚C (Figure 4-6). This would suggest that cocolithophore blooms, which produce the alkenones used in the SST reconstruction, occur more frequently or are larger between April and June. To our knowledge, there is only one study of the annual cycle of coccolithophores from the region and it showed that coccolithophore cell counts were highest in the surface layer in February, May and June during 1999 [*Tapia*, 2007]. Although the evidence suggests that alkenone SST are biased towards AMJ temperatures, annual average ERSST temperatures are strongly correlated to AMJ temperatures of all the seasons ($r=0.88$, $p<0.001$). Based on this comparison, we conclude the alkenone SST are likely recording general temperature trends throughout the record. A similar conclusion was reach based on a model proxy comparison for the last 21 kyr [*Timmermann et al.*, 2014]. Lastly, it is important to note the alkenone SST appear to be smoothed throughout the time series likely due to bioturbation and slow

sinking rate. Only variability longer than 200 years will be interpreted because the autocorrelation is 170 years.

The *N. dutertrei* calibration was discussed in more detail previously (Chapter 3). To summarize, *N. dutertrei* is estimated to calcify at a depth of ~125 m and the Anand et al. [2003] multi species calibration was determined to produce the most realistic temperatures. The error on the temperature reconstruction is ±1.3˚C and the temperature anomaly has an error of ±1.1˚C. The smoothed data are 3 point running averages which reduces the error to ±0.8˚C.

4.6 Downcore Records

The SST record exhibits an overall increasing trend of approximately 0.8˚C throughout the entire record (Figure 4-7). Early in the record, between 150 BCE and 250 CE, temperature increases approximately 0.5˚C and then decreases again by 550 CE. Between ~550 and 1450, temperature increases by approximately 0.6˚C to a record high of 23.8˚C. Temperature then decreases to 23.5˚ by 1600 and remains there until approximately 1815. For the last 200 years there are small variations in the SST record, but by no more than 0.2˚C, which is not significant given this is within 2σ error of the analysis.

The STT reconstruction shows higher variability (Figure 4-7) than the SST reconstruction. Prior to 1200 CE, temperature varies between 14 and 12˚C. Between ~1200 and 1400 CE the temperature decreases to between 10.5 and 11.5˚C but returns to 12˚C by 1400 CE. Between 1450 and 1800 CE STT are on average 0.3 ± 0.1˚C cooler than prior to 1000 CE. After 1800 CE STTs increase by ~1.5˚C during the next 200 years suggesting the last century STT exceeds by at least 1°C any time in the two millennia period before that. Although migration of *N. dutertrei* in the water column cannot be

eliminated as a cause for temperature variability, the $\delta^{13}C$ record suggests that migration is not the primary cause for the subsurface temperature change. If the variability were associated with migration, we would expect to see an increase in $\delta^{13}C$ (lower nutrient concentration) as *N. dutertrei* moved closer to the surface resulting in warmer temperatures; this pattern is not seen at any time during the record (Figure 4-7).

The $\delta^{13}C$ is a proxy for nutrient concentrations, whereby lower $\delta^{13}C$ values are associated with increased nutrients and older water masses, and C_{37}tot is a proxy for coccolithophore productivity. The $\delta^{13}C$ of *N. dutertrei* varies between 1.2 and 1.4 ‰ until 1650 CE. Between 1650 and 1900 CE $\delta^{13}C$ decreases by ~0.2‰ (Figure 4-7). The decrease beginning at ~1900 is associated with the Suess effect (see Age Model). Throughout the record the C_{37}tot varies between 4 and 8 nmol/g with low concentrations between -310- -70 BCE, 1000-1200 CE and 1650-1800 CE and a noticeable increase between 1300-1650 CE (Figure 4-7). Although increased nutrients are typically associated with increased productivity, the C_{37}tot and $\delta^{13}C$ of *N. dutertrei* are decoupled in this respect.

4.7 Discussion

4.7.1 Sea Surface Temperature

The EEP SST record does not indicate significant warming during the Medieval Climate Anomaly (MCA) nor cooling during the Little Ice Age (LIA) (Figure 4-8). The relatively small SST changes and the absence of any significant influence of the MCA and LIA is in agreement with another temperature reconstruction from the region which is based upon a diatom index from Lake El Junco in the Galapagos [*Conroy et al.*, 2009]. Additionally, SSTs do not respond to changes in total solar irradiance (TSI) or periods of

large volcanic eruptions (Figure 4-8). The absence of response to Northern Hemisphere temperatures, TSI and volcanic eruptions is consistent with multidecadal observational and model results that indicate the EEP has relatively large internal variability, such that external forcing, unless sufficiently strong, does not impact the EEP [*DiNezio et al.*, 2013; *Hoerling et al.*, 2010].

The long term warming trend in the SST record is not found in other 2,000 year SST records from various global sites suggesting it may be a regional signal [*McGregor et al.*, 2007; *Mohtadi et al.*, 2007; *Oppo et al.*, 2009]. Increasing boreal winter insolation (December-February) has been hypothesized to be the cause for increasing alkenone SST during the Holocene [*Leduc et al.*, 2010; *Timmermann et al.*, 2014]. This implies that the increase in SST may be related to precessional changes, though the radiative forcing would only be 5.4 W/m^2 over the 2,500 year period. Further, the entire Holocene SST record does not show a monotonic increase for the last 10,000 years indicating that precession is not the dominant forcing on SST in this region. The increase in greenhouse gases, particularly methane, during the last 2,000 years [*Meure et al.*, 2006] may have contributed to the SST warming trend, but this radiative forcing is relatively small suggesting that another process may be important.

Southward transport of equatorial surface water from the EEP warm pool, located north of the equator, could explain the long term warming trend in the SST record. Current understanding of the EPCC and what controls its variability remains unclear, making difficult any inferences as to past changes. Nonetheless, if weaker along-shore winds are responsible, in-part, for increased influence of this coastal current as Philander and Delecluse [1983] predicted, then the SST warming would have likely been

accompanied by a southward migration of the ITCZ. Precipitation reconstructions in the tropical Pacific do not support a continual southward migration of the ITCZ during the last 2,000 years however [*Conroy et al.*, 2008; *Sachs et al.*, 2009; *Tierney et al.*, 2010; *Yan et al.*, 2011]. As our understanding of the EPCC improves we likely will be able to better explain the long term trend of SST in the region.

4.7.2 Subthermocline Temperatures

Unlike SST, subthermocline temperatures (STTs) indicate the influence of external forcing (Figure 4-8). In several different compilations of Northern Hemisphere temperature anomalies the coldest temperatures in the last 2000 years occurred during the Little Ice Age between 1450 and 1850 CE [*Hegerl et al.*, 2007; *Mann et al.*, 2008; *Moberg et al.*, 2005]. Using 1450 CE as a reference point, the average STT is approximately 0.3±0.1˚C colder between 1450-1800 CE than prior to1000 CE suggesting a close link between the EEP STT and Northern Hemisphere climate. We also note that the last century STT exceeds the temperatures in the preceding 2000 years record. Within the error of the age model, the coldest STTs occur during a period of several large volcanic explosions and the Wolf solar minimum, both of which decreased radiative forcing (Figure 4-8) [*Crowley and Unterman*, 2013; *Gao et al.*, 2009; *Steinhilber et al.*, 2012]. Due to the uncertainty associated with the reservoir age, it is not possible to accurately determine if cool STTs are driven by large volcanic eruptions, TSI minimum or some combination of both.

Sea surface temperatures do not show the same response as the STTs implying that the effects of the various forcings are not being transported to the subsurface from the overlying surface. More likely, the signal is propagating from the subtropics. Modern observations and modeling studies suggest that climate perturbations are effectively

transmitted to the equatorial Pacific along isopycnal layers primarily in the form of density compensated changes in temperature and salinity (i.e., spiciness) [*Kolodziejczyk and Gaillard*, 2012; *OKane et al.*, 2014]. Within the uncertainty of our method, down core STT changes appear to be density compensated (Appendix 4-1), supporting the hypothesis that the cool STTs originate in the subtropics and travel to the base of the equatorial thermocline.

The warming at the end of the STT record precedes Northern Hemisphere temperature anomalies (Figure 4-8), however, changes in several other tropical Pacific reconstructions, including increasing Indo-Pacific Warm Pool (IPWP) SST [*Oppo et al.*, 2009], decreasing EEP [*Sachs et al.*, 2009] and South American precipitation [*Bird et al.*, 2011] and increasing Andean temperature [*Kellerhals et al.*, 2010], all occur around the same time. This is consistent with intrinsic centennial variability in the equatorial Pacific related to changes in the Walker circulation seen in climate models [*Karnauskas et al.*, 2012]. Sea surface temperature records from the IPWP [*Oppo et al.*, 2009] and the EEP (this study) indicate an increasing zonal gradient corresponding to a strengthening of the Walker circulation. The models suggest that during periods of stronger Walker circulation STTs in the EEP are cool due to a shoaling of the thermocline. In contrast, our STT reconstruction shows warm temperatures. Enhanced Walker circulation would also cause greater convergence of water in the thermocline causing the thermocline to deepen which would explain the STT increase. Increased convergence in the thermocline is supported by the decrease of $\delta^{13}C$ values around the same time. We interpret the decrease in $\delta^{13}C$ to reflect greater contribution of east Pacific subtropical water to the region due to enhanced interior pathway transport [*Fukumori et al.*, 2004]. A stronger interior pathway

is typical during periods of stronger Walker circulation.

4.7.3 Decoupling of the SST and STT

The SST and STT variations are decoupled (Figure 4-7). Past estimates of the upwelling depth near the core site imply that *N. dutertrei* is calcifying below the maximum depth of upwelling in the region which has been estimated to be 60 m based on model and nutrient analysis [*Barber and Chavez*, 1991; *Philander et al.*, 1987]. If this is the case, the temperature and nutrient changes at the depth where *N. dutertrei* is calcifying would not influence the surface. This may explain why the increase in nutrients, indicated by the depletion of $\delta^{13}C$ of *N. dutertrei* around 1750 CE, does not correspond to an increase in productivity, represented by C_{37}tot (Figure 4-7).

Assuming that alkenone SST are comparable to the *N. dutertrei* reconstructions despite possible seasonal biases in their ecologies [*Leduc et al.*, 2010; *Timmermann et al.*, 2014], the decoupling between the surface and subsurface temperatures has implications for EEP dynamics that extend beyond local upwelling. Climatological evidence suggests that the SST at the core site is correlated with the SST of the equatorial Pacific cold tongue (Figure 4-3), whereas *N. dutertrei* reflects water conditions at the base of the thermocline (Figure 4-4). Based on these two assumptions, the decoupling between the SST and STT implies that on this time scales the water at the base of the thermocline is not influencing the overlying SST. This is difficult to reconcile because there are several observational and modeling studies showing that the upwelling of subtropical water in the equatorial region is an important component of heat transport in the ocean [*Gu and Philander*, 1997; *McPhaden and Zhang*, 2004; *Qu et al.*, 2009]. Not withstanding ecological biases, one way to reconcile the decoupling between the surface and subsurface in the proxy data is to consider the role of stratification and the temperature of

upwelled water. When the subsurface water is cooler, there is more stratification resulting in shallower upwelling, which would not cool the SST as much. In contrast, when the subsurface is warmer, there is less stratification and deeper upwelling, but the upwelled water is warmer. Because the temperature of the water being upwelled counteracts the stratification and depth of upwelling, the subsurface temperature might not have a large impact on SST.

4.8 Climate Implications

Our temperature reconstructions of SST and STT from the EEP fill a prior void in the available data and address the nature of EEP variations on centennial time scales. The SST record is characterized by a general warming trend of <1°C through the Common Era, showing no warming during the MCA or cooling at the LIA, respectively, thereby suggesting that EEP SST is not highly susceptible to external forcing, which may include anthropogenic climate change. In contrast, STT appears to follow the Northern Hemisphere climate anomalies suggesting that on multi-centennial scale the EEP sub-thermocline is likely in "thermodynamic" equilibrium with the global climate as expected on such long time scales. However, we find that the EEP subthermocline exhibits substantial multi-decadal perturbations, arguably related to radiative forcings by large volcanic eruptions and solar minima possibly affecting the dynamics of the EEP.

Heat stored in the subsurface of the equatorial Pacific has arguably been implicated in the recent hiatus in global temperatures [*England et al.*, 2014; *Kosaka and Xie*, 2013; *Meehl et al.*, 2013]. It has been argued that dynamic changes in the equatorial Pacific can explain this climate anomaly and heat storage below the thermocline has increased due to the strengthening of the subtropical cells which has enhanced the downwelling of warm subtropical water [*England et al.*, 2014; *Meehl et al.*, 2013].

Similarly, multi-decadal variability in STTs may also be driven by dynamical changes which are caused by radiative forcing. The stronger response of STTs than SSTs to radiative forcing in our record may be because radiative forcing is transient and can disappear from the surface ocean and atmosphere quickly, whereas the signal may persist in the subsurface for a long period [*Stenchikov et al.*, 2009]. Thus, this record raises the possibility that the extended response of subsurface temperature in the EEP might have acted to mediate the global response of the surface ocean and atmosphere to these abrupt forcings, through dynamic responses similar to those offered to explain the current warming hiatus.

4.9 References

Alexander, M. A., et al. (2002), The Atmospheric Bridge: The Influence of ENSO Teleconnections on Air-Sea Interaction over the Global Oceans, *Journal of Climate*, *15*(16), 2205-2231.

Anand, P., et al. (2003), Calibration of Mg/Ca thermometry in planktonic foraminifera from a sediment trap time series, *Paleoceanography*, *18*(2).

Andreasen, D. H., et al. (2006), Fidelity of radially viewed ICP-OES and magnetic-sector ICP-MS measurement of Mg/Ca and Sr/Ca ratios in marine biogenic carbonates: Are they trustworthy together?, *Geochemistry Geophysics Geosystems*, *7*.

Barber, R. T., and F. P. Chavez (1991), Regulation of primary productivity rate in the equatorial Pacific, *Journal Name: Limnology and Oceanography; (United States); Journal Volume: 36:8*, Medium: X; Size: Pages: 1803-1815.

Barker, S., et al. (2003), A study of cleaning procedures used for foraminiferal Mg/Ca paleothermometry, *Geochemistry Geophysics Geosystems*, *4*.

Barlow, M., et al. (2001), ENSO, Pacific Decadal Variability, and U.S. Summertime Precipitation, Drought, and Stream Flow, *Journal of Climate*, *14*(9), 2105-2128.

Bird, B. W., et al. (2011), A 2,300-year-long annually resolved record of the South American summer monsoon from the Peruvian Andes, *Proceedings of the National Academy of Sciences*, *108*(21), 8583-8588.

Butzin, M., et al. (2005), Radiocarbon simulations for the glacial ocean: The effects of wind stress, Southern Ocean sea ice and Heinrich events, *Earth and Planetary Science Letters*, *235*(1-2), 45-61.

Chaigneau, A., et al. (2013), Near-coastal circulation in the Northern Humboldt Current System from shipboard ADCP data,
Journal of Geophysical Research: Oceans, *118*(10), 5251-5266.

Chelton, D. B., et al. (2001), Observations of Coupling between Surface Wind Stress and Sea Surface Temperature in the Eastern Tropical Pacific, *Journal of Climate*, *14*(7), 1479-1498.

Collins, M., et al. (2010), The impact of global warming on the tropical Pacific Ocean and El Nino, *Nature Geosci*, *3*(6), 391-397.

Conroy, J. L., et al. (2008), Holocene changes in eastern tropical Pacific climate inferred from a Galapagos lake sediment record, *Quaternary Science Reviews*, *27*(11), 1166-1180.
Conroy, J. L., et al. (2009), Unprecedented recent warming of surface temperatures in the eastern tropical Pacific Ocean, *Nature Geoscience*, *2*(1), 46-50.
Crowley, T. J., and M. B. Unterman (2013), Technical details concerning development of a 1200-yr proxy index for global volcanism, *Earth Syst. Sci. Data Discuss.*, *5*(1), 1-28.
Dai, A., and T. M. L. Wigley (2000), Global patterns of ENSO-induced precipitation, *Geophys. Res. Lett.*, *27*(9), 1283-1286.
Delecluse, P., et al. (1998), Coupled general circulation modeling of the tropical Pacific, *Journal of Geophysical Research-Oceans*, *103*(C7), 14357-14373.
Deser, C., et al. (2004), Pacific Interdecadal Climate Variability: Linkages between the Tropics and the North Pacific during Boreal Winter since 1900, *Journal of Climate*, *17*(16), 3109-3124.
DiNezio, P. N., et al. (2009), Climate Response of the Equatorial Pacific to Global Warming, *Journal of Climate*, *22*(18), 4873-4892.
DiNezio, P. N., et al. (2011), The response of the Walker circulation to Last Glacial Maximum forcing: Implications for detection in proxies, *Paleoceanography*, *26*.
DiNezio, P. N., et al. (2013), Detectability of Changes in the Walker Circulation in Response to Global Warming, *Journal of Climate*, *26*(12), 4038-4048.
Druffel, E. M., and H. E. Suess (1983), On the radiocarbon record in banded corals: Exchange parameters and net transport of 14CO2 between atmosphere and surface ocean, *Journal of Geophysical Research: Oceans*, *88*(C2), 1271-1280.
Druffel, E. R. M., et al. (2007), Oceanic climate and circulation changes during the past four centuries from radiocarbon in corals, *Geophysical Research Letters*, *34*(9).
England, M. H., et al. (2014), Recent intensification of wind-driven circulation in the Pacific and the ongoing warming hiatus, *Nature Clim. Change*, *4*(3), 222-227.
Fairbanks, R. G., et al. (2005), Radiocarbon calibration curve spanning 0 to 50,000 years BP based on paired 230Th/234U/238U and 14C dates on pristine corals, *Quaternary Science Reviews*, *24*(16-17), 1781-1796.
Fiedler, P. C. (1994), Seasonal and interannual variability of coastal zone color scanner phytoplankton pigments and winds in the eastern tropical Pacific, *J. Geophys. Res.*, *99*(C9), 18371-18384.
Fiedler, P. C., and L. D. Talley (2006), Hydrography of the eastern tropical Pacific: A review, *Progress in Oceanography*, *69*(2-4), 143-180.
Francey, R. J., et al. (1999), A 1000-year high precision record of δ13C in atmospheric CO2, *Tellus B*, *51*(2), 170-193.
Fukumori, I., et al. (2004), The Origin, Pathway, and Destination of Nino-3 Water Estimated by a Simulated Passive Tracer and Its Adjoint, *Journal of Physical Oceanography*, *34*(3), 582-604.
Gao, C. C., et al. (2009), Volcanic forcing of climate over the past 1500 years: An improved ice core-based index for climate models (vol 113, D23111, 2008), *Journal of Geophysical Research-Atmospheres*, *114*.
Garces-Vargas, J., et al. (2005), Inter-annual variability in the thermal structure of an oceanic time series station off Ecuador (1990,Äì2003) associated with El Ni√±o events, *Deep Sea Research Part I: Oceanographic Research Papers*, *52*(10), 1789-1805.
Gu, D. F., and S. G. H. Philander (1997), Interdecadal climate fluctuations that depend on exchanges between the tropics and extratropics, *Science*, *275*(5301), 805-807.
Hegerl, G. C., et al. (2007), Detection of Human Influence on a New, Validated 1500-Year Temperature Reconstruction, *Journal of Climate*, *20*(4), 650-666.
Herbert, T. D., et al. (1998), Depth and seasonality of alkenone production along the California margin inferred from a core top transect, *Paleoceanography*, *13*(3), 263-271.

Hoerling, M., et al. (2010), Regional Precipitation Trends: Distinguishing Natural Variability from Anthropogenic Forcing, *Journal of Climate*, *23*(8), 2131-2145.
INOCAR (2005), De La Costa Continenta E Insular Del Ecuador, edited by E. I. O. d. l. Armada, pp. 15-16, Guayaquil.
IUPAC (1994), Commission on Atomic Weights and Isotopic Abundances, *Pure and Applied Chemistry*, *66*, 2423-2444.
Johnson, G. C., and D. W. Moore (1997), The Pacific subsurface countercurrents and an inertial model, *Journal of Physical Oceanography*, *27*(11), 2448-2459.
Johnson, G. C., and M. J. McPhaden (1999), Interior Pycnocline Flow from the Subtropical to the Equatorial Pacific Ocean*, *Journal of Physical Oceanography*, *29*(12), 3073-3089.
Karnauskas, K. B., et al. (2012), A Pacific Centennial Oscillation Predicted by Coupled GCMs, *Journal of Climate*, *25*(17), 5943-5961.
Kellerhals, T., et al. (2010), Ammonium concentration in ice cores: A new proxy for regional temperature reconstruction?, *Journal of Geophysical Research: Atmospheres*, *115*(D16), D16123.
Kienast, M., et al. (2012), Alkenone unsaturation in surface sediments from the eastern equatorial Pacific: Implications for SST reconstructions, *Paleoceanography*, *27*(1), PA1210.
Kolodziejczyk, N., and F. Gaillard (2012), Observation of spiciness interannual variability in the Pacific pycnocline, *Journal of Geophysical Research-Oceans*, *117*.
Kosaka, Y., and S. P. Xie (2013), Recent global-warming hiatus tied to equatorial Pacific surface cooling, *Nature*, *501*(7467), 403-+.
Leduc, G., et al. (2010), Holocene and Eemian sea surface temperature trends as revealed by alkenone and Mg/Ca paleothermometry, *Quaternary Science Reviews*, *29*(7,Äì8), 989-1004.
Lee, T., and I. Fukumori (2003), Interannual-to-Decadal Variations of Tropical-Subtropical Exchange in the Pacific Ocean: Boundary versus Interior Pycnocline Transports, *Journal of Climate*, *16*(24), 4022-4042.
Locarnini, R. A., A. V. Mishonov, J. I. Antonov, T. P. Boyer, H. E. Garcia, O. K. Baranova, M. M. Zweng, and D. R. Johnson (2009), Temperature, edited by N. A. N. 68, U.S. Government Printing Office, Washington D.C.
Lukas, R. (1986), The termination of the Equatorial Undercurrent in the eastern Pacific, *Progress In Oceanography*, *16*(2), 63-90.
Mann, M. E., et al. (2008), Proxy-based reconstructions of hemispheric and global surface temperature variations over the past two millennia, *Proceedings of the National Academy of Sciences of the United States of America*, *105*(36), 13252-13257.
Mantua, N., and S. Hare (2002), The Pacific Decadal Oscillation, *Journal of Oceanography*, *58*(1), 35-44.
McGregor, H. V., et al. (2007), Rapid 20th-century increase in coastal upwelling off northwest Africa, *Science*, *315*(5812), 637-639.
McPhaden, M. J., and D. Zhang (2004), Pacific Ocean circulation rebounds, *Geophysical Research Letters*, *31*(18), L18301.
Meure, C. M., et al. (2006), Law Dome CO2, CH4 and N2O ice core records extended to 2000 years BP, *Geophysical Research Letters*, *33*(14).
Mitchell, T. P., and J. M. Wallace (1992), The Annual Cycle in Equatorial Convection and Sea Surface Temperature, *Journal of Climate*, *5*(10), 1140-1156.
Moberg, A., et al. (2005), Highly variable Northern Hemisphere temperatures reconstructed from low- and high-resolution proxy data, *Nature*, *433*(7026), 613-617.
Mohtadi, M., et al. (2007), Cooling of the southern high latitudes during the Medieval Period and its effect on ENSO, *Quaternary Science Reviews*, *26*(7-8), 1055-1066.

Mohtadi, M., et al. (2009), Low-latitude control on seasonal and interannual changes in planktonic foraminiferal flux and shell geochemistry off south Java: A sediment trap study, *Paleoceanography*, *24*(1), PA1201.

Moum, J. N., et al. (2013), Seasonal sea surface cooling in the equatorial Pacific cold tongue controlled by ocean mixing, *Nature*, *500*(7460), 64-67.

OKane, T. J., et al. (2014), ENSO regimes and the late 1970s climate shift: The role of synoptic weather and South Pacific ocean spiciness, *Journal of Computational Physics*(0).

Oppo, D. W., et al. (2009), 2,000-year-long temperature and hydrology reconstructions from the Indo-Pacific warm pool, *Nature*, *460*(7259), 1113-1116.

Philander, S. G. H., and P. Delecluse (1983), Coastal currents in low latitudes (with application to the Somali and El Nino currents), *Deep Sea Research Part A. Oceanographic Research Papers*, *30*(8), 887-902.

Philander, S. G. H., et al. (1987), Simulation of the Seasonal Cycle of the Tropical Pacific-Ocean, *Journal of Physical Oceanography*, *17*(11), 1986-2002.

Prahl, F. G., et al. (1988), Further Evaluation of Long-Chain Alkenones as Indicators of Paleoceanographic Conditions, *Geochimica Et Cosmochimica Acta*, *52*(9), 2303-2310.

Qu, T. D., et al. (2009), Origin and Pathway of Equatorial 13 degrees C Water in the Pacific Identified by a Simulated Passive Tracer and Its Adjoint, *Journal of Physical Oceanography*, *39*(8), 1836-1853.

Rasmusson, E. M., and T. H. Carpenter (1982), Variations in Tropical Sea Surface Temperature and Surface Wind Fields Associated with the Southern Oscillation/El Ni√±o, *Monthly Weather Review*, *110*(5), 354-384.

Raymond, D. J., et al. (2004), EPIC2001 and the Coupled Ocean-Atmosphere System of the Tropical East Pacific, *Bulletin of the American Meteorological Society*, *85*(9), 1341-1354.

Roemmich, D., and J. Gilson (2011), The global ocean imprint of ENSO, *Geophys. Res. Lett.*, *38*(13), L13606.

Rosenthal, Y., et al. (1997), Temperature control on the incorporation of magnesium, strontium, fluorine, and cadmium into benthic foraminiferal shells from Little Bahama Bank: Prospects for thermocline paleoceanography, *Geochimica Et Cosmochimica Acta*, *61*(17), 3633-3643.

Rosenthal, Y., et al. (1999), Precise determination of element/calcium ratios in calcareous samples using sector field inductively coupled plasma mass spectrometry, *Analytical Chemistry*, *71*(15), 3248-3253.

Rosenthal, Y., et al. (2013), Pacific Ocean Heat Content During the Past 10,000 Years, *Science*, *342*(6158), 617-621.

Ryan, W. B. F., et al. (2009), Global Multi-Resolution Topography synthesis, *Geochemistry Geophysics Geosystems*, *10*.

Sachs, J. P., et al. (2009), Southward movement of the Pacific intertropical convergence zone AD[thinsp]1400-1850, *Nature Geosci*, *2*(7), 519-525.

Schlitzer, R. (2011), Ocean Data View, edited.

Sen Gupta, A., et al. (2012), Drivers of the projected changes to the Pacific Ocean equatorial circulation, *Geophysical Research Letters*, *39*.

Shackleton, N. J., and E. Vincent (1978), Oxygen and carbon isotope studies in recent foraminifera from the southwest Indian ocean, *Marine Micropaleontology*, *3*(1), 1-13.

Smith, T. M., et al. (2008), Improvements to NOAA's historical merged land-ocean surface temperature analysis (1880-2006), *Journal of Climate*, *21*(10), 2283-2296.

Steinhilber, F., et al. (2012), 9,400 years of cosmic radiation and solar activity from ice cores and tree rings, *Proceedings of the National Academy of Sciences of the United States of America*, *109*(16), 5967-5971.

Stenchikov, G., et al. (2009), Volcanic signals in oceans, *Journal of Geophysical Research-Atmospheres*, *114*.

Tans, P. P., et al. (1979), Natural atmospheric 14C variation and the Suess effect, *Nature*, *280*, 826-828.

Tapia, M. E. (2007), Variabilidad Temporal del Fitoplancton en Areas Costeras del Mar Ecuatorianso y su interrelacion con el evento La Nina 1999-2000, Ecuador, *Acta Oceanografica del Pacifico*, *14*(1), 37-48.

Taylor, R. E., and R. Berger (1967), Radiocarbon Content of Marine Shells from the Pacific Coasts of Central and South America, *Science*, *158*(3805), 1180-1182.

Thunell, R. C., and L. A. Reynolds (1984), Sedimentation of Planktonic-Foraminifera - Seasonal-Changes in Species Flux in the Panama Basin, *Micropaleontology*, *30*(3), 243-262.

Tierney, J. E., et al. (2010), Coordinated hydrological regimes in the Indo-Pacific region during the past two millennia, *Paleoceanography*, *25*(1), PA1102.

Timmermann, A., et al. (2014), Assessing divergent SST behavior during the last 21 ka derived from alkenones and G. ruber-Mg/Ca in the Equatorial Pacific, *Paleoceanography*, 2013PA002598.

Toggweiler, J. R., et al. (1991), The Peru Upwelling and the Ventilation of the South Pacific Thermocline, *J. Geophys. Res.*, *96*(C11), 20467-20497.

Twilley, R. R., et al. (2001), The Gulf of Guayaquil and the Guayas Rover Estuary, Ecuador, in *Coastal Marine Ecosystems of Latin America*, edited by U. Seeliger and B. Kjerfve, pp. 245-263, Springer-Verlag, Berlin.

Wittenberg, A. T. (2009), Are historical records sufficient to constrain ENSO simulations?, *Geophysical Research Letters*, *36*.

Yan, H., et al. (2011), A record of the Southern Oscillation Index for the past 2,000 years from precipitation proxies, *Nature Geosci*, *4*(9), 611-614.

Zhang, Y., et al. (1997), ENSO-like interdecadal variability: 1900-93, *Journal of Climate*, *10*(5), 1004-1020.

Zilberman, N. V., et al. (2013), The Mean and the Time Variability of the Shallow Meridional Overturning Circulation in the Tropical South Pacific Ocean, *Journal of Climate*, *26*(12), 4069-4087.

Table 4-1. Radiocarbon dates for the multicore and gravity core. The radiocarbon age was converted to calendar age first by subtracting a reservoir age of 500 and then using the Fairbanks et al. [2005] calibration.

Core	ID	depth (cm)	^{14}C year ± 1 sigma	calendar year ± 1 sigma
16MC-A	OS-106155	24.5	610 ±25	out of calibration age
16MC-A	OS-94332	56.5	905 ±25	483 ±28
14GGC	OS-77375	7.25	890 ±30	465 ±46
14GGC	OS-94366	25.5	1050 ±30	550 ±30
14GGC	OS-94331	75.5	1700 ±35	1118 ±53
14GGC	OS-77582	100.25	1860 ±45	1285 ±26
14GGC	OS-94370	151.5	2330 ±35	1763 ±48
14GGC	OS-77376	200.25	2860 ±35	2357 ±33

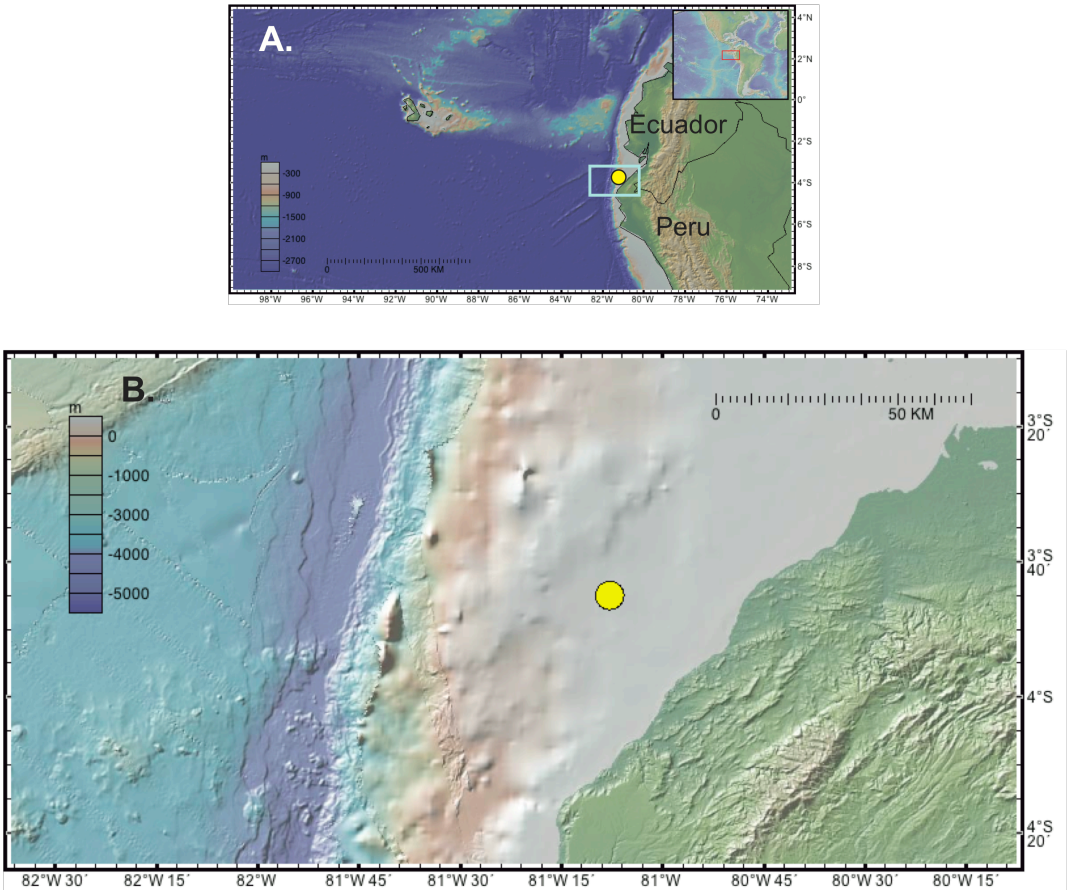

Figure 4-1. (A) Location of core discussed in this chapter (yellow circle) (B) Expanded view of light blue box in (A), showing detail of bathymetry in region of core location. Figures generated using geomapapp.org

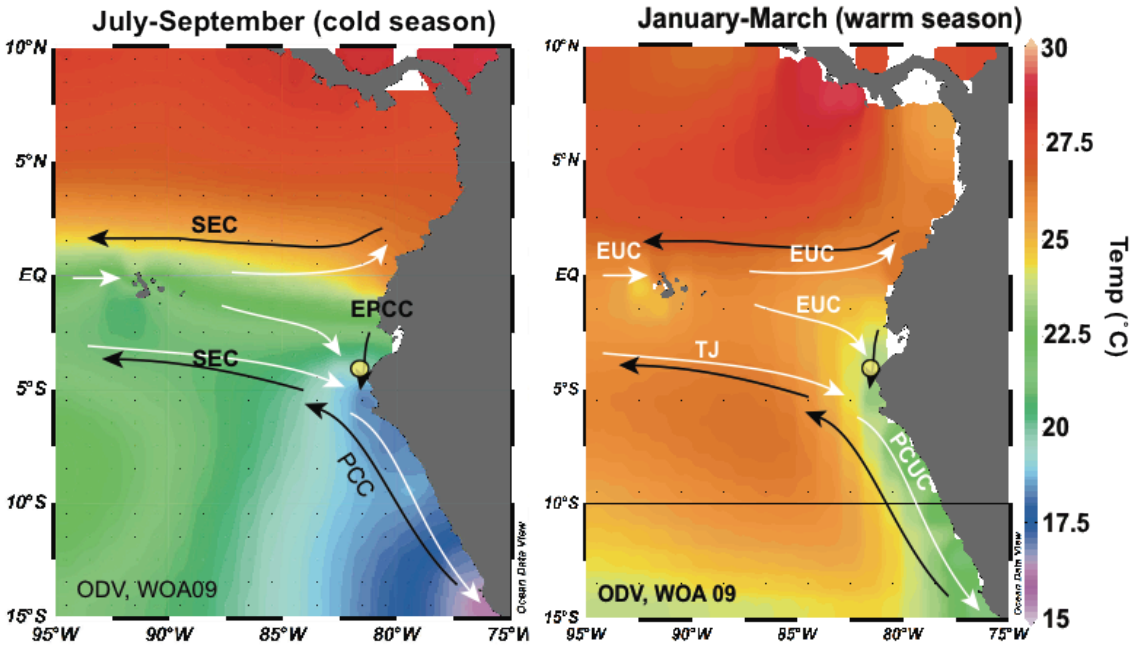

Figure 4-2. Seasonal SST map with the surface (black arrows) and subsurface (white arrows) circulation, for cold (left) and warm (right) seasons. Core site is indicated by yellow circle. SEC: Southern Equatorial Current, EPCC: Ecuador Peru Coastal Current, PCC: Peru Chile Current, EUC: Equatorial Undercurrent, TJ: Tsuchiya jet, PCUC: Peru-Chile Undercurrent. The SST images were made with ODV [*Schlitzer*, 2011] using the data from World Ocean Atlas 2009 [*Locarnini*, 2009]

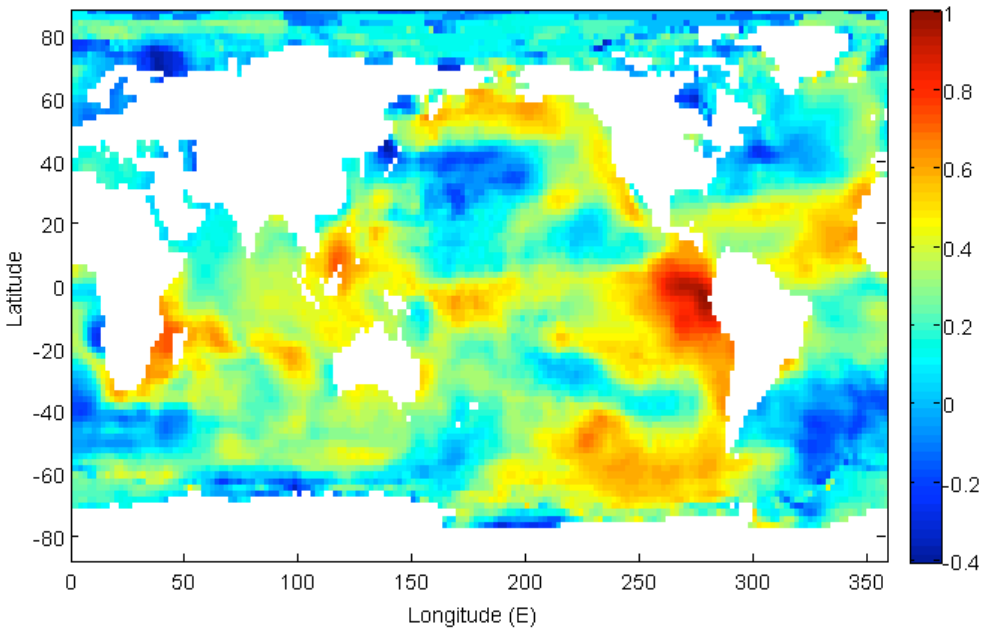

Figure 4-3. Correlation between the 8 year filtered SST record from 4˚S, 82˚W and the 8 year filtered SST from each grid point over the globe. Color bar indicates correlation coefficient. The SST data are from NOAA extended reconstructed SST data set [*Smith et al.*, 2008]. The data were filtered at 8 years to remove ENSO variability.

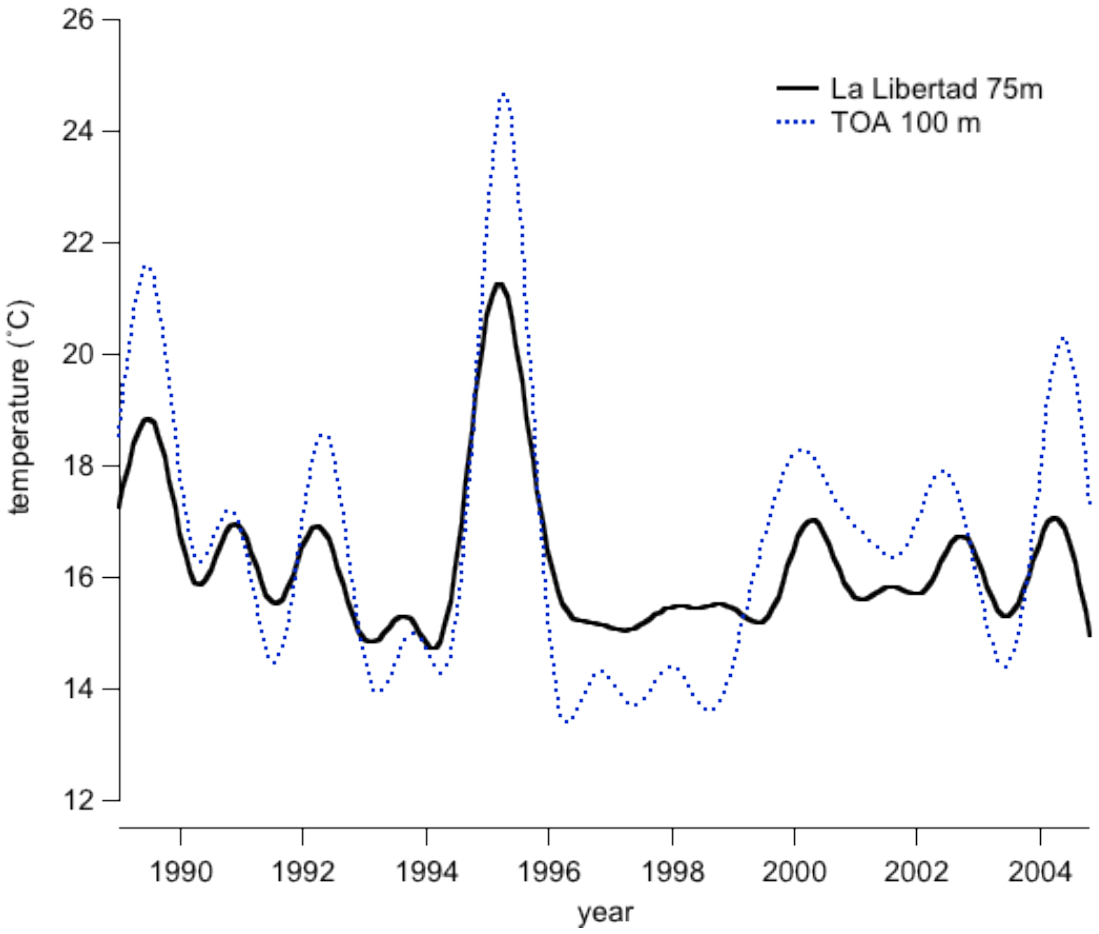

Figure 4-4. Buoy temperature data from 75 m depth at station La Libertad (2˚S, 81˚W) located near the core site (black line), plotted with TOA buoy temperature data from 100-m depth at 110˚W, 2˚S (http://www.pmel.noaa.gov/tao/). Depths of both data sets are below the main thermocline [*Fiedler and Talley*, 2006]. The records were filtered to remove the seasonal cycle. The correlation between the two filtered temperature records is 0.89 ($p<0.01$)

.

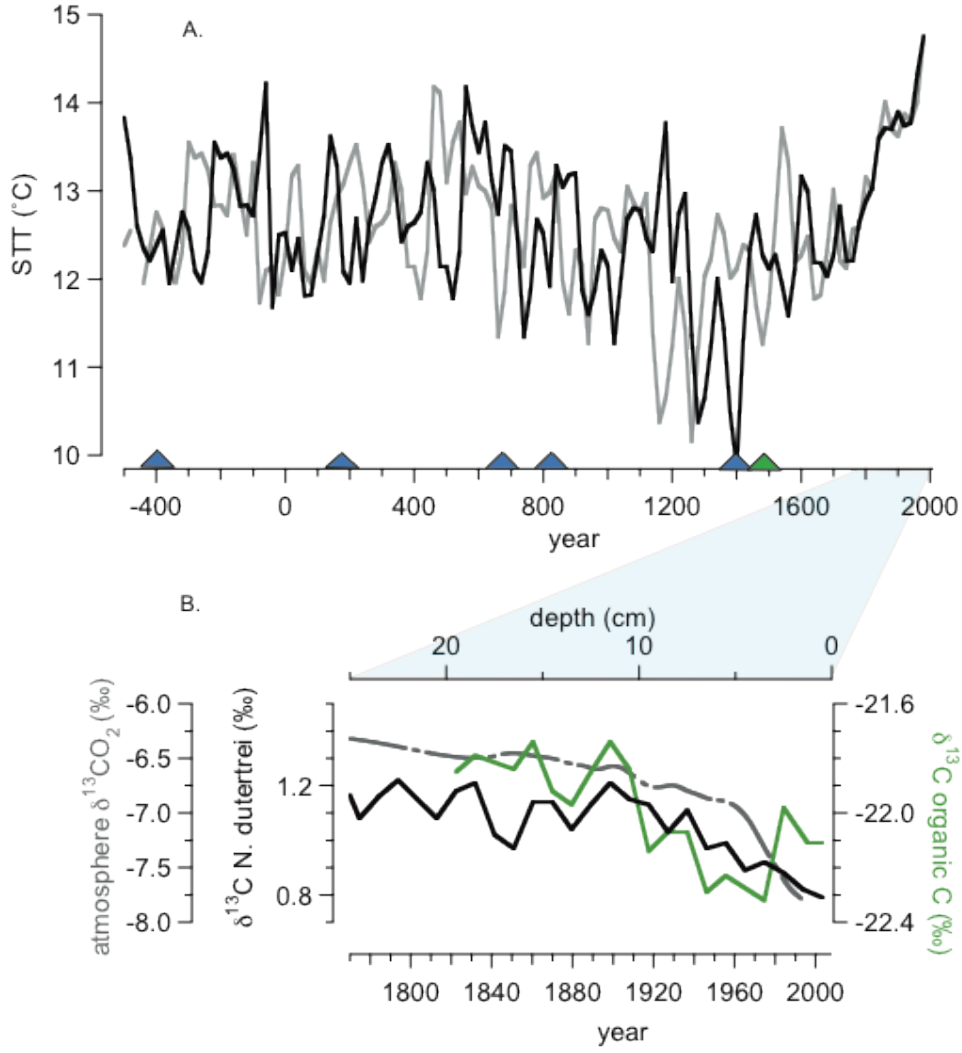

Figure 4-5. (A) *N. dutertrei* sub-thermocline temperature (STT) averaged data is plotted using a 550 year reservoir age (black) and a 450 year reservoir age (grey). The triangles mark the depths or radiocarbon dates (B) The $\delta^{13}C$ of organic carbon (green) and *N. dutertrei* (black) are plotted versus age and depth. The grey dashed line is the atmospheric $\delta^{13}CO_2$ [*Francey et al.*, 1999].

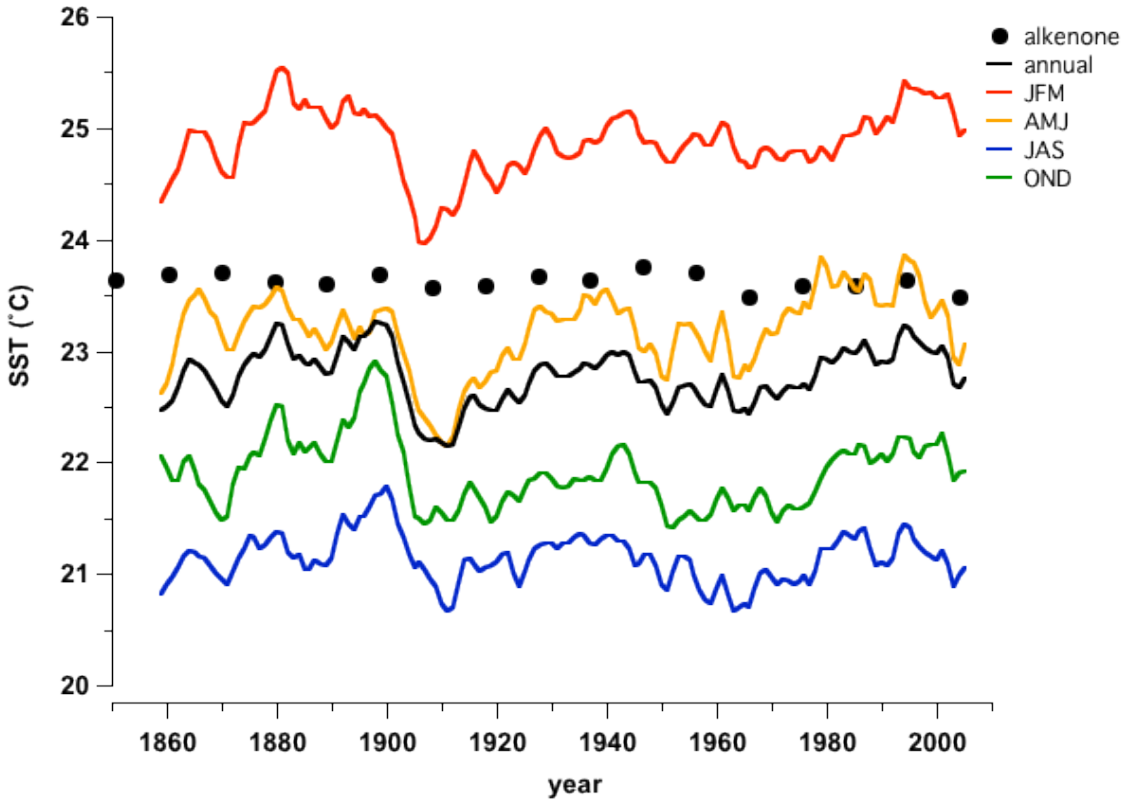

Figure 4-6. Alkenone SST estimates based on the calibration of Prahl et al (1988) (black circles) are compared with the 10 year smoothed SST data for different seasons. The SSTs represent the average of two grid points, 82˚W, 2˚S and 82˚W 4˚S, from the ErSST data set [*Smith et al.*, 2008]. The black line is the average annual temperature and the different colors represent the different seasons

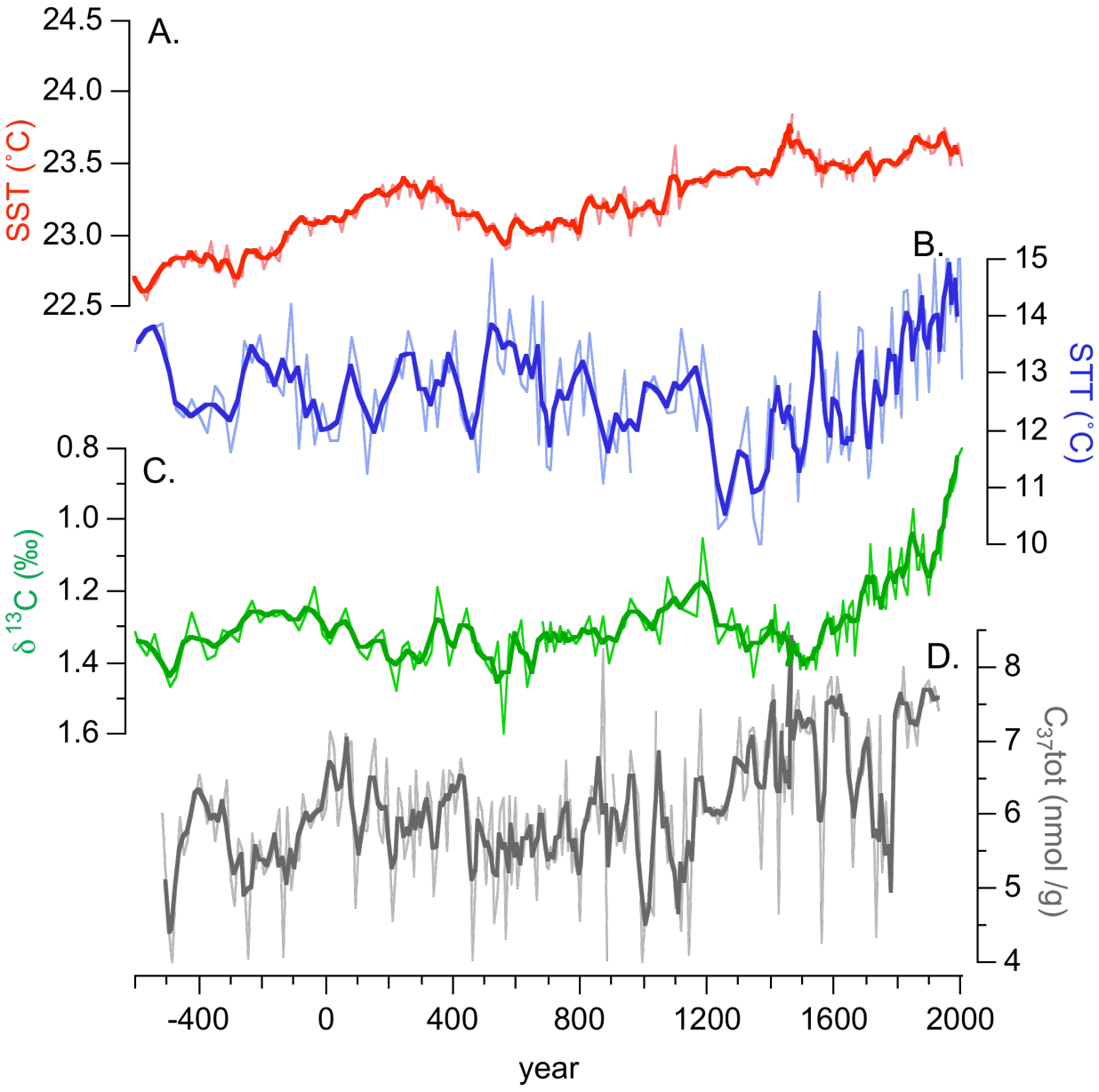

Figure 4-7. Individual (thin lines) data and 3-point running averages (thick lines) are plotted for (A) alkenone SST, (B) *N. dutertrei* Mg/Ca subthermocline temperature (STT), (C) *N. dutertrei* $\delta^{13}C$ and (D) C_{37}tot. Note the difference in temperature scale for the alkenone SST reconstruction and the *N. dutertrei* STT reconstruction.

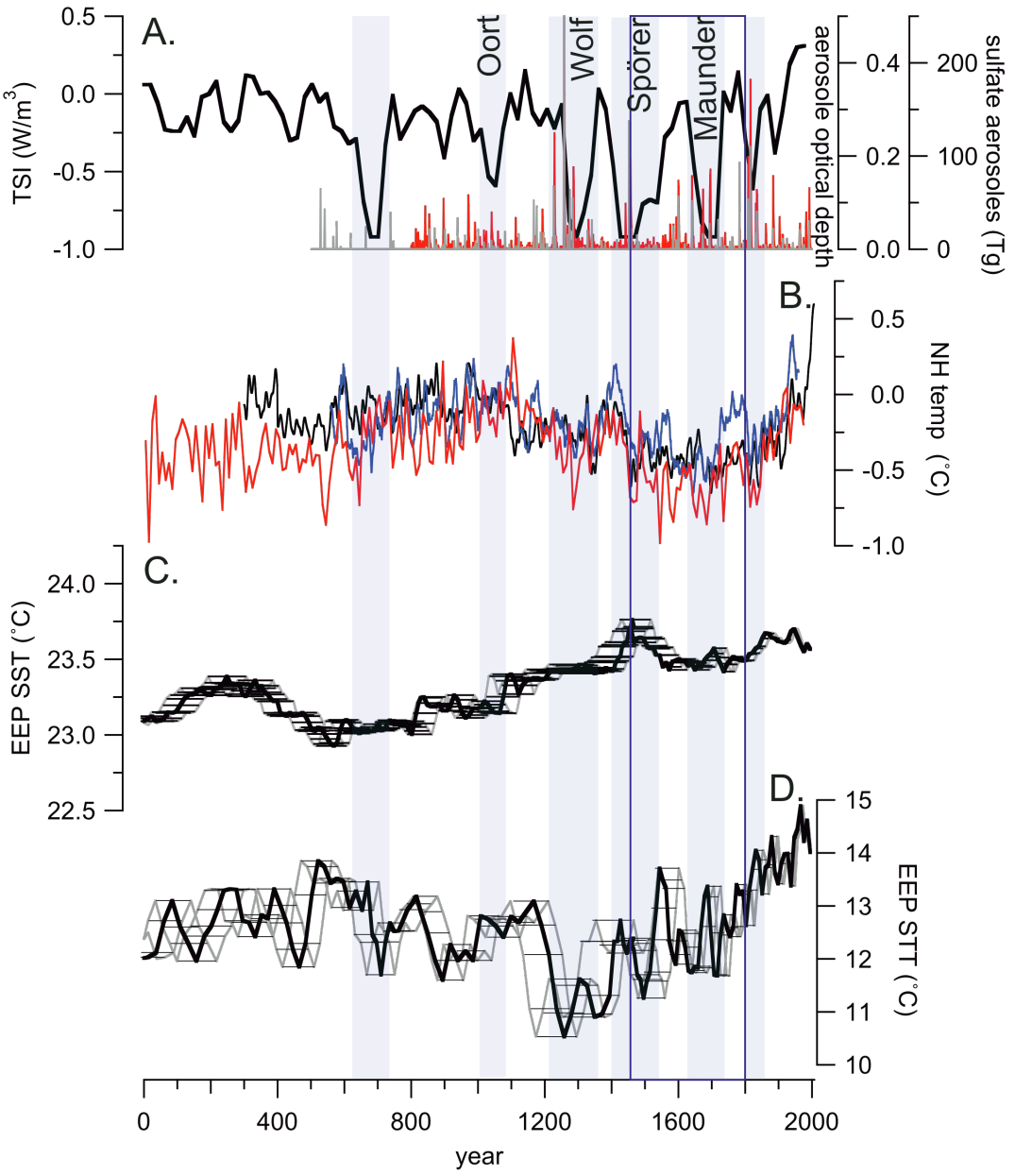

Figure 4-8. A) TSI [*Steinhilber et al.* 2011], volcanic eruption reconstructions [*Gao et al.* 2009 (grey) *Crowley and Unterman* 2013 (red)] and (B) Northern Hemisphere temperature anomalies [*Mann et al.* 2008 (black), *Moberg et al.* 2005 (red), *Hegerl et al.* 2007 (blue)] are plotted with (C) EEP SST and (D) STT records. The grey lines and horizontal error bars on the EEP temperature records represent the uncertainty in the age model due to the reservoir age. Periods of reduced radiative forcing, whether from reduction in TSI or from large volcanic eruptions, are shaded in grey. The blue box indicates 1450-1800 CE and is representative of the time period used to calculate average STT during Little Ice Age.

CHAPTER FIVE

FRESHWATER CONTROLS ON THE INDONESIAN THROUGHFLOW THERMOCLINE DURING THE LAST 2000 YEARS

5.1 Abstract

The Indonesian throughflow (ITF) transports heat and freshwater between the Pacific and Indian Oceans with the main transport occurring in the thermocline. Throughout the observational record, seasonally alternating monsoonal winds and interannual El Niño Southern Oscillation (ENSO) modulations drive freshwater from the South China Sea into the ITF, which affect the velocity, depth and temperature of the transport. Here we reconstruct ITF thermocline water temperatures (TWTs) in the Makassar Strait over the last 2,000 years using Mg/Ca of the thermocline-dwelling foraminifera *Neogloboquadrina dutertrei* to determine centennial variability and evaluate the causes of this variability. Throughout the record TWTs vary between ~ 20 and 24˚C which is comparable to the range of thermocline temperatures in modern observations. Although TWTs do not closely follow Northern Hemisphere temperatures, TWT are generally warm during the Medieval Climate Anomaly (MCA) and cool by ~1.3±0.1°C during the Little Ice Age (LIA). We argue that the location of the Intertropical Convergence Zone (ITCZ) is driving the TWTs variability by affecting the freshwater input from the South China Sea through changes in the regional winds. During the MCA when the ITCZ was farther north, conditions are more similar to the East Asian Summer Monsoon limiting the freshwater input into the ITF causing TWTs to increase. In contrast, during the LIA when the ITCZ is farther south and conditions are more similar to the East Asian Winter Monsoon freshwater flow into the ITF is enhanced causing the TWTs to decrease. The transition between the MCA and LIA is also marked by

decreased amplitude and increased frequency of TWT variability. The variability in TWT during the LIA corresponds to changes in precipitation and total solar irradiance. Using previously published sea surface temperature and intermediate water temperature reconstructions along with the TWT reconstruction presented here, we estimate that temperature weighted transport was approximately 1˚C warmer and heat transport was between 0.04-0.1 PW higher during the MCA compared to the LIA.

5.2 Introduction

As part of the global thermohaline circulation, the Indonesian throughflow (ITF), is the only equatorial inter-ocean connection transferring heat and freshwater between the Pacific and Indian Oceans. Transporting ~0.53 Pettawatts (PW) [*Tillinger and Gordon*, 2010] the ITF plays a major role in the heat budget of the Indian Ocean thermocline and helps maintain the freshwater balance between the Indian and Pacific Oceans [*Talley*, 2008]. Indeed, the low salinity water of the ITF can be traced across the Indian Ocean thermocline [*Wijffels et al.*, 2002]. The input of the ITF into the Indian Ocean increases the South Equatorial Current, helping to flush the thermocline and increases southward heat transport via the Agulhas Current [*Godfrey*, 1996; *Gordon*, 2005].

The largest ITF transport is between 70-140 m in the thermocline, but the depth and velocity of the transport vary seasonally with monsoonal winds and interannually with El Niño Southern Oscillation (ENSO) [*Sprintall et al.*, 2014]. The longest running current profile measurements have been made in the Makassar Strait because ~75% of the ITF flows through the Makassar Strait and appears to reflect the overall transport variability of the ITF [*Gordon et al.*, 2010; *Susanto et al.*, 2012]. During El Niño events and the winter monsoon the main transport of the ITF is reduced and deepens compared with the summer monsoon and the La Niña [*Gordon*, 2005; *Sprintall et al.*, 2014; *Susanto*

et al., 2012]. Generally, periods of reduced transport ITF are associated with cooler thermocline temperatures [*Ffield et al.*, 2000; *Gordon et al.*, 2003; *Susanto et al.*, 2012]. Because decreased transport is associated with lower temperatures, heat transport is also reduced during ENSO and the winter monsoon [*Gordon et al.*, 2003; *Tillinger and Gordon*, 2010]. For example, the heat transport was reduced by 0.24 PW during the 1997-1998 El Niño relative to the La Niña the year before [*Ffield et al.*, 2000].

Reduction of ITF transport is caused by increased freshwater input from the South China Sea (SCS) to the Makassar Strait [*Gordon et al.*, 2003; *Gordon et al.*, 2012; *Tozuka et al.*, 2007; *Tozuka et al.*, 2009]. The transport of freshwater into the ITF is referred to as the South China Sea throughflow (SCSTF) which is the inflow of water through the Luzon Strait to the north SCS and outflow water through the Karimata, Mindoro and Taiwan Straits (Figure 5-1) [*Qu et al.*, 2006]. When the SCSTF is strong the main ITF transport is generally reduced, deeper and cooler than when the SCSTF is weak. Models suggest that the SCSTF reduces the heat transport through the Makassar Strait by ~0.2 PW [*Tozuka et al.*, 2007].

Seasonally, the freshwater input from the SCSTF is affected by the monsoonal winds. The boreal winter monsoon (January, February, March) will be referred to as the East Asian Winter Monsoon (EAWM), and the boreal summer monsoon (July, August, September) will be referred to as the East Asian Summer Monsoon (EASM). The SCSTF is stronger during EAWM. During the EAWM the North Equatorial Current (NEC) bifuricates farther north weakening the Kuroshio Current east of Luzon which increases the flow of west Pacific water through the Luzon Strait [*Qu and Lukas*, 2003; *Qu et al.*, 2009]. Increased transport through the Luzon Strait enhances the transport through the

Sibutu Passage and Karimata Strait, thereby affecting the freshwater forcing from the SCS [*Gordon et al.*, 2012]. Additionally, during the EAWM the winds blow towards Australia and push the low salinity surface water from the SCS through the Karimata Strait decreasing the surface salinity in the southern Makassar Strait (Fig. 5-1) [*Gordon et al.*, 2003]. Both the enhanced transports through the Luzon Strait and Karimata Strait increase freshwater input into the Makassar Strait restricting the surface flow which causes the ITF transport to slow, deepen and cool [*Gordon et al.*, 2003; *Gordon et al.*, 2012]. In contrast during boreal summer, the monsoonal winds are reversed reducing the freshwater forcing on the ITF. During the EASM monsoon, the winds blow towards the SCS through the Karimata Strait reducing the freshwater input and surface salinity in the southern Makassar Strait (Figure 5-1b) which causes the ITF transport to increase and shoal [*Gordon et al.*, 2003]. Reduced transport through the Luzon Strait during boreal summer also weakens the freshwater forcing from the SCSTF augmenting the effects of the EASM winds.

On interannual time scales, the ITF transport weakens during El Niño events due to the decreased sea level pressure gradient [*Wyrtki*, 1987]. Recently, however, the reduced transport during the 2004 El Niño has been attributed to the transport of low salinity from the SCSTF into the northern Makassar Strait [*Gordon et al.*, 2012]. The available observations suggest that the decade-long variability is associated with changes in the westerlies and resembles El Niño-like changes, with weakening of the trade winds causing cooler subsurface temperatures and reduced transport through the ITF [*Sprintall et al.*, 2014]. Accordingly, modeling studies predict that on longer time scales, ITF transport will follow changes in Pacific trade winds [*Sen Gupta et al.*, 2012].

Paleoceanographic reconstructions may provide a test for model predications of future changes in the ITF. The records suggest that the ITF is sensitive to freshwater forcing also on millennial and longer time scales. Flooding of the Karimata Strait during the early Holocene due to sea level rise allowed fresh water from the SCS to reach southern Makassar Strait. This caused freshening of surface water and the ITF transport to deepen [*Linsley et al.*, 2010]. Additionally, a thermocline water temperature (TWT) reconstruction from the Holocene suggests that changes in the ITF thermocline generally follow Northern Hemisphere insolation and may be a response to the location of the Intetropical Convergence Zone (ITCZ) [*Xu et al.*, 2008].

The Common Era (CE), offers an opportunity to assess ITF response to known climate anomalies, including the Medieval Climate Anomaly (MCA), Little Ice Age (LIA) and shorter perturbations associated with solar variability through proxy reconstruction of the thermocline structure in the Makassar Strait. During the last 2000 years, sea surface (SST) and intermediate water (IWT) temperatures generally follow the Northern Hemisphere temperature anomalies, but not necessarily changes in the ITCZ location or freshwater forcing [*Oppo et al.*, 2009; *Rosenthal et al.*, 2013]. Currently, however, there is no thermocline reconstruction with sufficient resolution to study the centennial scale variability of the ITF thermocline. This paper presents reconstructed thermocline temperatures from the Makassar Strait for the last 2,000 years using Mg/Ca-based temperature estimates from the thermocline dwelling planktonic foraminifera *Neogloboquadrina dutertrei* (*N. dutertrei*) in order to examine the centennial variability of the ITF. By comparing the temperature reconstruction to precipitation records and ENSO reconstructions we infer the primary cause of the ITF variability on centennial

time scales.

5.3 Methods

The record is from gravity core BJ803 GGC34 (3˚53 S', 119˚26' E, long, 503 m water depth) and multi-core BJ803 MC31 (3˚53' S, 119˚27'E, 459 m water depth) (Figure 5-1). The age model for 34GGC and 31MC was published in Oppo et al. [2009]. Briefly, the age model for 31MC is based upon 13 ^{210}Pb measurements and 2 radiocarbon dates and the age model for 34GGC is based on 5 radiocarbon dates. A reservoir age of 475 years and the Fairbanks et al. [2005] calibration were used to convert radiocarbon age into calendar year. The multi core and gravity core do not overlap resulting in the gap in the record. The core was sampled every cm, but due to limited numbers of individuals, the foraminifera from two neighboring samples were combined such that the resolution is approximately every 20 years.

Thermocline temperature estimates were derived from Mg/Ca measurements from 355-425µm *N. dutertrei*. When there was over 200 µg of calcite the sample was split for isotope and trace metal analysis. Trace metal ratios were determined at Rutgers University, using a Thermo Finnigan Element XR sector-filed inductively couple mass spectrometer (ICP-MS). In addition to Mg/Ca ratios, several other element ratios were measured, including Al/Ca, Fe/Ca, Mn/Ca and Ti/Ca, to monitor for contamination from oxides and silicates. The long term precision of the data was based upon the replication of three in house consistency standards with Mg/Ca values (and one sigma standard deviations) of CS1: 1.44 mmol/mol (±0.01), CS2: 3.49 mmol/mol (±0.01), and CS3: 8.71 (±0.04) mol/mol. Data were eliminated if the calcium concentration was below 0.5 mM Ca, the Fe/Ca was above 1000 µmol/mol,or the Al/Ca was above 2000 µmol/mol. 19 data points out of 238 were rejected for these reasons. Data were also rejected if the

Mg/Ca value was two-sigma higher than the 10 nearest samples, which we took to indicate that the Mg/Ca value was influenced by contamination. Out of 238, 4 samples were eliminated due to their high Mg/Ca values. The Mg/Ca temperature estimates were smoothed by using a 5-point running average.

Isotope analyses were measured at Rutgers University on a Micromass (FISONS) Optima Isotope Ratio Mass Spectrometer. The samples were drift corrected if necessary using an in house standard. The standard is run against the international NBS19 [*IUPAC*, 1994] biannually. Throughout all the runs the average standard deviations values were ±0.05‰ for $\delta^{13}C$ and ±0.1‰ for $\delta^{18}O$. The $\delta^{18}O$ of calcite from *N. dutertrei* samples ($\delta^{18}O_C$) was converted to $\delta^{18}O$ of sea water ($\delta^{18}O_{SW}$) using the *N. dutertrei* equation from Farmer et al. [2007]. Due to the limited number of paired $\delta^{18}O_C$ and Mg/Ca measurements, the records were interpolated to 10 year time steps prior to calculating the $\delta^{18}O_{SW}$.

To determine the depth habitat of *N. dutertrei*, the $\delta^{18}O_C$ of core top samples were compared the estimated $\delta^{18}O_C$ of the water column. Salinity profiles from World Ocean Atlas 2009 from near the core site were converted to $\delta^{18}O_{SW}$ using the Morimoto et al. [2002] equation. From there, the $\delta^{18}O_{SW}$ were converted to $\delta^{18}O_C$ using the *N. dutertrei* equation from Farmer et al. [2007]. The core top *N. dutertrei* $\delta^{18}O_C$ where then plotted at the depth where *N. dutertrei* $\delta^{18}O_C$ value and the estimated seawater $\delta^{18}O_C$ overlap (Figure 5-2).

5.4 Results

Core top *N. dutertrei* $\delta^{18}O_C$ and Mg/Ca derived calcification temperatures from the Makassar Strait suggest a calcification depth of around 75-100 meters (Figure 5-2).

This is consistent with estimates from sediment trap samples from the eastern Indian Ocean suggesting that *N. dutertrei* lives between 60-90 m and is associated with the upwelling period [*Mohtadi et al., 2009*]. The *N. dutertrei* Mg/Ca calibration from Anand et al. [2003] has been used since it has the lowest standard error of the available calibrations. The standard error on individual temperature estimates is ±1.4˚C and is reduced to ±0.7˚C on the five-point running mean. The water temperature average at ~80 m from the SODA reanalysis model from 1958-2010 is 24.5 ± 1.2 ˚C (1-σ, SD) [*Carton and Giese*, 2008] and similarly, whereas the *N. dutertrei* core top average from the region is 24.3 ± 1.3˚C (1-σ, SD).

The downcore *N. dutertrei* temperature record varies between 20 and 24.5˚C with multidecadal to multicentennial variability (Figure 5-3), which is comparable to interannual variability at 100 m [*Ffield et al.* 2000]. Prior to 1300 CE, the TWT show multicentennial variability by as much as 3˚C, while after the TWT variability shows lower amplitude, but higher frequency changes. In the period between ~500 and 600 CE the temperature increases from 21 to 24˚C and subsequently decreases back to 21˚C by 800 CE. During the MCA, 900-1300 CE, the temperature increases from 21 to ~24˚C. After 1300 CE, TWT does not exceed 23˚C again until 1960 and the mean temperature is 1.3±0.1°C cooler than prior to 1300 CE. Between 1300 to ~1960 CE multidecadal temperature variability ranges from 21-22.5˚C and temperature oscillations last between ~60 and 130 years. After 1960 CE the temperature rapidly increases to 23˚C. Although not continuous due to limited sample size, generally the $\delta^{18}O_{SW}$ record suggests higher $\delta^{18}O_{SW}$ during periods of warmer thermocline temperatures (Figure 5-3).

5.5 Discussion

Modern observational records show that ENSO is a dominant mode of ITF variability [*Ffield et al.*, 2000; *Gordon et al.*, 2012; *Susanto et al.*, 2012]. However, to the extent that past ENSO reconstructions represent decadal to centennial ENSO modulations, these modulations do not appear to impact the ITF transport. The various reconstructions of ENSO multidecadal to centennial variability for the last 2000 years differ [*Conroy et al.*, 2008; *Emile-Geay et al.*, 2013; *Khider et al.*, 2011; *Moy et al.*, 2002; *Rein et al.*, 2004] (Figure 5-4). Nonetheless, comparison of our TWT record to several of these reconstructions suggests that ENSO modulations are not the dominant forcing on the centennial ITF variability during the Common Era. Periods of increased precipitation in South America and the Galapagos [*Conroy et al.*, 2008; *Moy et al.*, 2002], interpreted as increased intensity or frequency of El Niño events are associated with warming and increased salinity of thermocline water in our record (Fig. 5-4). This is in contrast to the current understanding of the ITF response, which indicates El Niño events would cool and freshen the thermocline [*Susanto et al.*, 2012]. Thus based on our current ENSO reconstructions and understanding of the ITF-ENSO relationship, ENSO does not appear to be driving ITF variability on centennial time scales.

Another dominant mode of ITF variability originates from seasonal changes in regional monsoonal winds [*Susanto et al.*, 2012]. Here we argue that a similar mechanism may also be driving TWTs on centennial time scales. During the MCA, TWTs are on average ~1˚C warmer than during the LIA. The cooling during the LIA is coincident with a southward migration of the ITCZ (Figure 5-4) [*Haug et al.*, 2001; *Hu et al.*, 2008; *Sachs et al.*, 2009; *Tierney et al.*, 2010; *Zhang et al.*, 2008]. Because the location of the ITCZ is inherently linked to the monsoonal winds, this suggests that changes in the

regional monsoon system drove TWTs during the MCA and LIA.

We use the seasonal ITF variability as an analogue to explain the shift in TWTs that occurred between the MCA and LIA. Seasonally, during the EASM, when the ITCZ is farther north, the freshwater forcing on the ITF is reduced. The monsoonal winds blow towards the Karimata Strait inhibiting freshwater input from the SCS from reaching the southern Makassar Strait [*Gordon et al.*, 2003] and the NEC bifuricates farther south reducing the Luzon Strait transport [*Qu and Lukas*, 2003]. Similar conditions of reduced freshwater forcing on the Makassar Strait likely occurred during the MCA, when the ITCZ was farther north, causing the warm TWTs. In contrast, during the EAWM, when the ITCZ is farther south, freshwater forcing on the ITF is enhanced because the winds blow freshwater through the Karimata Strait to the Makassar Strait and transport through the Luzon Strait is increased [*Gordon et al.*, 2003; *Tozuka et al.*, 2009]. This enhanced freshwater forcing during periods of a southerly location of the ITCZ would explain why TWTs were ~1˚C cooler throughout the LIA.

In addition to being cooler after1300 CE, TWT variability also changes from multicentennial to multidecadal and the amplitude is reduced (Figure 5-3). As argued previously, during this period the ITCZ is farther south likely changing the boundary conditions to a period of enhanced freshwater transport into the Makassar Strait. Under these conditions it seems that TWTs has higher sensitivity to precipitation changes. Between 1300-1960, a Makassar Strait precipitation record generated from the δD of leaf-wax [*Tierney et al.*, 2010] is correlated to TWTs ($r=0.4$, $p<0.02$) showing that TWTs are cool when precipitation is enhanced (Figure 5-4). TWTs also correspond to solar variability during the LIA, particularly in the peaks after the Spörer and Maunder

minimum (Figure 5-4). Small changes in total solar irradiance (TSI) affect convection patterns, including enhanced precipitation over Indonesia resulting from reduced TSI [*Gupta et al.*, 2005; *Steinke et al.*, 2014]. The already enhanced freshwater forcing on the ITF due to the southward migration of the ITCZ set the boundary conditions such that the changes in freshwater from precipitation are sufficient to drive thermocline variability. This increased sensitivity to precipitation would explain why TWT variability is different during the LIA.

The high TWTs between 500-700 CE do not appear to be associated with a robust shift in the ITCZ. Although the $\delta^{18}O$ from Wanxiang Cave (33°19'N, 105°00'E, 1200 m above sea level) indicates greater precipitation [*Zhang et al.*, 2008] other precipitation records from the region do not indicate a similar change [*Hu et al.*, 2008; *Tierney et al.*, 2010]. Therefore, this increase in TWTs is not necessarily related to migration of the ITCZ, but rather may be due to an increase in the northern branch of the EASM driven by subtropical atmosphere dynamics [*Lau et al.*, 2000]. A strong EASM north of the ITF could cause the NEC to bifuricate farther south reducing the transport through the Luzon Strait and weakening SCSTF [*Qu and Lukas*, 2003; *Qu et al.*, 2009]. Reduced freshwater forcing on the ITF from the SCS would cause TWTs to increase explaining the high TWT between 500-700 CE.

Lastly, using the TWT record generated in this study along with previously published SST [*Oppo et al.*, 2009] and IWT [*Rosenthal et al.*, 2013] records from the Makassar Strait we try to estimate the difference in transport weighted temperature and heat transport between the MCA and LIA. Although the records show distinct variability throughout the Common Era, MCA temperatures are on average warmer than the LIA at

all depths (Figure 5-5). If we assume that the transport and velocity of the ITF at the different depths in the past is comparable to the present, we can make some first order approximations of how the temperature weighted transport and heat transport varied between the MCA and LIA. Using the transport profile from Tillinger and Gordon [2010] and the average SST, TWT, and IWT temperature from 1000-1300 CE for the MCA and 1450-1850 CE for LIA we calculate that the temperature weighted transport was approximately 1˚C higher during the MCA. Similarly, using the same average temperatures for the respective time periods and depths, and using the annual velocity profile in Susanto et al. [2012], we calculate that the heat transport during the MCA was approximately 0.04 PW higher than during the LIA. If, we use the boreal summer velocity profile for the MCA and the winter velocity profile for the LIA, as we argue that the MCA was more similar to the EASM and the LIA was more similar to the EAWM, the heat transport during the MCA is ~0.1 PW higher. While this heat anomaly is not large compared with observed interannual variability, integrated over a few centuries, it potentially translates into a large perturbation. Based on this we would expect greater heat transport through the Leeuwin Current into the Indian Ocean thermocline and farther into the Agulhas Current during the MCA. This may have been one mechanism by which the Common Era climate anomalies were propagated across the equator into the southern hemisphere.

5.6 References

Anand, P., et al. (2003), Calibration of Mg/Ca thermometry in planktonic foraminifera from a sediment trap time series, *Paleoceanography*, *18*(2).

Carton, J. A., and B. S. Giese (2008), A reanalysis of ocean climate using Simple Ocean Data Assimilation (SODA), *Monthly Weather Review*, *136*(8), 2999-3017.

Conroy, J. L., et al. (2008), Holocene changes in eastern tropical Pacific climate inferred from a Galapagos lake sediment record, *Quaternary Science Reviews*, *27*(11), 1166-1180.

Emile-Geay, J., et al. (2013), Estimating Central Equatorial Pacific SST Variability over the Past Millennium. Part I: Methodology and Validation, *Journal of Climate*, *26*(7), 2302-2328.
Fairbanks, R. G., et al. (2005), Radiocarbon calibration curve spanning 0 to 50,000 years BP based on paired 230Th/234U/238U and 14C dates on pristine corals, *Quaternary Science Reviews*, *24*(16-17), 1781-1796.
Farmer, E. C., et al. (2007), Corroborating ecological depth preferences of planktonic foraminifera in the tropical Atlantic with the stable oxygen isotope ratios of core top specimens, *Paleoceanography*, *22*(3).
Ffield, A., et al. (2000), Temperature variability within Makassar Strait, *Geophysical Research Letters*, *27*(2), 237-240.
Gordon, A. L., et al. (2003), Cool Indonesian throughflow as a consequence of restricted surface layer flow, *Nature*, *425*(6960), 824-828.
Gordon, A. L. (2005), Oceanography of the Indonesian seas and their throughflow, *Oceanography*, *18*(4), 14-27.
Gordon, A. L., et al. (2010), The Indonesian throughflow during 2004-2006 as observed by the INSTANT program, *Dynamics of Atmospheres and Oceans*, *50*(2), 115-128.
Gordon, A. L., et al. (2012), South China Sea throughflow impact on the Indonesian throughflow, *Geophysical Research Letters*, *39*.
Gupta, A. K., et al. (2005), Solar influence on the Indian summer monsoon during the Holocene, *Geophysical Research Letters*, *32*(17), L17703.
Haug, G. H., et al. (2001), Southward Migration of the Intertropical Convergence Zone Through the Holocene, *Science*, *293*(5533), 1304-1308.
Hu, C. Y., et al. (2008), Quantification of Holocene Asian monsoon rainfall from spatially separated cave records, *Earth and Planetary Science Letters*, *266*(3-4), 221-232.
IUPAC (1994), Commission on Atomic Weights and Isotopic Abundances, *Pure and Applied Chemistry*, *66*, 2423-2444.
Khider, D., et al. (2011), Assessing El Nino Southern Oscillation variability during the past millennium, *Paleoceanography*, *26*.
Lau, K. M., et al. (2000), Dynamical and Boundary Forcing Characteristics of Regional Components of the Asian Summer Monsoon, *Journal of Climate*, *13*(14), 2461-2482.
Linsley, B. K., et al. (2010), Holocene evolution of the Indonesian throughflow and the western Pacific warm pool, *Nature Geosci*, *3*(8), 578-583.
Mohtadi, M., et al. (2009), Low-latitude control on seasonal and interannual changes in planktonic foraminiferal flux and shell geochemistry off south Java: A sediment trap study, *Paleoceanography*, *24*(1), PA1201.
Morimoto, M., et al. (2002), Salinity records for the 1997-98 El Nino from Western Pacific corals, *Geophysical Research Letters*, *29*(11).
Moy, C. M., et al. (2002), Variability of El Nino/Southern Oscillation activity at millennial timescales during the Holocene epoch, *Nature*, *420*(6912), 162-165.
Oppo, D. W., et al. (2009), 2,000-year-long temperature and hydrology reconstructions from the Indo-Pacific warm pool, *Nature*, *460*(7259), 1113-1116.
Qu, T. D., and R. Lukas (2003), The bifurcation of the North Equatorial Current in the Pacific, *Journal of Physical Oceanography*, *33*(1), 5-18.
Qu, T. D., et al. (2009), An introduction to the South China Sea throughflow: Its dynamics, variability, and application for climate, *Dynamics of Atmospheres and Oceans*, *47*(1-3), 3-14.
Regenberg, M., et al. (2009), Calibrating Mg/Ca ratios of multiple planktonic foraminiferal species with δ18O-calcification temperatures: Paleothermometry for the upper water column, *Earth and Planetary Science Letters*, *278*(3-4), 324-336.
Rein, B., et al. (2004), A major Holocene ENSO anomaly during the Medieval period, *Geophys. Res. Lett.*, *31*(17), L17211.

Rosenthal, Y., et al. (2013), Pacific Ocean Heat Content During the Past 10,000 Years, *Science*, *342*(6158), 617-621.

Sachs, J. P., et al. (2009), Southward movement of the Pacific intertropical convergence zone AD 1400-1850, *Nature Geosci*, *2*(7), 519-525.

Schlitzer, R. (2011), Ocean Data View, edited.

Sen Gupta, A., et al. (2012), Drivers of the projected changes to the Pacific Ocean equatorial circulation, *Geophysical Research Letters*, *39*.

Sprintall, J., et al. (2014), The Indonesian seas and their role in the coupled ocean-climate system, *Nature Geoscience*, *7*, 487-492.

Steinke, S., et al. (2014), Mid to Late-Holocene Australian-Indonesian summer monsoon variability, *Quaternary Science Reviews*, *93*(0), 142-154.

Susanto, R. D., et al. (2012), Variability of Indonesian throughflow within Makassar Strait, 2004-2009, *Journal of Geophysical Research-Oceans*, *117*.

Tierney, J. E., et al. (2010), Coordinated hydrological regimes in the Indo-Pacific region during the past two millennia, *Paleoceanography*, *25*(1), PA1102.

Tillinger, D., and A. Gordon (2010), Transport weighted temperature and internal energy transport of the Indonesian throughflow, *Dynamics of Atmospheres and Oceans*, *50*(2), 224-232.

Tozuka, T., et al. (2007), Dramatic impact of the South China Sea on the Indonesian Throughflow, *Geophysical Research Letters*, *34*(12).

Tozuka, T., et al. (2009), Impacts of the South China Sea Throughflow on seasonal and interannual variations of the Indonesian Throughflow, *Dynamics of Atmospheres and Oceans*, *47*(1-3), 73-85.

Wyrtki, K. (1987), Indonesian through flow and the associated pressure gradient, *Journal of Geophysical Research: Oceans*, *92*(C12), 12941-12946.

Xu, J., et al. (2008), Changes in the thermocline structure of the Indonesian outflow during Terminations I and II, *Earth and Planetary Science Letters*, *273*(1-2), 152–162.

Zhang, P. Z., et al. (2008), A Test of Climate, Sun, and Culture Relationships from an 1810-Year Chinese Cave Record, *Science*, *322*(5903), 940-942.

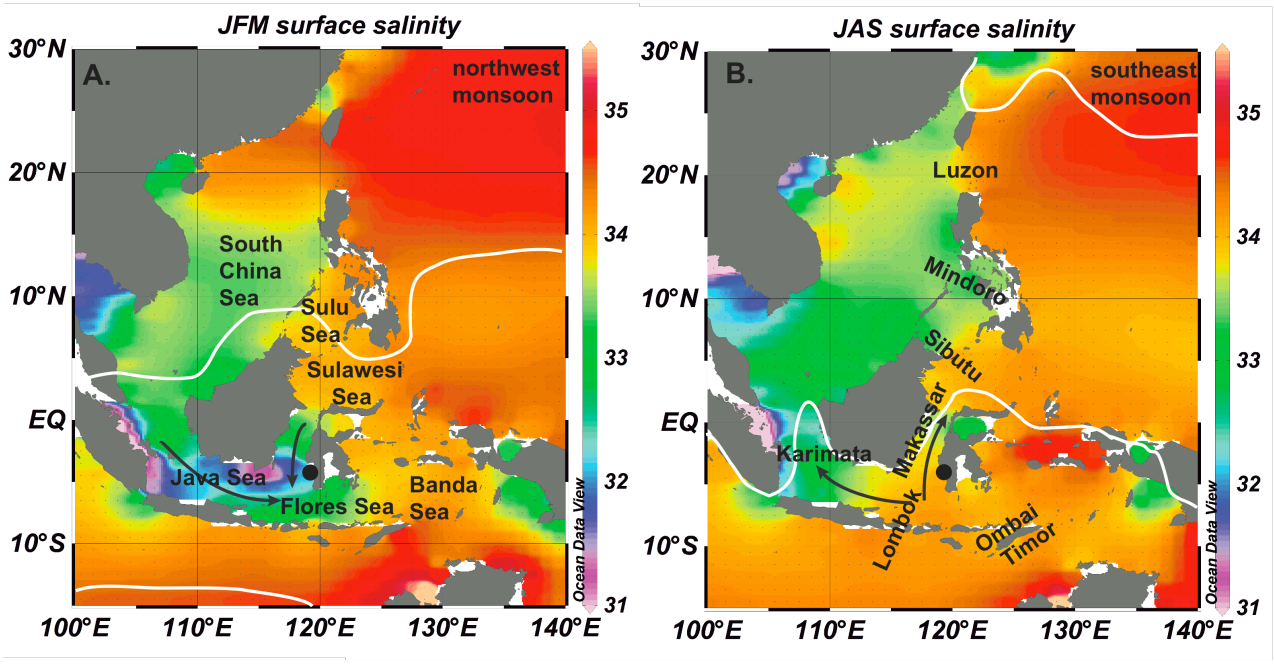

Figure 5-1. (A) Winter (January, February, March) surface salinity for SCS and ITF region with the marginal seas labeled. The dark grey arrows indicate the wind direction. The region between the white lines indicates the area of enhance precipitation during the winter season. The southern limit in the east is south 15˚S and extends off the map. The black dot marks the core location. (B) Same as A except for the summer (July, August, September) and the straits and passages are labeled. The northern precipitation line extends off the map in the west [*Schlitzer*, 2011]

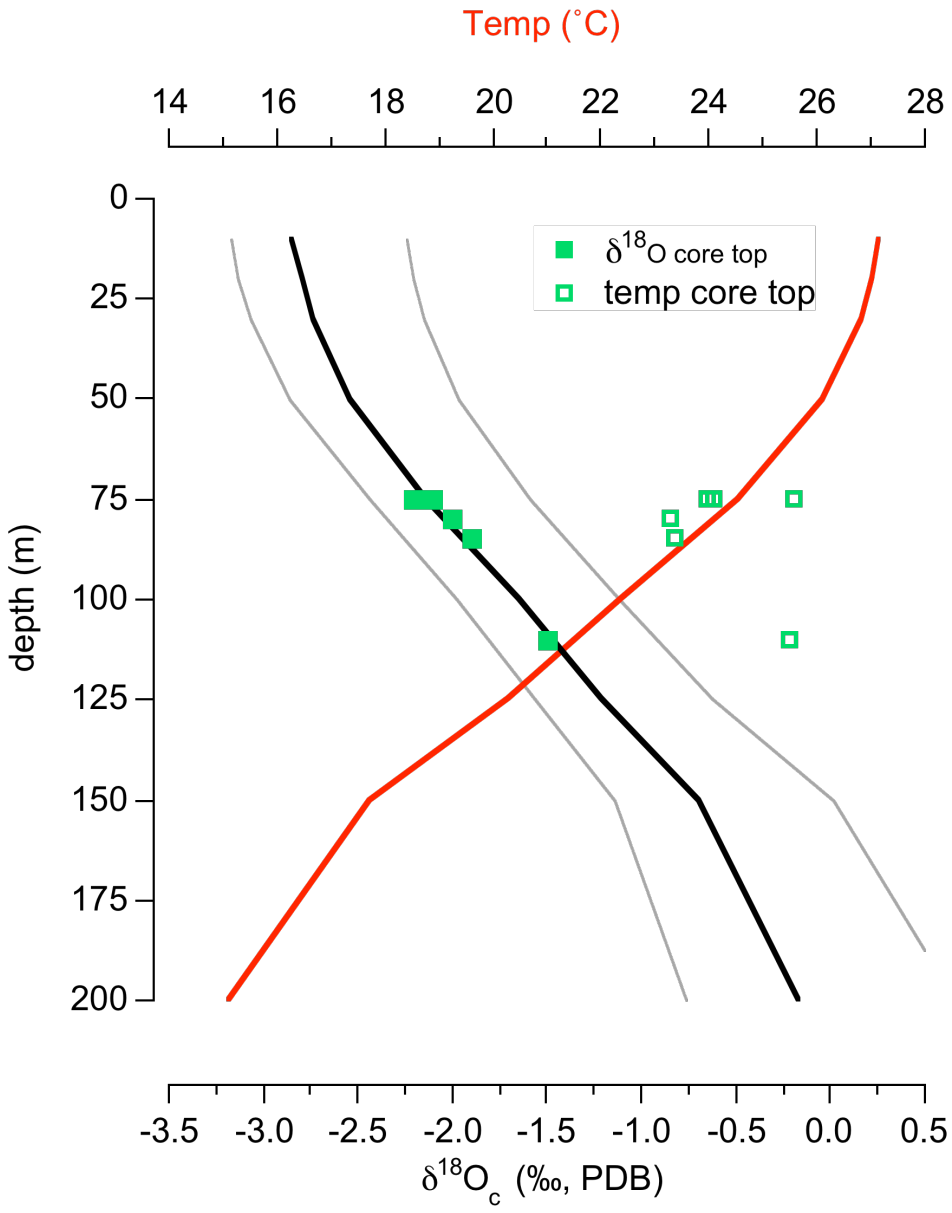

Figure 5-2. Measured $\delta^{18}O_C$ from *N. dutertrei* from the ITF (solid green squares) are plotted on the estimated $\delta^{18}O_C$ of sea water (black line) from near the core site. The thin grey lines are the upper and lower $\delta^{18}O_C$ values calculate from the different published $\delta^{18}O_{SW}$,$\delta^{18}O_C$, temperature relationships [see *Regenberg et al.*, 2009]. Measured Mg/Ca *N. dutertrei* temperatures estimates from core tops (open green squares) are plotted on WOA temperature profile from -1.5 ˚S, 117.5 ˚E. The Anand et al. [2003] *N. dutertrei* calibration was used to convert Mg/Ca to temperature

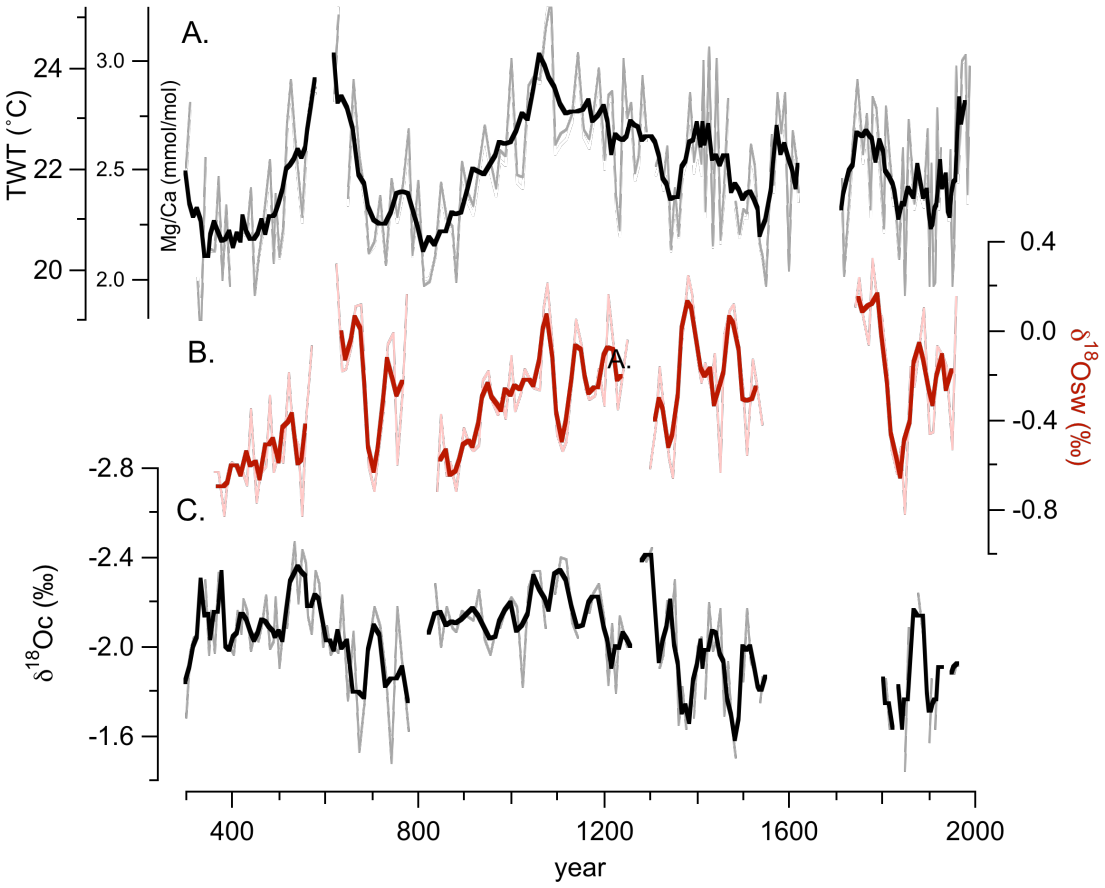

Figure 5-3. (A) The individual (grey) and 5-point average (black) downcore *N. dutertrei* Mg/Ca temperature estimates (B) The interpolated individual (pink) and 3-point running average of the $\delta^{18}O_{SW}$ values (red). More positive $\delta^{18}O_{SW}$ values are associated with increased salinity (C) The individual (grey) and 3-point average (black) $\delta^{18}O_C$ of *N. dutertrei.* More negative numbers are associated with warmer temperatures and fresher water

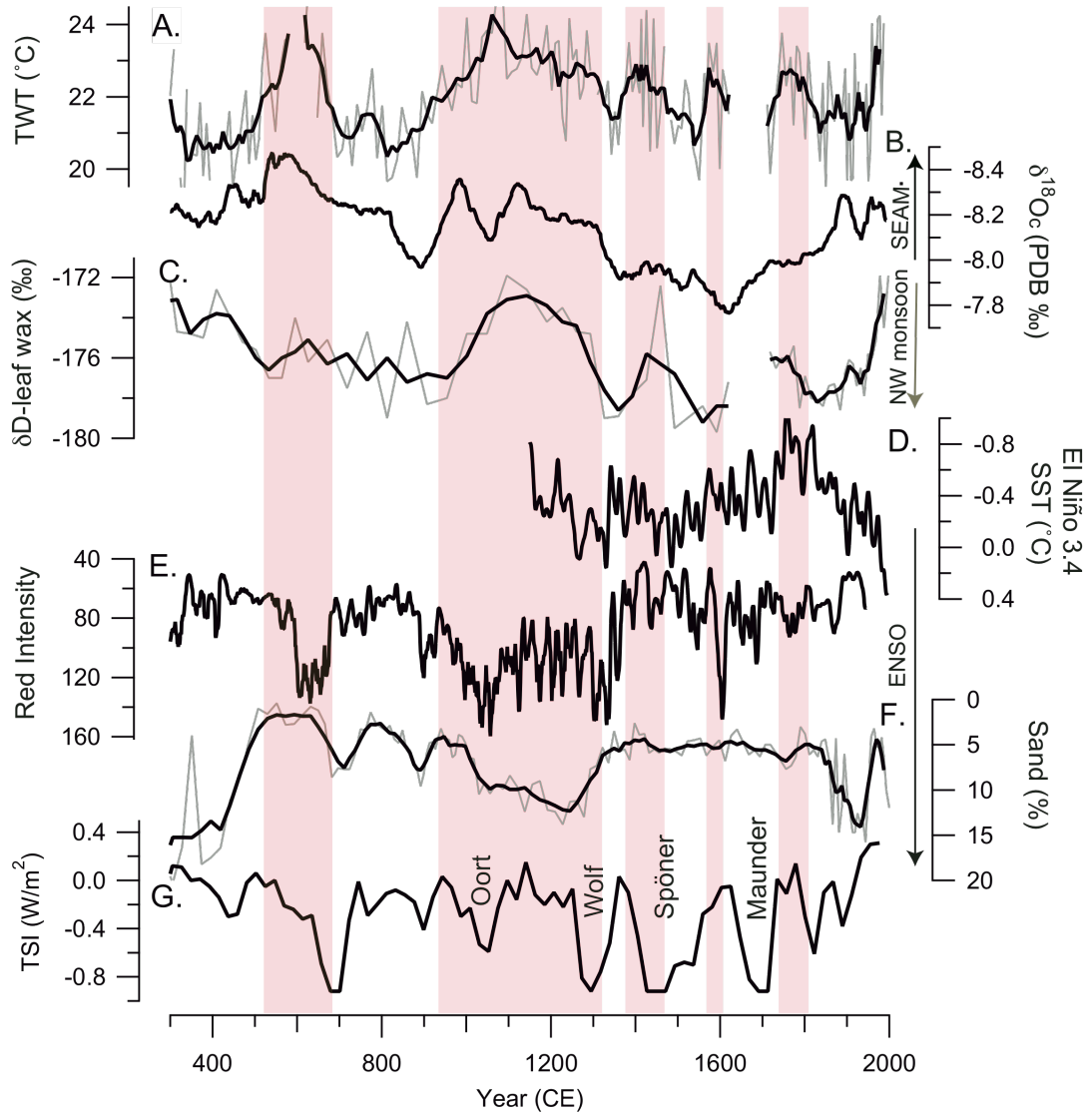

Figure 5-4. Monsoonal precipitation reconstructions (B, C), ENSO reconstructions (D,E,F) and total solar irradiance (G) are plotted for comparison with the TWT reconstruction (A). The decrease in NW monsoon and increase SEASM precipitation are associated with increased TWT, whereas reduced ENSO variability is not. All proxies are plotted such that values towards the top of the page should be associated with increased TWT. (B) Wanxiang Cave (33°19'N, 105°00'E) [*Zhang et al.*, 2008] (C) Makassar Strait (3˚53'S, 119˚27'E) [*Tierney et al.*, 2010] (D) Proxy compilation of El Niño 3.4 SST [*Emile-Geay et al.*, 2013] (E) A ENSO record based on precipitation from the Peruvian Andes [*Moy et al.*, 2002] (F) ENSO record based on precipitation from the Galapagos [*Conroy et al.*, 2008] (G) TSI reconstruction [*Steinhilber et al.*, 2012]

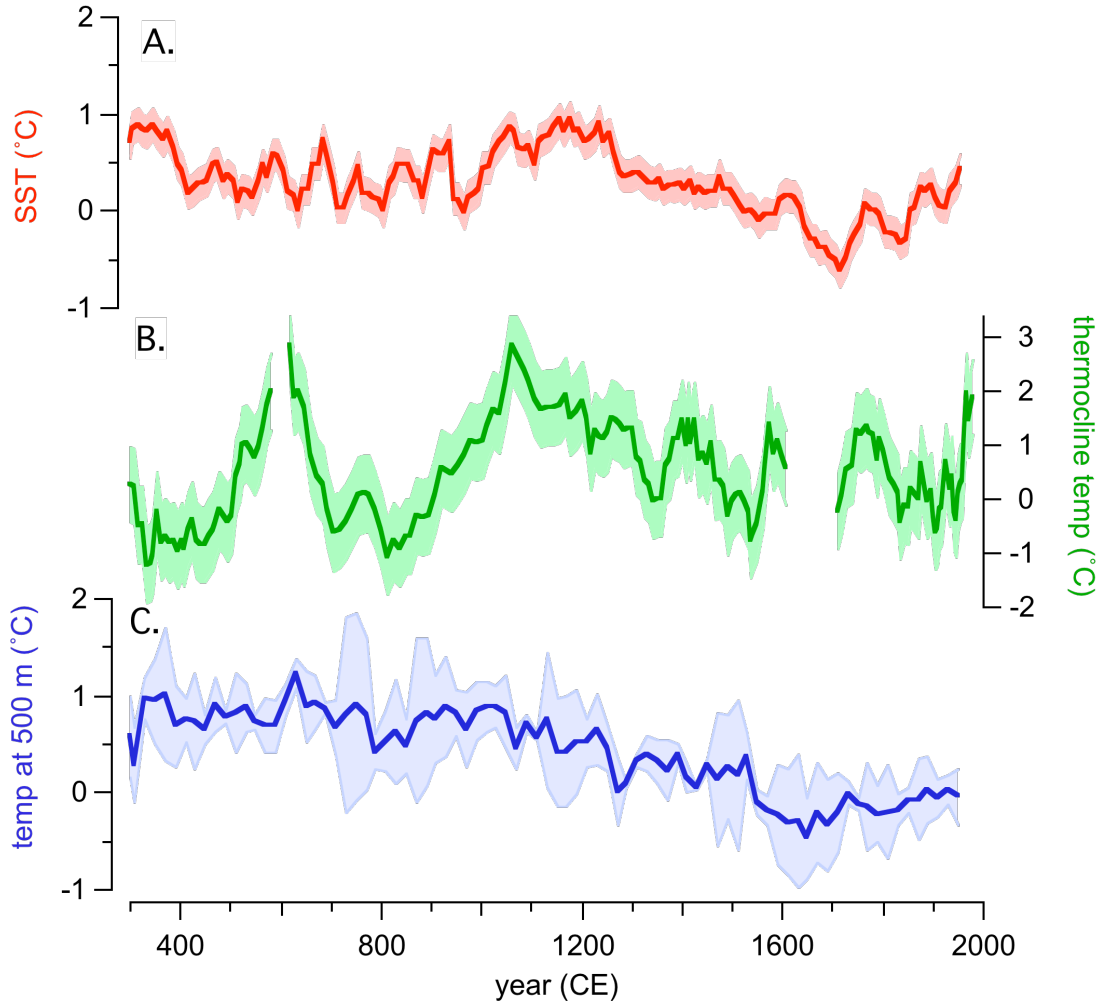

Figure 5-5. Makassar Strait temperature anomalies from throughout the water column. (A) SST temperature estimates from *G. ruber* Mg/Ca temperature [*Oppo et al.*, 2009]. (B) TWT estimates from *N. dutertrei* Mg/Ca temperature estimates (this study). (C) Intermediate water temperature (~500 m) estimates from *H. balthica* [*Rosenthal et al.*, 2013]. The shaded regions represent the positive and negative standard error. All anomalies are calculated from the average between 1850-1880 CE. Note the different temperature scales

Appendix 3

Appendix 3.1 Error analysis on the N. dutertrei temperature

The Anand et al. [2003] *N. dutertrei* calibration is Mg/Ca = (0.34±0.02) exp(T*(0.09±0.003)) with an error of ±1.2˚C. The four core top measurements have a standard error of ±0.4˚C. Combining these two errors, the *N. dutertrei* temperature record has an error of ±1.3˚C (eq 1). The error of the temperature anomaly is reduced because it only relies on the slope in the calibration equation, (0.09±0.003) which produces an error of ±1.0˚C resulting in an absolute temp anomaly error of ±1.1˚C (eq 2). The binned data averages three data points further reducing the error to ±0.8˚C (eq 3). This same approach was used to estimate the error in the temperature records from *Uvigerina* and *N. dutertrei* from the Indonesian Throughflow.

Eq. 1: *absolute temp error:* $[(1.2)^2 + (0.4)^2]^{1/2} = \pm 1.3$ °C

Eq. 2: *absolute temp anomaly error:* $[(1.0)^2 + (0.4)^2]^{1/2} = \pm 1.1$ °C

Eq. 3: *smoothed absolute temp anomaly error*: $1.0\ °C / (3-1)^{1/2} = \pm 0.8$ °C

Appendix 3.2. All the N. dutertrei data from Chapter 3.

depth in sediment (cm)	Age (year BP)	Mg/Ca (mmol/mol)	Fe/Ca (μmol/mol)	Al/Ca (μmol/mol)	Temp (˚C)	Temp anomaly (˚C)	δ13C (per mil, PDB)	δ18O (per mil, PDB)	sea level (m)	δ18O Sea level corrected	δ18Osw (per mil, SMOW)
0.75	1092	1.31	29	52	13.73	-0.08	1.43	0.46	-3.43	1.42	0.01
8.75	1172	1.21	18	105	12.90	-0.91	1.30	0.66	-3.47	1.28	-0.12
16.75	1252	1.18	55	32	12.59	-1.22	1.27	0.60	-3.51	1.25	0.05
24.75	1332	1.26	69	27	13.31	-0.50	1.34	0.60	-3.54	1.32	-0.04
32.75	1412	1.30	94	48	13.68	-0.13	1.27	0.42	-3.56	1.25	0.03
40.75	1492	1.28	101	11	13.53	-0.28	1.34	0.53	-3.58	1.32	-0.36
48.75	1603	1.13	35	70	12.11	-1.70	1.33	0.46	-3.60	1.31	-0.14
56.75	1720	1.25	135	10	13.25	-0.56	1.33	0.42	-3.61	1.31	-0.03
64.75	1836	1.30	98	37	13.68	-0.13	1.35	0.44	-3.62	1.33	0.00
72.75	1952	1.22	95	21	12.94	-0.87	1.15	0.64	-3.62	1.14	-0.39
80.75	2069	1.17	67	20	12.52	-1.29	1.41	0.34	-3.62	1.39	-0.28
88.75	2185	1.22	68	25	12.93	-0.88	1.32	0.35	-3.62	1.30	-0.23
96.75	2302	1.27	205	225	13.37	-0.44	1.49	0.30	-3.62	1.47	0.22
104.75	2418	1.37	59	22	14.23	0.42	1.12	0.56	-3.62	1.10	0.02
112.75	2535	1.35	121	19	14.11	0.30	1.34	0.39	-3.63	1.32	-0.01
120.75	2640	1.23	119	36	13.07	-0.74	1.31	0.60	-3.64	0.56	-0.01
128.75	2726	1.41	134	9	14.53	0.73	1.36	0.51	-3.65	0.47	0.24
136.75	2812	1.28	139	19	13.49	-0.32	1.29	0.73	-3.66	0.69	0.22
144.75	2898	1.19	101	59	12.67	-1.14	1.26	0.50	-3.68	0.46	-0.19
152.75	2983	1.18	100	38	12.57	-1.24	1.18	0.51	-3.70	0.47	-0.21
160.75	3066	1.14	54	18	12.19	-1.62	1.26	0.47	-3.73	0.43	-0.34
168.75	3121	1.30	121	33	13.70	-0.11	1.23	0.71	-3.75	0.67	0.25
176.75	3175	1.37	187	244	14.26	0.45	1.46	0.68	-3.77	0.64	0.35
182.75	3216	1.35	59	52	14.11	0.30	1.35	0.60	-3.79	0.56	0.23
190.75	3270	1.19	271	45	12.67	-1.14	1.29	0.67	-3.82	0.63	-0.02
198.75	3325	1.29	218	24	13.55	-0.26	1.36	0.47	-3.85	0.43	-0.02
206.75	3379	1.41	162	64	14.54	0.73	1.40	0.51	-3.88	0.47	0.24
214.75	3434	1.36	227	29	14.14	0.33	1.44	0.51	-3.92	0.47	0.15

Appendix 3.2 continued

depth in sediment (cm)	Age (year BP)	Mg/Ca (mmol/mol)	Fe/Ca (μmol/mol)	Al/Ca (μmol/mol)	Temp (˚C)	Temp anomaly (˚C)	δ13C (per mil, PDB)	δ18O (per mil, PDB)	sea level (m)	δ18O Sea level corrected	δ18Osw (per mil, SMOW)
222.75	3488	1.42	100	16	14.66	0.85	1.35	0.54	-3.95	0.50	0.30
230.75	3543	1.48	171	28	15.13	1.32	1.43	0.48	-4.00	0.44	0.35
238.75	3597	1.46	59	14	14.93	1.12	1.41	0.48	-4.04	0.44	0.30
246.75	3651	1.34	106	47	14.03	0.22	1.37	0.38	-4.09	0.34	0.00
254.75	3706	1.11	160	34	11.86	-1.95	1.39	0.39	-4.14	0.35	-0.49
262.75	3764	1.17	102	42	12.48	-1.33	1.53	0.66	-4.20	0.62	-0.08
270.75	3831	1.12	106	23	12.05	-1.76	1.37	0.63	-4.27	0.58	-0.21
278.75	3899	1.18	111	239	12.60	-1.21	1.37	0.49	-4.34	0.45	-0.22
286.75	3966	1.25	96	22	13.20	-0.61			-4.43		
294.75	4034	1.10	87	38	11.79	-2.01	1.39	0.59	-4.52	0.54	-0.31
302.75	4101	1.27	175	36	13.42	-0.39	1.33	0.47	-4.61	0.43	-0.05
310.75	4169	1.27	170	2	13.44	-0.37			-4.71		
318.75	4236	1.35	295	10	14.09	0.28			-4.82		
326.75	4304	1.25	140	83	13.23	-0.58	1.49	0.51	-4.93	0.47	-0.05
333.75	4363	1.39	337	127	14.40	0.59	1.42	0.43	-5.04	0.38	0.13
341.75	4430	1.15	262	25	12.27	-1.54	1.47	0.73	-5.16	0.68	-0.06
349.75	4498	1.24	128	72	13.18	-0.63	1.40	0.44	-5.29	0.39	-0.14
357.75	4555	1.27	213	58	13.36	-0.45	1.46	0.87	-5.41	0.82	0.33
365.75	4612	1.15	167	17	12.29	-1.52	1.23	0.47	-5.53	0.42	-0.31
373.75	4668	1.39	157	36	14.38	0.57	1.34	0.60	-5.66	0.54	0.29
381.75	4724	1.11	303	21	11.94	-1.87	1.23	0.58	-5.79	0.52	-0.29
389.75	4781	1.24	254	33	13.14	-0.67	1.44	0.71	-5.92	0.65	0.12
397.75	4837	1.25	242	22	13.23	-0.58	1.36	0.37	-6.06	0.31	-0.20
405.75	4918	1.37	462	37	14.28	0.47	1.44	0.73	-6.27	0.67	0.41
413.75	5009	1.53	310	87	15.46	1.65	1.49	0.51	-6.52	0.44	0.45
421.75	5100	1.38	231	39	14.33	0.52	1.50	0.53	-6.78	0.46	0.21
429.75	5191	1.27	92	168	13.40	-0.40	1.52	0.51	-7.06	0.44	-0.01
437.75	5282	1.47	232	118	15.06	1.25	1.36	0.54	-7.35	0.47	0.39
445.75	5373	1.30	508	101	13.64	-0.17	1.47	0.71	-7.65	0.63	0.23
453.75	5463	1.32	409	41	13.82	0.01	1.42	0.55	-7.97	0.47	0.12

Appendix 3.2 continued

depth in sediment (cm)	Age (year BP)	Mg/Ca (mmol/mol)	Fe/Ca (μmol/mol)	Al/Ca (μmol/mol)	Temp (˚C)	Temp anomaly (˚C)	δ13C (per mil, PDB)	δ18O (per mil, PDB)	sea level (m)	δ18O Sea level corrected	δ18Osw (per mil, SMOW)
461.75	5553	1.19	210	66	12.72	-1.09			-8.30		
469.75	5638	1.33	564	29	13.89	0.08	1.45	0.67	-8.62	0.58	0.25
477.75	5723	1.30	510	61	13.70	-0.10			-8.95		
485.75	5807	1.44	61	93	14.79	0.98	1.51	0.78	-9.30	0.68	0.56
493.75	5892	1.17	79	69	12.53	-1.28	1.34	0.64	-9.66	0.54	-0.09
501.75	5977	1.19	42	33	12.65	-1.16	1.36	0.81	-10.04	0.71	0.11
509.75	6066	1.45	110	57	14.85	1.04	NaN	NaN	-10.44		
517.75	6154	1.37	51	42	14.27	0.47	1.46	0.78	-10.86	0.67	0.45
525.75	6242	1.27	120	76	13.37	-0.44	1.29	0.68	-11.29	0.57	0.14
533.75	6331	1.23	38	30	13.05	-0.76	1.36	0.54	-11.74	0.42	-0.07
542.75	6430	1.37	37	18	14.22	0.41	1.26	0.75	-12.26	0.63	0.41
550.75	6515	1.17	60	33	12.47	-1.34	1.36	0.81	-12.72	0.68	0.07
558.75	6569	1.20	114	19	12.78	-1.03	1.42	0.76	-13.01	0.63	0.09
566.75	6623	1.21	46	20	12.89	-0.92	NaN	NaN	-13.32		
574.75	6677	1.26	97	61	13.35	-0.46	1.39	0.82	-13.62	0.69	0.28
582.75	6731	1.18	47	78	12.63	-1.17	1.39	0.67	-13.94	0.53	-0.04
590.75	6785	1.17	84	34	12.49	-1.32	1.22	0.54	-14.26	0.39	-0.20
598.75	6839	1.30	71	22	13.64	-0.17	1.49	0.74	-14.58	0.59	0.26
606.75	6900	1.31	35	10	13.76	-0.05	1.36	0.76	-14.96	0.61	0.32
614.75	6964	1.24	92	70	13.10	-0.71	NaN	NaN	-15.35		
622.75	7027	1.37	79	19	14.26	0.45	1.32	0.59	-15.75	0.43	0.26
630.75	7090	1.30	65	21	13.68	-0.13	1.35	0.88	-16.16	0.72	0.42
638.75	7154	1.26	91	45	13.35	-0.46	1.28	0.66	-16.58	0.50	0.12
646.75	7217	1.27	64	9	13.37	-0.44	1.30	0.68	-17.00	0.51	0.14
654.75	7280	1.13	109	19	12.15	-1.66	NaN	NaN	-17.43		
662.75	7344	1.23	111	56	13.06	-0.75	1.36	0.71	-17.87	0.53	0.10
670.75	7407	1.19	153	94	12.73	-1.08	1.33	0.80	-18.31	0.62	0.12
678.75	7471	1.38	134	36	14.30	0.49	1.36	0.85	-18.76	0.67	0.53
686.75	7534	1.30	129	43	13.69	-0.12	1.37	0.83	-19.22	0.64	0.37
688.75	7550	1.26	60	36	13.32	-0.49	1.37	0.72	-19.34	0.53	0.18

Appendix 3.2 continued

depth in sediment (cm)	Age (year BP)	Mg/Ca (mmol/mol)	Fe/Ca (μmol/mol)	Al/Ca (μmol/mol)	Temp (˚C)	Temp anomaly (˚C)	δ13C (per mil, PDB)	δ18O (per mil, PDB)	sea level (m)	δ18O Sea level corrected	δ18Osw (per mil, SMOW)
696.75	7613	1.36	57	25	14.18	0.37	1.26	0.75	-19.80	0.55	0.40
704.75	7677	1.13	39	34	12.16	-1.65	1.31	0.71	-20.28	0.50	-0.11
712.75	7740	1.13	72	28	12.10	-1.71	1.29	0.82	-20.76	0.61	-0.01
720.75	7804	1.27	266	43	13.44	-0.37	1.38	0.74	-21.25	0.53	0.22
728.75	7867	1.20	180	43	12.80	-1.01	1.36	0.68	-21.74	0.46	0.01
736.75	7930	1.21	237	72	12.89	-0.92	1.43	0.88	-22.24	0.66	0.23
747.75	8017	1.50	421	30	15.22	1.41	1.34	0.63	-22.94	0.40	0.52
752.75	8057	1.26	109	17	13.32	-0.49	1.26	0.96	-23.26	0.73	0.41
760.75	8121	1.16	140	26	12.40	-1.40	1.25	0.83	-23.79	0.59	0.07
768.75	8184	1.32	80	185	13.83	0.03	1.14	0.83	-24.31	0.59	0.40
776.75	8247	1.42	121	55	14.66	0.85	1.24	0.99	-24.85	0.74	0.75
784.75	8323	1.33	141	100	13.92	0.12	1.22	0.92	-25.50	0.66	0.51
792.75	8414	1.39	298	100	14.37	0.56	1.15	1.00	-26.28	0.74	0.69
800.75	8504	1.31	251	26	13.76	-0.05	1.25	0.94	-27.07	0.67	0.49
808.75	8594	1.33	430	98	13.92	0.11	1.17	0.74	-27.88	0.46	0.33
816.75	8684	1.42	263	30	14.68	0.87	1.23	0.88	-28.70	0.59	0.64
824.75	8774	1.36	467	54	14.18	0.37	1.33	0.92	-29.53	0.63	0.57
832.75	8865	1.37	739	86	14.26	0.45	1.18	1.05	-30.37	0.74	0.71
847.75	9034	1.48	277	17	15.11	1.30	1.18	1.09	-31.98	0.77	0.95
855.75	9084	1.40	309	20	14.50	0.69	1.26	1.10	-32.47	0.77	0.82
863.75	9117	1.56	544	686	15.66	1.85	1.15	0.76	-32.79	0.43	0.75
871.75	9150	1.42	299	37	14.64	0.84	1.14	0.87	-33.11	0.54	0.63
879.75	9183	1.55	210	36	15.64	1.83	1.22	0.88	-33.43	0.55	0.86
959.75	9509	1.42	440	78	14.68	0.87	1.12	0.83	-36.71	0.47	0.60
967.75	9542	1.44	676	101	14.79	0.98	1.09	0.95	-37.05	0.58	0.74
975.75	9575	1.41	342	29	14.54	0.73	1.06	0.84	-37.38	0.47	0.57
983.75	9608	1.52	423	26	15.37	1.56	1.06	0.69	-37.72	0.31	0.61
991.75	9640	1.64	346	61	16.28	2.47	1.08	0.80	-38.06	0.42	0.93
999.75	9673	1.67	418	561	16.42	2.61	1.04	1.01	-38.40	0.63	1.18
1007.75	9748	1.61	403	37	16.01	2.20	1.05	0.83	-39.19	0.44	0.89

Appendix 3.2 continued

depth in sediment (cm)	Age (year BP)	Mg/Ca (mmol/mol)	Fe/Ca (μmol/mol)	Al/Ca (μmol/mol)	Temp (˚C)	Temp anomaly (˚C)	δ13C (per mil, PDB)	δ18O (per mil, PDB)	sea level (m)	δ18O Sea level corrected	δ18Osw (per mil, SMOW)
1015.75	9826	1.90	369	45	17.90		1.29	1.11	-40.01	0.71	
1023.75	9904	1.53	316	27	15.45	1.64	1.07	0.70	-40.84	0.29	0.64
1031.75	9982	1.45	701	46	14.90	1.10	1.01	0.83	-41.68	0.42	0.65
1039.75	10060	1.62	306	40	16.09	2.28	1.10	0.92	-42.52	0.49	1.00
1047.75	10138	1.58	362	27	15.86	2.05	1.10	0.84	-43.37	0.40	0.87
1055.75	10216	1.69	613	53	16.60	2.79	0.98	0.81	-44.23	0.36	1.01
1063.75	10294	1.55	704	26	15.60	1.79	0.98	0.79	-45.09	0.34	0.77
1071.75	10372	1.62	797	45	16.14	2.34	1.11	0.65	-45.95	0.19	0.75
1079.75	10450	1.76	782	183	17.04	3.23	1.00	1.00	-46.82	0.53	1.30
1087.75	10529	1.73	915	66	16.86	3.05	0.97	0.75	-47.70	0.27	1.01
1095.75	10607	1.52	1295	47	15.42	1.61	0.90	0.90	-48.58	0.42	0.84

Appendix 3.3 All the *Uvigerina* data from chapter 3.The yellow shading indicates samples that were removed because the value was greater than 2s higher than all other values and the red shading indicates samples that were small (Ca concentration below 0.4 mol). Blanks indicates depths where there was not sufficient sample to acquire data.

depth in sediment (cm)	Age (year BP)	Mg/Ca (mmol/mol)	Fe/Ca (µmol/mol)	Al/Ca (µmol/mol)	Temp (˚C)	sea level (m)	Temp SL corrected (˚C)	Temp anomaly (˚C)	δ13C (per mil, PDB)	δ18O (per mil, PDB)	δ18O Sea level corrected
0.75	1092	1.046	13	59	9.36	-3.43	9.30	-0.62	0.07	1.98	1.95
8.75	1172	1.088	25	71	9.86	-3.47	9.80	-0.12	0.15	1.96	1.93
16.75	1252	1.040	24	48	9.28	-3.51	9.22	-0.70	0.07	2.00	1.97
24.75	1332	1.270	32	57	12.02	-3.54	11.97	2.05	-0.01	2.02	1.99
32.75	1412	1.057	37	57	9.48	-3.56	9.43	-0.49	0.31	2.03	2.00
40.75	1492	1.144	25	52	10.53	-3.58	10.47	0.55	0.12	1.93	1.89
48.75	1603	1.195	71	220	11.13	-3.60	11.07	1.15	0.02	1.78	1.75
56.75	1720	1.283	121	3622	12.18	-3.61	12.12	2.20			
64.75	1836	1.239	17	33	11.66	-3.62	11.60	1.68	-0.11	1.75	1.72
72.75	1952	1.077	24	70	9.73	-3.62	9.67	-0.25	0.05	1.75	1.71
80.75	2069	1.047	57	448	9.37	-3.62	9.31	-0.61	0.20	1.84	1.80
88.75	2185	1.070	213	111	9.64	-3.62	9.59	-0.33	0.25	1.86	1.83
96.75	2302					-3.62			0.04	2.08	2.04
104.75	2418	1.184	125	177	11.00	-3.62	10.94	1.02	0.18	1.88	1.84
112.75	2535	1.263	26	30	11.94	-3.63	11.88	1.96	0.27	2.09	2.05
120.75	2640					-3.64			0.16	2.06	2.02
136.75	2812					-3.66			0.29	2.12	2.08
144.75	2898	1.119	55	20	10.23	-3.68	10.17	0.25	0.12	1.99	1.95
152.75	2983	1.151	24	31	10.60	-3.70	10.54	0.62	0.10	1.92	1.88
160.75	3066	1.135	83	35	10.42	-3.73	10.36	0.44	0.09	2.01	1.97
168.75	3121	1.095	28	57	9.95	-3.75	9.89	-0.03	0.19	1.84	1.80
176.75	3175	1.251	29	21	11.79	-3.77	11.73	1.81	0.15	1.99	1.95
182.75	3216	1.207	14	73	11.27	-3.79	11.21	1.29	0.12	1.81	1.77
190.75	3270	1.093	18	28	9.91	-3.82	9.85	-0.07	0.08	1.84	1.81
198.75	3325					-3.85			0.19	1.92	1.88

Appendix 3.3 continued

depth in	Age	Mg/Ca	Fe/Ca	Al/Ca	Temp	sea	Temp SL	Temp	δ13C (per	δ18O (per	δ18O Sea

sediment (cm)	(year BP)	(mmol/mol)	(µmol/mol)	(µmol/mol)	(˚C)	level (m)	corrected (˚C)	anomaly (˚C)	mil, PDB)	mil, PDB)	level corrected
206.75	3379					-3.88			-0.05	1.91	1.88
214.75	3434	1.143	64	53	10.51	-3.92	10.45	0.53	0.26	1.72	1.68
222.75	3488	1.042	11	23	9.31	-3.95	9.24	-0.68	0.15	1.72	1.68
230.75	3543	1.129	16	15	10.35	-4.00	10.28	0.36	0.02	1.75	1.71
238.75	3597	1.057	14	21	9.49	-4.04	9.42	-0.50	0.10	1.72	1.68
246.75	3651	1.197	18	84	11.16	-4.09	11.09	1.17	0.09	1.89	1.85
254.75	3706	1.695	98	138		-4.14			0.11	1.87	1.83
262.75	3764	1.112	22	285	10.14	-4.20	10.07	0.15	0.21	1.83	1.79
270.75	3831	1.285	84	176	12.20	-4.27	12.13	2.21	0.16	1.82	1.78
278.75	3899	1.128	129	55	10.34	-4.34	10.27	0.35	0.17	1.87	1.82
286.75	3966	1.157	85	42	10.68	-4.43	10.61	0.69	0.11	1.80	1.75
294.75	4034	1.177	64	44	10.92	-4.52	10.85	0.93	0.19	1.80	1.76
302.75	4101	2.380	740	1762		-4.61			0.14	1.72	1.68
310.75	4169	1.115	31	10	10.17	-4.71	10.10	0.18	0.04	1.89	1.84
318.75	4236	1.249	34	57	11.78	-4.82	11.70	1.78	0.14	1.70	1.65
326.75	4304	1.238	64	4188	11.64	-4.93	11.56	1.64	0.09	1.66	1.61
333.75	4363	1.098	180	68	9.98	-5.04	9.90	-0.02	0.06	1.96	1.91
341.75	4430	1.208	83	71	11.28	-5.16	11.20	1.28	0.21	2.01	1.96
349.75	4498	1.134	60	21	10.41	-5.29	10.32	0.40	0.21	1.81	1.76
357.75	4555	1.122	48	31	10.26	-5.41	10.17	0.25	0.06	1.67	1.62
365.75	4612	1.090	17	27	9.88	-5.53	9.79	-0.13	0.14	1.73	1.68
373.75	4668	1.068	16	176	9.62	-5.66	9.53	-0.39	0.12	1.75	1.69
381.75	4724	1.291	55	34	12.27	-5.79	12.18	2.26	0.09	1.92	1.86
389.75	4781	1.173	51	30	10.87	-5.92	10.77	0.85	0.12	1.72	1.66
397.75	4837	1.133	88	132	10.40	-6.06	10.30	0.38	0.10	1.91	1.85
405.75	4918	1.069	21	54	9.63	-6.27	9.53	-0.39	0.16	1.71	1.65
413.75	5009	1.119	71	145	10.22	-6.52	10.12	0.20	0.16	1.92	1.85
421.75	5100	1.204	75	299	11.24	-6.78	11.13	1.21	0.13	1.81	1.74
429.75	5191	1.140	18	422	10.47	-7.06	10.36	0.44	0.15	1.69	1.62
437.75	5282	1.270	17	133	12.02	-7.35	11.90	1.98	0.25	1.85	1.78

Appendix 3.3 continued

depth in	Age	Mg/Ca	Fe/Ca	Al/Ca	Temp	sea	Temp SL	Temp	δ13C (per	δ18O (per	δ18O Sea

sediment (cm)	(year BP)	(mmol/mol)	(µmol/mol)	(µmol/mol)	(˚C)	level (m)	corrected (˚C)	anomaly (˚C)	mil, PDB)	mil, PDB)	level corrected
445.75	5373	1.062	21	109	9.55	-7.65	9.43	-0.49	0.16	1.81	1.73
453.75	5463	1.137	71	60	10.44	-7.97	10.31	0.39	0.02	1.90	1.82
461.75	5553	1.162	18	42	10.74	-8.30	10.60	0.68	0.01	1.91	1.83
469.75	5638	1.139	80	54	10.46	-8.62	10.32	0.40	0.15	1.94	1.85
477.75	5723	1.142	55	64	10.50	-8.95	10.36	0.44	-0.02	1.87	1.78
485.75	5807	1.106	20	50	10.07	-9.30	9.92	0.00	0.03	1.79	1.70
493.75	5892	1.171	17	17	10.84	-9.66	10.69	0.77	0.16	1.98	1.88
501.75	5977					-10.04			0.24	1.77	1.67
509.75	6066	1.242	87	32	11.70	-10.44	11.53	1.61	0.34	1.79	1.68
517.75	6154	1.233	29	57	11.59	-10.86	11.41	1.49	-0.08	1.97	1.86
525.75	6242	1.176	17	28	10.91	-11.29	10.72	0.80	0.06	1.74	1.63
533.75	6331					-11.74			0.15	2.02	1.90
542.75	6430	1.113	58	22	10.15	-12.26	9.95	0.03	0.10	1.94	1.81
550.75	6515					-12.72			0.00	2.08	1.96
558.75	6569	1.290	76	32	12.26	-13.01	12.05	2.13	-0.03	1.92	1.78
566.75	6623	1.262	53	46	11.93	-13.32	11.71	1.79	0.06	1.77	1.63
574.75	6677	1.239	39	42	11.65	-13.62	11.44	1.52			
582.75	6731	1.129	53	57	10.34	-13.94	10.12	0.20	0.05	1.80	1.66
590.75	6785	1.374	49	53	13.26	-14.26	13.03	3.11	0.03	1.83	1.69
598.75	6839					-14.58			0.01	1.87	1.72
606.75	6900	1.083	53	24	9.80	-14.96	9.56	-0.36	-0.04	1.92	1.77
614.75	6964	1.023	1715	51	9.09	-15.35	8.84	-1.08	-0.03	2.07	1.92
622.75	7027					-15.75			0.02	2.01	1.85
630.75	7090	1.114	24	24	10.16	-16.16	9.90	-0.02	0.06	2.00	1.84
646.75	7217					-17.00			0.01	1.98	1.81
654.75	7280					-17.43			-0.12	1.84	1.67
662.75	7344					-17.87			-0.06	2.08	1.90
670.75	7407	1.181	41	51	10.97	-18.31	10.67	0.75	-0.13	1.73	1.55
678.75	7471	1.150	14	21	10.60	-18.76	10.30	0.38	0.11	1.96	1.77
686.75	7534	1.131	38	39	10.36	-19.22	10.05	0.13	-0.05	1.87	1.68

Appendix 3.3 continued

depth in	Age	Mg/Ca	Fe/Ca	Al/Ca	Temp	sea	Temp SL	Temp	δ13C (per	δ18O (per	δ18O Sea

sediment (cm)	(year BP)	(mmol/mol)	(µmol/mol)	(µmol/mol)	(˚C)	level (m)	corrected (˚C)	anomaly (˚C)	mil, PDB)	mil, PDB)	level corrected
688.75	7550	1.258	20	52	11.89	-19.34	11.57	1.65	0.18	1.94	1.75
696.75	7613	1.220	55	32	11.43	-19.80	11.11	1.19	-0.07	2.09	1.89
704.75	7677					-20.28			-0.06	1.92	1.71
712.75	7740	1.086	71	28	9.83	-20.76	9.50	-0.42			
720.75	7804					-21.25			-0.01	2.07	1.86
728.75	7867					-21.74			-0.06	2.17	1.95
736.75	7930					-22.24			-0.23	1.96	1.74
744.75	7994					-22.75			-0.09	2.06	1.83
752.75	8057					-23.26			-0.15	2.13	1.90
760.75	8121	1.263	82	68	11.94	-23.79	11.56	1.64	-0.04	1.89	1.65
768.75	8184	1.173	64	86	10.86	-24.31	10.47	0.55	0.04	1.88	1.64
776.75	8247	1.208	25	32	11.29	-24.85	10.89	0.97	-0.11	1.96	1.71
784.75	8323	1.200	18	50	11.20	-25.50	10.78	0.86	-0.14	2.05	1.79
792.75	8414	1.266	24	79	11.98	-26.28	11.55	1.63			
800.75	8504		97	497		-27.07			-0.19	1.85	1.58
808.75	8594	1.200	73	146	11.20	-27.88	10.75	0.83	-0.20	2.27	1.99
816.75	8684	1.219	82	42	11.41	-28.70	10.95	1.03			
824.75	8774					-29.53			-0.13	1.94	1.64
832.75	8865	1.147	123	12	10.55	-30.37	10.06	0.14			
847.75	9034	1.387	123	182	13.42	-31.98	12.90	2.98	-0.23	2.12	1.80
855.75	9084	1.320	435	212	12.62	-32.47	12.10	2.18	-0.17	2.00	1.67
863.75	9117		153	67		-32.79			-0.17	1.99	1.66
871.75	9150	1.242	100	62	11.69	-33.11	11.16	1.24	-0.26	2.03	1.70
879.75	9183	1.273	199	72	12.06	-33.43	11.52	1.60	-0.23	1.85	1.52
888.75	9219	1.326	151	63	12.69	-33.79	12.14	2.22	-0.24	1.70	1.36
895.75	9248	1.371	324	135	13.22	-34.07	12.68	2.76	-0.15	1.75	1.41
903.75	9281	1.352	1676	515	13.00	-34.40	12.45	2.53	-0.10	1.98	1.63
911.75	9313	1.147	111	187	10.55	-34.72	9.99	0.07	-0.11	1.92	1.58
919.75	9346	1.411	43	40	13.70	-35.05	13.13	3.21	-0.29	1.73	1.38
927.75	9379	1.235	119	97	11.61	-35.38	11.04	1.12	-0.13	1.81	1.45

Appendix 3.3 continued

depth in	Age	Mg/Ca	Fe/Ca	Al/Ca	Temp	sea	Temp SL	Temp	δ13C (per	δ18O (per	δ18O Sea

sediment (cm)	(year BP)	(mmol/mol)	(µmol/mol)	(µmol/mol)	(˚C)	level (m)	corrected (˚C)	anomaly (˚C)	mil, PDB)	mil, PDB)	level corrected
935.75	9411	1.406	66	78	13.65	-35.71	13.07	3.15	-0.23	1.79	1.43
943.75	9444	1.339	678	70	12.85	-36.04	12.27	2.35	-0.31	1.93	1.57
951.75	9477	1.311	439	42	12.51	-36.38	11.92	2.00	-0.23	1.78	1.42
959.75	9509	1.382	110	91	13.36	-36.71	12.77	2.85	-0.37	1.92	1.55
967.75	9542	1.389	338	247	13.44	-37.05	12.84	2.92	-0.24	1.94	1.57
975.75	9575	1.300	179	148	12.38	-37.38	11.78	1.86	-0.25	1.78	1.41
983.75	9608	1.296	239	150	12.34	-37.72	11.73	1.81	-0.23	1.98	1.60
991.75	9640	1.242	253	199	11.69	-38.06	11.07	1.15	-0.36	1.75	1.37
999.75	9673	1.260	149	229	11.90	-38.40	11.28	1.36	-0.35	1.89	1.50
1007.75	9748	1.347	115	53	12.94	-39.19	12.31	2.39	-0.30	1.77	1.38
1015.75	9826	1.302	75	77	12.40	-40.01	11.76	1.84	-0.33	1.93	1.53
1023.75	9904	1.444	125	71	14.09	-40.84	13.44	3.52	-0.29	1.94	1.53
1031.75	9982	1.233	33	71	11.59	-41.68	10.92	1.00	-0.28	2.04	1.62
1039.75	10060	1.280	302	40	12.14	-42.52	11.46	1.54	-0.26	1.84	1.41
1047.75	10138	1.265	68	493	11.97	-43.37	11.27	1.35	-0.37	2.13	1.69
1055.75	10216	1.270	124	57	12.03	-44.23	11.31	1.39	-0.36	1.73	1.28
1063.75	10294	1.346	305	123	12.92	-45.09	12.20	2.28			
1071.75	10372	1.471	452	166	14.41	-45.95	13.67	3.75	-0.28	1.88	1.42
1079.75	10450	1.307	199	101	12.47	-46.82	11.72	1.80	-0.39	1.97	1.50
1087.75	10529	1.412	136	123	13.72	-47.70	12.95	3.03			
1095.75	10607	1.448	84	106	14.14	-48.58	13.36	3.44	-0.51	2.27	1.78

Appendix 4

Appendix 4.1 Paleo density calculation and error

The $\delta^{18}O_C$ was converted to $\delta^{18}O_{SW}$ using the following equation

$$\delta^{18}O_{SW} = \delta^{18}O_C + 0.27 + (16.9 - Temp)\ 4.38^{-1}$$ [*Shackleton and Vincent*, 1978].

The error associated with the $\delta^{18}O_{SW}$ follows Cleroux et al. 2012 and is

$$\sigma\delta^{18}O_{SW} = [(\sigma\delta^{18}O_C)^2 + (\sigma temp)^2(0.23)^2]^{1/2} = [(0.07)^2 + (0.8)^2(0.23)^2]^{1/2} = \pm 0.2‰$$

Using discrete shipboard $\delta^{18}O_{SW}$ and salinity measurements from the cruise the following relationship was developed

$$\delta^{18}O_{SW} = 0.754 \pm 0.15 * sal - 26.349 \pm 5.14$$

The standard error of the salinity measurement from the water samples is ±0.2. Thus the error on the density calculation is

Absolute density error: $[(0.8)^2 + (0.2)^2]^{1/2} = \pm 0.8\ kg/m^3$

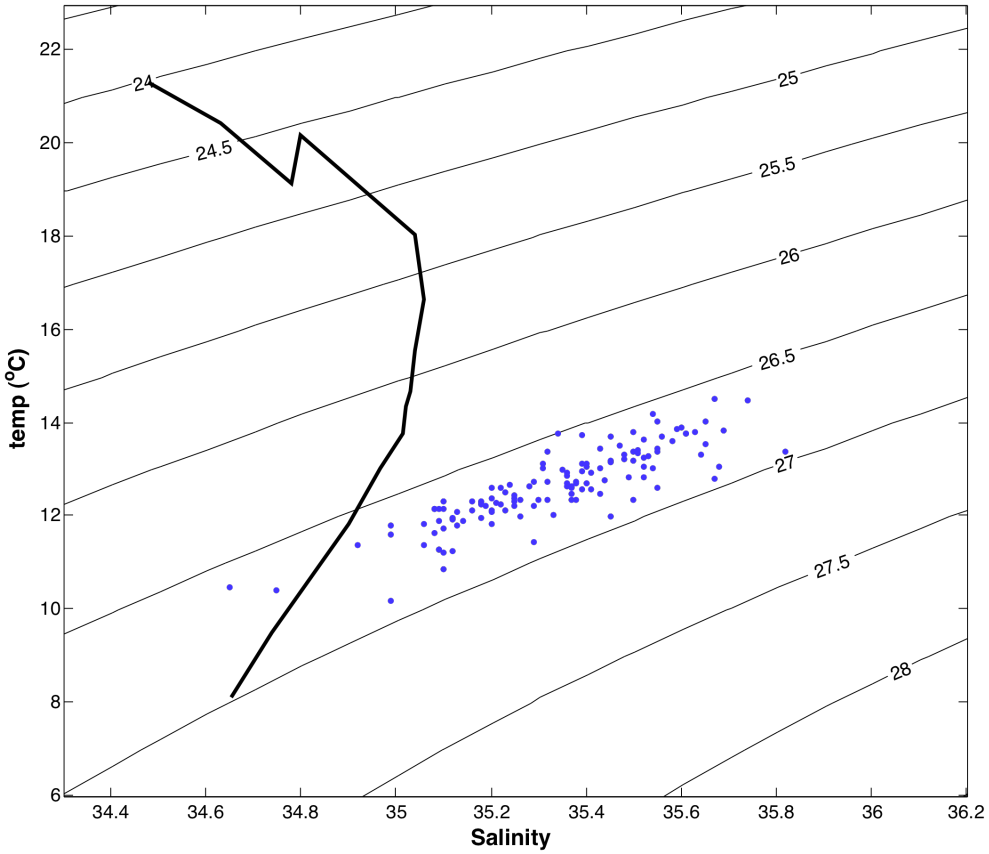

Figure 4A-1. Hydrographic (black line) and down core temperature and salinity (blue dots) data are plotted on top of density contours. The down core data plot along lines of constant density suggesting that changes in temperature are compensated by changes in salinity. The down core data are cooler and more saline than the hydrographic data.

Appendix 4.2 Alkenone data from KNR 195-5 16MC-A in Chapter 4.

depth (cm)	Age	Uk'37	SST (˚C)	C37 total (ng/g)
0.5	2004.2	0.837	23.481	
1.5	1994.61	0.843	23.640	
2.5	1985.02	0.841	23.578	
3.5	1975.42	0.841	23.591	
4.5	1965.83	0.837	23.485	
5.5	1956.24	0.845	23.711	
6.5	1946.65	0.847	23.753	7.662
7.5	1937.05	0.843	23.637	
8.5	1927.46	0.844	23.663	7.414
9.5	1917.87	0.841	23.587	7.730
10.5	1908.27	0.840	23.570	7.530
11.5	1898.68	0.844	23.688	7.801
12.5	1889.09	0.841	23.600	7.745
13.5	1879.5	0.842	23.627	7.501
14.5	1869.9	0.845	23.700	7.378
15.5	1860.31	0.844	23.683	6.947
16.5	1850.72	0.843	23.640	7.272
17.5	1841.12	0.841	23.587	7.531
18.5	1831.53	0.839	23.529	6.914
19.5	1821.94	0.841	23.600	8.007
20.5	1812.35	0.838	23.495	7.550
21.5	1802.75	0.838	23.508	7.316
22.5	1793.16	0.837	23.477	
23.5	1783.57	0.837	23.482	
24.5	1773.97	0.839	23.522	4.950
25.5	1764.38	0.839	23.517	6.172
26.5	1754.79	0.838	23.512	5.215
27.5	1745.19	0.836	23.452	7.344
28.5	1735.6	0.836	23.435	4.344
29.5	1726.01	0.834	23.370	5.651
30.5	1716.42	0.842	23.608	7.057
31.5	1706.82	0.840	23.554	7.286
32.5	1697.23	0.840	23.556	6.736
33.5	1687.64	0.838	23.504	6.536
34.5	1678.04	0.838	23.494	6.609
35.5	1668.45	0.837	23.480	5.984
36.5	1658.86	0.834	23.372	5.286
37.5	1649.27	0.839	23.521	7.307
38.5	1639.67	0.834	23.395	7.194
39.5	1630.08	0.838	23.513	7.492
40.5	1620.49	0.837	23.462	7.438

Appendix 4.2 continued

depth (cm)	Age	Uk'37	SST (˚C)	C37 total (ng/g)
41.5	1610.89	0.837	23.482	7.866
42.5	1601.3	0.839	23.524	6.982
43.5	1591.71	0.838	23.498	7.861
44.5	1582.12	0.836	23.449	7.716
45.5	1572.52	0.838	23.507	6.893
46.5	1562.93	0.832	23.332	4.272
47.5	1553.34	0.841	23.595	6.541
48.5	1543.74	0.835	23.424	7.021
49.5	1534.15	0.840	23.562	7.597
50.5	1524.56	0.841	23.597	7.104
51.5	1514.96	0.841	23.578	7.114
52.5	1505.37	0.839	23.535	7.273
53.5	1495.78	0.843	23.654	7.128
54.5	1486.19	0.845	23.717	7.672
55.5	1476.59	0.840	23.565	7.366
56.5	1467	0.842	23.631	6.023
57.5	1458.45	0.843	23.637	8.387

Appendix 4.3 Alkenone data from KNR 195-5 14GGC in Chapter 4.

depth (cm)	year	C37 ratio	SST (˚C)	C37tot (ng/g)
0.25	1603	0.835	23.42	9.94
1.25	1587	0.840	23.55	
2.25	1570	0.843	23.63	
3.25	1554	0.840	23.56	
4.25	1538	0.830	23.27	8.79
5.25	1522	0.837	23.48	
6.25	1505	0.837	23.46	
7.25	1489	0.838	23.50	8.63
8.25	1481	0.839	23.54	
9.25	1477	0.848	23.78	
10.25	1472	0.848	23.80	
11.25	1467	0.850	23.84	
12.25	1462	0.844	23.67	
13.5	1456	0.848	23.78	6.35
14.5	1451	0.843	23.66	6.79
15.5	1446	0.842	23.62	6.18
16.5	1441	0.840	23.56	7.03
17.5	1436	0.844	23.66	7.24
18.5	1432	0.840	23.56	7.02
19.5	1427	0.839	23.53	4.67
20.5	1422	0.837	23.47	7.20
21.5	1417	0.839	23.54	7.33
22.5	1412	0.837	23.46	7.48
23.5	1407	0.836	23.43	7.77
24.5	1402	0.835	23.41	7.11
25.5	1394	0.835	23.42	6.78
26.5	1383	0.836	23.45	6.99
27.5	1372	0.837	23.46	5.28
28.5	1360	0.833	23.35	6.84
29.5	1349	0.835	23.43	7.17
30.5	1338	0.836	23.44	7.12
31.5	1326	0.837	23.46	6.40
32.5	1315	0.837	23.47	6.21
33.5	1303	0.837	23.46	7.32
34.5	1292	0.836	23.46	6.60
35.5	1281	0.835	23.40	6.36
36.5	1269	0.836	23.44	6.12
37.5	1258	0.835	23.41	5.93
38.5	1247	0.835	23.41	6.11
39.5	1235	0.835	23.41	5.88
40.5	1224	0.837	23.46	6.09
41.5	1213	0.836	23.43	6.00
42.5	1201	0.832	23.34	6.09
43.5	1190	0.833	23.35	6.00
44.5	1178	0.835	23.40	7.41
45.5	1167	0.834	23.38	5.98
46.5	1156	0.833	23.35	6.01
47.5	1144	0.833	23.36	4.11
48.5	1133	0.834	23.37	6.74
49.5	1122	0.830	23.26	4.43

Appendix 4.3 continued

depth (cm)	year	C37 ratio	SST (˚C)	C37tot (ng/g)
50.5	1110	0.827	23.18	4.78
51.5	1099	0.843	23.63	4.75
52.5	1088	0.834	23.39	6.13
53.5	1076	0.826	23.14	5.35
54.5	1065	0.829	23.23	6.29
55.5	1054	0.823	23.06	2.25
56.5	1042	0.826	23.15	7.40
57.5	1031	0.830	23.26	4.63
58.5	1019	0.828	23.19	4.77
59.5	1008	0.828	23.22	4.79
60.5	997	0.826	23.13	3.93
61.5	985	0.827	23.18	6.25
62.5	974	0.828	23.22	6.45
63.5	963	0.821	23.00	6.87
64.5	951	0.825	23.12	6.19
65.5	940	0.832	23.34	5.47
66.5	929	0.829	23.24	5.87
67.5	917	0.828	23.22	5.60
68.5	906	0.825	23.11	6.54
69.5	894	0.826	23.15	2.00
70.5	883	0.829	23.22	4.03
71.5	872	0.830	23.25	8.23
72.5	860	0.824	23.08	5.75
73.5	849	0.829	23.23	6.27
74.5	838	0.831	23.28	6.38
75.5	829	0.829	23.25	5.92
76.5	822	0.828	23.21	5.91
77.5	815	0.827	23.18	5.93
78.5	809	0.822	23.04	5.43
79.5	802	0.821	23.00	4.56
80.5	796	0.820	22.97	5.59
81.5	789	0.825	23.11	5.80
82.5	782	0.824	23.08	5.50
83.5	776	0.824	23.08	5.23
84.5	769	0.822	23.03	6.20
85.5	763	0.823	23.07	5.51
86.5	756	0.825	23.10	6.73
87.5	749	0.823	23.06	5.98
88.5	743	0.825	23.11	5.45
89.5	736	0.824	23.08	6.26
90.5	729	0.824	23.10	5.39
91.5	723	0.824	23.08	5.35
92.5	716	0.819	22.95	5.44
93.5	710	0.824	23.08	5.56
94.5	703	0.823	23.05	5.27
95.5	696	0.824	23.09	5.29
96.5	690	0.822	23.02	6.06
97.5	683	0.821	22.99	5.79
98.5	677	0.823	23.06	6.07
99.5	670	0.822	23.04	6.13
100.5	663	0.822	23.02	4.85

Appendix 4.3 continued

depth (cm)	year	C37 ratio	SST (˚C)	C37tot (ng/g)
101.5	653	0.821	23.00	5.85
102.5	644	0.822	23.04	5.61
103.5	634	0.821	22.99	6.01
104.5	625	0.824	23.09	5.42
105.5	616	0.823	23.05	5.56
106.5	606	0.824	23.10	5.00
107.5	597	0.826	23.14	6.22
108.5	587	0.822	23.03	5.05
109.5	578	0.818	22.91	6.25
110.5	568	0.817	22.90	4.32
111.5	559	0.820	22.97	6.22
112.5	550	0.820	22.96	6.04
113.5	540	0.821	22.99	4.94
114.5	531	0.823	23.07	4.52
115.5	521	0.824	23.08	6.16
116.5	512	0.821	23.01	5.64
117.5	503	0.821	22.99	5.05
118.5	493	0.824	23.10	6.03
119.5	484	0.826	23.16	6.23
120.5	474	0.825	23.12	5.49
121.5	465	0.827	23.17	4.03
122.5	455	0.825	23.11	5.79
123.5	446	0.824	23.10	6.29
124.5	437	0.827	23.17	6.41
125.5	427	0.827	23.18	6.74
126.5	418	0.822	23.03	6.42
127.5	408	0.827	23.19	6.02
128.5	399	0.828	23.22	6.51
129.5	390	0.830	23.26	6.60
130.5	380	0.827	23.19	5.52
131.5	371	0.830	23.26	6.60
132.5	361	0.833	23.35	6.25
133.5	352	0.829	23.23	5.56
134.5	342	0.835	23.40	4.90
135.5	333	0.831	23.30	6.14
136.5	324	0.834	23.38	6.44
137.5	314	0.831	23.30	6.03
138.5	305	0.828	23.19	5.85
139.5	295	0.830	23.27	5.60
140.5	286	0.833	23.34	6.60
141.5	276	0.834	23.38	5.16
142.5	267	0.830	23.27	6.38
143.5	258	0.834	23.37	5.65
144.5	248	0.834	23.39	5.39
145.5	239	0.834	23.39	6.06
146.5	229	0.829	23.25	6.35
147.5	220	0.832	23.31	5.41
148.5	211	0.833	23.35	4.55
149.5	201	0.829	23.24	5.89
150.5	192	0.828	23.20	6.75
151.5	181	0.833	23.35	5.62

Appendix 4.3 continued

depth (cm)	year	C37 ratio	SST (˚C)	C37tot (ng/g)
152.5	169	0.831	23.30	5.80
153.5	157	0.830	23.28	7.03
154.5	145	0.830	23.27	6.68
155.5	133	0.829	23.25	5.78
156.5	121	0.830	23.27	5.81
157.5	109	0.828	23.20	5.82
158.5	97	0.825	23.12	4.73
159.5	84	0.826	23.14	7.00
160.5	72	0.827	23.17	6.90
161.5	60	0.826	23.14	7.11
162.5	48	0.822	23.02	6.23
163.5	36	0.825	23.12	5.84
164.5	24	0.825	23.13	6.91
165.5	12	0.825	23.12	7.13
166.5	0	0.824	23.08	6.09
167.5	-12	0.823	23.07	5.93
168.5	-24	0.824	23.08	6.20
169.5	-36	0.825	23.12	5.97
170.5	-48	0.821	22.99	5.82
171.5	-60	0.825	23.12	5.95
172.5	-72	0.825	23.11	6.27
173.5	-84	0.825	23.11	5.37
174.5	-96	0.822	23.03	5.42
175.5	-108	0.823	23.06	4.99
176.5	-121	0.819	22.95	6.10
177.5	-133	0.821	23.00	4.08
178.5	-145	0.815	22.81	6.06
179.5	-157	0.816	22.84	5.73
180.5	-169	0.818	22.91	5.39
181.5	-181	0.815	22.83	5.29
182.5	-193	0.813	22.76	5.20
183.5	-205	0.818	22.91	5.64
184.5	-217	0.815	22.84	5.26
185.5	-229	0.818	22.90	5.75
186.5	-241	0.817	22.88	4.04
187.5	-253	0.817	22.88	5.15
188.5	-265	0.811	22.70	5.52
189.5	-277	0.812	22.73	5.66
190.5	-289	0.809	22.64	4.77
191.5	-301	0.813	22.77	5.14
192.5	-314	0.818	22.92	6.47
193.5	-326	0.813	22.77	6.05
194.5	-338	0.812	22.73	6.01
195.5	-350	0.812	22.75	5.65
196.5	-362	0.819	22.95	6.26
197.5	-374	0.816	22.84	5.88
198.5	-386	0.814	22.79	6.22
199.5	-398	0.814	22.78	6.53
200.5	-410	0.817	22.89	6.22
201.5	-422	0.815	22.82	6.11
202.5	-433	0.817	22.88	5.66

Appendix 4.3 continued

depth (cm)	year	C37 ratio	SST (˚C)	C37tot (ng/g)
203.5	-445	0.813	22.78	5.45
204.5	-457	0.815	22.84	5.97
205.5	-469	0.816	22.85	5.10
206.5	-481	0.815	22.81	3.99
207.5	-492	0.813	22.77	4.22
208.5	-504	0.814	22.79	5.01
209.5	-516	0.814	22.80	6.02
210.5	-528	0.811	22.71	
211.5	-539	0.809	22.65	
212.5	-551	0.809	22.66	
213.5	-563	0.805	22.54	
214.5	-575	0.807	22.59	
215.5	-587	0.810	22.67	
216.5	-598	0.810	22.66	
217.5	-610	0.812	22.74	

Appendix 4.4 N. dutertrei data from KNR195-5 16MC-A in Chapter 4.

Depth (cm)	year	Mg/Ca (mmol/mol)	Fe/Ca (μmol/mol)	Al/Ca (μmol/mol)	Temp (˚C)	$\delta^{13}C$ (per mil, PDB)	$\delta^{18}O$ (per mil PDB)
0.5	2004	1.216	45.551	274.084	12.92	0.79	0.44
1.5	1995	1.494	7.967	19.601	15.21	0.82	0.62
2.5	1985	1.326	9.134	28.982	13.89	0.88	0.50
3.5	1975	1.432	26.666	47.394	14.74	0.92	0.46
4.5	1966	1.344	12.734	27.590	14.03	0.89	0.47
5.5	1956	1.589	26.276	32.894	15.90	0.99	0.41
6.5	1947	1.268	17.818	23.521	13.39	0.97	0.47
7.5	1937	1.286	32.844	92.824	13.55	1.11	0.49
8.5	1927	1.245	60.409	24.492	13.19	1.03	0.49
9.5	1918	1.498	21.451	23.085	15.24	1.13	0.53
10.5	1908	1.281	17.839	43.138	13.50	1.15	0.61
11.5	1899	1.188	30.860	25.102	12.66	1.21	0.51
12.5	1889	1.351	22.534	73.057	14.10	1.13	0.50
13.5	1880	1.351	22.116	36.978	14.09	1.04	0.40
14.5	1870	1.431	28.105	26.264	14.73	1.14	0.59
15.5	1860	1.172	28.201	36.533	12.52	1.14	0.62
16.5	1851	1.327	29.413	99.694	13.90	0.97	0.51
17.5	1841	1.254	37.551	37.414	13.26	1.02	0.57
18.5	1832	1.396	31.234	67.844	14.46	1.21	0.62
19.5	1822	1.391	37.595	71.149	14.42	1.18	0.48
20.5	1812	1.140	39.904	207.430	12.21	1.08	0.65
21.5	1803	1.257	43.527	24.775	13.29	1.15	0.55
22.5	1793	1.161	39.347	146.774	12.41	1.22	0.60
23.5	1784	1.358	36.083	62.056	14.15	1.16	0.53
24.5	1774	1.235	21.561	23.345	13.10	1.08	0.55
25.5	1764	1.220	47.738	66.067	12.96	1.25	0.62
26.5	1755	1.096	46.888	6.049	11.77	1.24	0.71
27.5	1745	1.174	21.023	12.343	12.53	1.25	0.63
28.5	1736	1.276	39.094	12.023	13.46	1.16	0.61
29.5	1726	1.171	45.766	27.162	12.50	1.24	0.65
30.5	1716	1.058	error	858.072	11.38	1.07	0.56
31.5	1707	1.036	3.992	16.737	11.15	1.24	0.67
32.5	1697	1.178	2.856	17.052	12.57	1.18	0.56
33.5	1688	1.308	5.742	24.289	13.74	1.20	0.68
34.5	1678	1.317	45.642	33.011	13.81	1.26	0.72
35.5	1668	1.114	18.734	47.603	11.95	1.38	0.71
36.5	1659	1.125	18.401	36.887	12.06	1.23	0.66
37.5	1649	1.067	13.340	115.222	11.47	1.25	0.66
38.5	1640	1.123	20.516	25.498	12.04	1.34	0.60
39.5	1630	1.091	error	61.839	11.71	1.23	0.54
40.5	1620	1.077	21.852	19.291	11.57	1.29	0.62

Appendix 4.4 continued

Depth (cm)	year	Mg/Ca (mmol/mol)	Fe/Ca (μmol/mol)	Al/Ca (μmol/mol)	Temp (˚C)	$\delta^{13}C$ (per mil, PDB)	$\delta^{18}O$ (per mil PDB)
41.5	1611	1.265	19.538	48.176	13.36	1.38	0.46
42.5	1601	1.172	16.272	13.865	12.52	1.27	0.57
43.5	1592	1.093	29.794	42.466	11.74	1.32	0.62
44.5	1582	1.065	9.097	29.878	11.45	1.26	0.56
45.5	1573	1.229	7.603	51.326	13.04	1.30	0.58
46.5	1563	1.173	25.872	26.013	12.53	1.35	0.54
47.5	1553	1.391	59.060	15.877	14.42	1.33	0.52
48.5	1544	1.283	72.031	12.392	13.52	1.42	0.60
49.5	1534	1.246	59.644	12.127	13.20	1.36	0.60
50.5	1525	1.135	12.332	39.380	12.16	1.39	0.59
51.5	1515	1.092	22.383	47.471	11.72	1.42	0.49
52.5	1505	1.056	9.771	591.486	11.36	1.38	0.60
53.5	1496	1.086	34.272	30.747	11.67	1.42	0.47
54.5	1486	1.000	15.292	47.884	10.75	1.35	0.60
55.5	1477	1.161	35.752	59.297	12.41	1.36	0.58
56.5	1467	1.112	48.670	56.322	11.93	1.33	0.64
57.5	1458	1.132	14.736	59.588	12.13	1.48	0.39

Appendix 4.5 N. dutertrei data from KNR 195-5 14GGC in Chapter 4.

Depth (cm)	year	Mg/Ca (mmol/mol)	Fe/Ca (μmol/mol)	Al/Ca (μmol/mol)	Temp (˚C)	$\delta^{13}C$ (per mil, PDB)	$\delta^{18}O$ (per mil PDB)
3.5	1550	1.108	55.31	39.51	11.89	1.26	0.71
4.5	1534	1.467	36.25	81.77	15.01		
5.5	1518	1.228	36.43	15.63	13.04	1.25	0.81
6.5	1501	1.080	32.16	45.59	11.61		
9.5	1475	1.218	19.20	22.82	12.95	1.29	0.70
11.5	1466	1.204	31.04	60.72	12.81	1.42	0.60
13.5	1456	1.141	48.00	4.52	12.22	1.29	0.59
15.5	1446	1.120	44.90	38.18	12.01	1.32	0.73
17.5	1436					1.34	0.72
19.5	1427	1.173	21.79	7.66	12.52	1.37	0.87
21.5	1417	1.218	119.01	20.13	12.94	1.24	0.63
23.5	1407	1.072	80.49	113.00	11.52	1.34	0.83
25.5	1394	1.175	92.43	19.15	12.54	1.30	0.56
27.5	1372	0.922	135.00	44.48	9.85	1.31	0.86
29.5	1349	0.975	57.18	51.99	10.47	1.44	0.82
31.5	1326	1.159	error	23.19	12.39	1.30	0.78
33.5	1303	1.082	81.53	148.98	11.63	1.36	0.64
35.5	1281	1.008	133.28	20.02	10.84	1.25	0.79
37.5	1258	0.974	79.39	33.06	10.46	1.31	0.53
39.5	1235	0.960	60.99	13.93	10.29	1.35	0.70
41.5	1213	1.164	50.31	20.19	12.43	1.23	0.58
43.5	1190	1.282	43.37	8.01	13.51	1.05	0.48
45.5	1167	1.116	73.39	13.90	11.97	1.27	0.82
49.5	1122	1.312	63.00	35.94	13.77	1.25	0.56
51.5	1099	1.153	139.96	44.91	12.33	1.24	0.64
53.5	1076	1.148	130.92	80.49	12.29	1.16	0.45
55.5	1054	1.184	88.70	13.91	12.63	1.35	0.85
57.5	1031	1.217	65.82	38.45	12.93	1.28	0.76
59.5	1008	1.190	52.81	21.30	12.68	1.31	0.62
61.5	985	1.125	39	15	12.06	1.26	0.84
63.5	963	1.048	76.72	51.72	11.27	1.22	0.69
65.5	940	1.229	34.14	12.22	13.04	1.30	0.64
67.5	917	1.081	86.92	71.53	11.61	1.32	0.61
69.5	894	1.134	43.60	131.19	12.15	1.40	0.52
71.5	872	1.027	50.20	18.21	11.05	1.27	0.58
73.5	849	1.192	58.34	39.44	12.71	1.38	0.62
75.5	829	1.304	48.51	43.41	13.70	1.27	0.55
77.5	815	1.146	107.56	52.49	12.27	1.31	0.59
79.5	802	1.289	250.30	152.12	13.57	1.33	0.55
81.5	789	1.257	77.19	33.11	13.29	1.35	0.52
85.5	763	1.111	76.90	91.11	11.92	1.31	0.48
87.5	749	1.157	86.95	269.52	12.37	1.35	0.53

Appendix 4.5 continued

Depth (cm)	year	Mg/Ca (mmol/mol)	Fe/Ca (μmol/mol)	Al/Ca (μmol/mol)	Temp (˚C)	$\delta^{13}C$ (per mil, PDB)	$\delta^{18}O$ (per mil PDB)
89.5	736	1.254	74.78	25.28	13.26	1.30	0.73
91.5	723	1.160	177.72	156.45	12.40	1.37	0.53
93.5	710	1.051	189.69	278.69	11.31	1.29	0.53
95.5	696	1.058	33.95	114.01	11.38	1.37	0.61
97.5	683	1.369	399.19	234.42	14.24	1.29	0.63
99.5	670	1.094	223.96	25.35	11.75		
101.5	653	1.384	110.80	42.07	14.36	1.39	0.49
103.5	634	1.188	161.19	37.87	12.66	1.47	0.53
105.5	616	1.204	239.46	68.75	12.81	1.28	0.59
107.5	597	1.274	87.45	26.78	13.44	1.35	0.49
109.5	578	1.354	79.99	55.75	14.12	1.32	0.65
111.5	559	1.223	66.45	46.94	12.99	1.62	0.31
113.5	540	1.246	95.71	178.03	13.20	1.34	0.52
115.5	521	1.469	208.54	190.74	15.02	1.43	0.38
117.5	503	1.262	140.82	83.80	13.34	1.40	0.46
119.5	484	1.047	63.30	88.90	11.27	1.35	0.50
121.5	465	1.147	50.57	9.37	12.28	1.34	0.52
123.5	446	1.119	84.84	30.45	12.00	1.25	0.50
125.5	427	1.148	66.96	56.91	12.28	1.31	0.50
127.5	408	1.310	52.82	6.86	13.75	1.34	0.49
129.5	390	1.224	99.58	8.73	13.00	1.41	0.37
131.5	371	1.248	66.49	75.96	13.21	1.27	0.58
133.5	352	1.126	365.40	78.28	12.07	1.19	0.65
135.5	333	1.247	101.99	23.54	13.21	1.37	0.45
137.5	314	1.117	79.53	108.05	11.98	1.41	0.56
139.5	295	1.211	error	23.51	12.87	1.37	0.58
141.5	276	1.260	375.52	25.20	13.32	1.42	0.49
143.5	258	1.308	245.96	35.75	13.73	1.34	0.79
145.5	239	1.214	error	69.18	12.91	1.36	0.56
147.5	220	1.251	error	65.65	13.24	1.48	0.67
149.5	201	1.185	228.35	24.38	12.64	1.39	0.53
151.5	181	1.117	102.35	18.33	11.98	1.31	0.67
153.5	157	1.190	80.31	20.47	12.69	1.33	0.62
155.5	133	1.043	error	84.78	11.22	1.39	0.61
157.5	109	1.219	143.68	51.62	12.95	1.37	0.60
159.5	84	1.295	error	72.01	13.62	1.31	0.60
161.5	60	1.194	198.24	34.61	12.72	1.25	0.61
163.5	36	1.102	334.47	42.09	11.83	1.30	0.65
165.5	12	1.100	118.06	32.94	11.81	1.35	0.45
167.5	-12	1.167	44.96	23.28	12.46	1.32	0.60
169.5	-36	1.092	106.95	36.07	11.73	1.19	0.61
171.5	-60	1.260	58.92	15.43	13.32	1.26	0.56
173.5	-84	1.088	error	24.49	11.68	1.31	0.52

Appendix 4.5 continued

Depth (cm)	year	Mg/Ca (mmol/mol)	Fe/Ca (μmol/mol)	Al/Ca (μmol/mol)	Temp (˚C)	$\delta^{13}C$ (per mil, PDB)	$\delta^{18}O$ (per mil PDB)
175.5	-108	1.366	error	99.15	14.22	1.27	0.61
177.5	-133	1.181	error	74.20	12.60	1.26	0.51
179.5	-157	1.207	error	46.40	12.84	1.27	0.56
181.5	-181	1.205	error	45.32	12.83	1.26	0.67
183.5	-205	1.298	147.87	38.27	13.65	1.29	0.55
185.5	-229	1.247	205.42	33.49	13.20	1.23	0.63
187.5	-253	1.287	340.95	93.81	13.55	1.27	0.56
189.5	-277	1.151	235.73	61.83	12.31	1.34	0.52
191.5	-301	1.080	110.09	27.50	11.61	1.32	0.61
193.5	-326	1.178	62.68	395.66	12.57	1.31	0.49
195.5	-350	1.198	52.38	19.73	12.76	1.38	0.53
197.5	-374	1.114	92.83	24.18	11.95	1.39	0.57
201.5	-422	1.175	error	68.94	12.55	1.26	0.67
203.5	-445	1.141	150.42	106.27	12.21	1.35	0.49
205.5	-469	1.155	135.69	133.10	12.35	1.44	0.64
207.5	-492	1.209	167.48	88.65	12.86	1.47	0.87
209.5	-516	1.324	293.25	42.85	13.87	1.41	0.74
211.5	-539	1.315	200.71	32.01	13.79	1.32	0.48
213.5	-563	1.310	212.51	25.80	13.75	1.38	0.36
215.5	-587	1.296	254.71	372.24	13.63	1.35	0.55
217.5	-610	1.249	202.19	44.77	13.22	1.29	0.48

Appendix 5

Appendix 5.1 All trace metal ratios for samples and replicates in Chapter 5.

Samples highlighted in blue were eliminated due to high Fe/Ca and Al/Ca. Samples highlighted in yellow were eliminated because the values were 2σ higher than the mean of the surrounding 10 values.

core	depth in sediment (cm)	Year CE	Mg/Ca (mmol/mol)	Fe/Ca (μmol/mol)	Al/Ca (μmol/mol)
31MC	2.5	1987	2.96	39	179
31MC	3.5	1982	2.35	36	93
31MC	4.5	1978	3.01	43	69
31MC	5.5	1973	2.99	76	170
31MC	6.5	1968	2.62	41	86
31MC	7.5	1964	2.44	15	94
31MC	8.5	1959	2.96	24	80
31MC	9.5	1955	2.17	29	187
31MC	10.5	1950	2.00	21	144
31MC	11.5	1946	2.54	error	56
31MC	12.5	1941	2.27	44	200
31MC	13.5	1937	2.36	60	112
31MC	14.5	1932	3.20	error	677
31MC	15.5	1928	2.56	error	131
31MC	16.5	1923	2.32	30	99
31MC	17.5	1918	2.74	91	145
31MC	18.5	1914	2.01	83	149
31MC	19.5	1909	2.00	128	139
31MC	20.5	1905	2.49	74	194
31MC	21.5	1900	2.00	31	47
31MC	22.5	1896	2.64	47	121
31MC	24	1888	2.33	36	67
31MC	25.5	1877	2.43	120	55
31MC	26.5	1870	2.32	111	90
31MC	28.5	1857	2.69	66	71
31MC	29.5	1850	1.97	104	173
31MC	30.5	1843	2.55	119	105
31MC	31.5	1836	2.10	106	199
31MC	32.5	1829	2.34	131	149
31MC	33.5	1822	2.34	336	210
31MC	34.5	1815	2.51	67	72
31MC	35.5	1808	2.75	107	38
31MC	36.5	1801	2.22	79	71
31MC	37.5	1794	2.48	137	33
31MC	38.5	1788	2.75	215	177
31MC	39.5	1781	2.79	96	92
31MC	40.5	1774	2.29	89	58
31MC	41.5	1767	2.72	85	59
31MC	43	1756	2.53	234	125
31MC	44.5	1746	2.89	68	29
31MC	45.5	1739	2.63	38	76
31MC	47	1729	2.37	116	175
31MC	48.5	1718	2.03	71	148
31MC	49.5	1711	2.41	80	71

core	depth in sediment (cm)	Year CE	Mg/Ca (mmol/mol)	Fe/Ca (μmol/mol)	Al/Ca (μmol/mol)
34GGC	1	1620	2.36	38	110
34GGC	2.5	1615	2.50	56	121
34GGC	5	1606	2.64	78	937
34GGC	7	1599	2.06	26	65
34GGC	9	1592	2.82	97	157
34GGC	11	1584	2.62	60	103
34GGC	13.5	1573	2.82	412	710
34GGC	15	1567	2.40	145	240
34GGC	16	1563	2.61	47	126
34GGC	19	1551	2.00	79	187
34GGC	21	1542	2.11	47	39
34GGC	22	1538	2.14	92	54
34GGC	23	1534	2.21	122	98
34GGC	25	1526	2.60	32	38
34GGC	25	1526	2.36	205	192
34GGC	27	1517	2.30	96	50
34GGC	27	1517	2.84	79	49
34GGC	29	1509	2.21	88	16
34GGC	29	1509	2.34	308	138
34GGC	31	1501	2.01	214	57
34GGC	31	1501	2.57	91	141
34GGC	33	1492	1.92	98	239
34GGC	33	1492	2.46	64	966
34GGC	35	1484	2.09	274	94
34GGC	35	1484	2.56	67	8
34GGC	39	1468	2.92	399	344
34GGC	39	1468	2.66	149	39
34GGC	41	1459	2.39	298	238
34GGC	43	1451	3.56	122	109
34GGC	43	1451	2.17	204	46
34GGC	45	1443	3.18	638	605
34GGC	45	1443	2.80	305	100
34GGC	47	1434	2.15	231	389
34GGC	49	1426	3.34	320	143
34GGC	49	1426	2.77	207	107
34GGC	51	1418	2.29	270	112
34GGC	52	1414	2.99	264	185
34GGC	53	1409	2.48	306	524
34GGC	55	1401	2.60	396	35
34GGC	57	1393	2.49	148	57
34GGC	59	1385	2.82	256	23
34GGC	61	1376	2.06	247	
34GGC	61	1376	3.01	93	106
34GGC	63	1368	2.47	452	105
34GGC	65	1360	2.19	562	64
34GGC	67	1351	2.37	490	107
34GGC	69	1343	2.13	290	92
34GGC	71	1335	2.56	252	21
34GGC	73	1326	2.41	295	194
34GGC	75	1318	2.53	379	184
34GGC	77	1310	2.48	259	147

Appendix 5.1 continued

core	depth in sediment (cm)	Year CE	Mg/Ca (mmol/mol)	Fe/Ca (mmol/mol)	Al/Ca (mmol/mol)
34GGC	81	1293	2.63	212	571
34GGC	83	1285	2.91	588	225
34GGC	85	1277	2.52	207	66
34GGC	87	1268	2.57	227	207
34GGC	87	1268	2.33	201	102
34GGC	89	1260	2.77	177	1397
34GGC	91	1252	2.70	242	155
34GGC	93	1243	2.99	295	1503
34GGC	95	1235	2.20	140	1193
34GGC	97	1227	2.34	220	319
34GGC	99	1219	2.83	316	190
34GGC	101	1210	2.81	539	375
34GGC	103	1202	2.50	167	243
34GGC	105	1190	2.94	672	868
34GGC	107	1178	2.71	379	438
34GGC	109	1167	2.60	668	353
34GGC	111	1155	2.65	421	668
34GGC	113	1143	3.02	467	1633
34GGC	115	1131	2.72	297	468
34GGC	117	1119	2.64	326	266
34GGC	119	1108	2.62	241	332
34GGC	121	1096	2.57	313	1462
34GGC	123	1084	3.32	694	696
34GGC	125	1072	3.16	642	644
34GGC	127	1060	2.89	106	178
34GGC	129	1049	2.91	390	340
34GGC	131	1037	3.22	612	693
34GGC	131	1037	2.49	192	536
34GGC	133	1025	2.39	353	390
34GGC	133	1025	2.45	187	210
34GGC	135	1013	2.91	692	463
34GGC	135	1013	1.96	78	84
34GGC	137	1002	3.13	334	628
34GGC	137	1002	2.87	273	386
34GGC	139	990	2.87	457	451
34GGC	139	990	2.17	239	432
34GGC	141	978	2.49	612	687
34GGC	141	978	2.60	106	134
34GGC	143	966	2.45	604	380
34GGC	143	966	2.31	136	90
34GGC	145	954	2.79	507	290
34GGC	145	954	2.19	566	202
34GGC	147	943	3.14	349	628
34GGC	147	943	2.19	214	204
34GGC	149	931	3.53	1034	1151
34GGC	151	919	2.58	379	1369
34GGC	151	919	2.03	163	137
34GGC	153	907	2.36	206	117
34GGC	155	895	2.50	235	55
34GGC	157	884	2.01	192	111
34GGC	159	872	2.22	71	210
34GGC	161	860	2.25	380	503

Appendix 5.1 continued

core	depth in sediment (cm)	Year CE	Mg/Ca (mmol/mol)	Fe/Ca (mmol/mol)	Al/Ca (mmol/mol)
34GGC	163	848	2.40	150	183
34GGC	165	836	3.74	633	1074
34GGC	165	836	2.11	236	994
34GGC	167	825	2.27	302	183
34GGC	167	825	1.75	199	485
34GGC	169	813	2.07	469	1528
34GGC	169	813	1.92	177	120
34GGC	171	801	2.80	206	1835
34GGC	171	801	2.02	148	69
34GGC	173	789	1.85	161	655
34GGC	173	789	2.37	281	119
34GGC	175	777	2.95	379	626
34GGC	175	777	2.34	407	180
34GGC	177	766	2.58	490	802
34GGC	177	766	2.21	158	75
34GGC	179	754	2.26	266	141
34GGC	181	742	2.71	292	372
34GGC	181	742	2.13	130	106
34GGC	183	730	3.51	842	1063
34GGC	183	730	2.07	190	312
34GGC	185	718	2.67	778	1695
34GGC	185	718	2.03	613	301
34GGC	187	707	2.50	991	541
34GGC	187	707	1.82	149	194
34GGC	189	695	2.15	329	595
34GGC	189	695	2.09	236	152
34GGC	191	683	2.43	671	722
34GGC	191	683	2.28	774	248
34GGC	193	671	2.52	488	618
34GGC	195	659	2.89	592	451
34GGC	197	648	2.34	603	687
34GGC	201	626	3.24	597	786
34GGC	203	618	2.82	563	993
34GGC	205	611	3.96	2175	2361
34GGC	207	603	2.82	1182	1608
34GGC	209	595	3.92	687	3306
34GGC	211	587	3.09	1395	1399
34GGC	213	580	2.85	369	853
34GGC	215	572	2.84	465	956
34GGC	217	564	2.70	177	337
34GGC	219	556	2.56	302	1602
34GGC	221	549	2.48	204	408
34GGC	221	549	2.03	213	203
34GGC	223	541	2.51	154	281
34GGC	223	541	2.36	820	238
34GGC	225	533	2.65	486	1037
34GGC	225	533	2.59	542	1747
34GGC	227	525	2.93	365	1593
34GGC	227	525	2.84	817	816
34GGC	229	518		411	541
34GGC	229	518	2.67	360	74

Appendix 5.1 continued

core	depth in sediment (cm)	Year CE	Mg/Ca (mmol/mol)	Fe/Ca (mmol/mol)	Al/Ca (mmol/mol)
34GGC	231	510	2.12	132	126
34GGC	231	510	2.31	208	112
34GGC	233	502	1.84	252	319
34GGC	233	502	2.36	295	84
34GGC	235	494	2.45	207	885
34GGC	235	494	2.25	634	52
34GGC	235	494	2.25	634	52
34GGC	237	487	2.12	298	251
34GGC	237	487	2.05	317	414
34GGC	239	479	2.50	468	1062
34GGC	241	471	2.27	397	2595
34GGC	241	471	2.42	864	99
34GGC	243	463	2.29	152	645
34GGC	243	463	2.11	212	208
34GGC	245	456	1.84	159	179
34GGC	245	456	2.35	555	133
34GGC	247	448	1.82	142	478
34GGC	247	448	2.11	537	297
34GGC	249	440	2.37	79	135
34GGC	251	432	2.20	663	923
34GGC	253	425	2.21	332	1207
34GGC	255	417	2.94	780	1089
34GGC	257	409	2.25	241	289
34GGC	259	401	2.67	1153	332
34GGC	261	394	2.00	132	147
34GGC	263	386	2.31	301	411
34GGC	265	378	2.02	226	127
34GGC	267	370	2.43	482	744
34GGC	269	363	2.13	227	337
34GGC	271	355	2.13	282	542
34GGC	273	347	2.51	676	3816
34GGC	275	339	2.51	848	528
34GGC	277	332	1.81	265	142
34GGC	279	324	2.01	279	106
34GGC	281	316	3.34	1136	1215
34GGC	283	308	2.77	835	1701
34GGC	285	301	2.48	500	1265

Appendix 5.2 N. dutertrei data used for figure 5-3. The highlighted values from appendix 1 were removed and replicates were averaged together. The temperature anomaly was calculated from the average from between 1850-1880, 21.4˚C

core	depth in sediment (cm)	Age	Mg/Ca Averaged	Temp (˚C)	Temp anomaly (˚C)	δ13C (PDB, per mil)	δ18O (PDB, per mil)
31MC	2.5	1987	2.96	24.0	2.6		
31MC	3.5	1982	2.35	21.5	0.1		
31MC	4.5	1978	3.01	24.2	2.8		
31MC	5.5	1973	2.99	24.2	2.7		
31MC	6.5	1968	2.62	22.7	1.3		
31MC	7.5	1964	2.44	21.9	0.5	0.85	-1.91
31MC	8.5	1959	2.96	24.0	2.6	0.79	-1.92
31MC	9.5	1955	2.17	20.6	-0.8	0.97	-1.88
31MC	10.5	1950	2.00	19.7	-1.7		
31MC	11.5	1946	2.54	22.4	0.9		
31MC	12.5	1941	2.27	21.1	-0.3	1.02	-1.72
31MC	13.5	1937	2.36	21.5	0.1		
31MC	14.5	1932					
31MC	15.5	1928	2.56	22.4	1.0	1.19	-1.90
31MC	16.5	1923	2.32	21.3	-0.1		
31MC	17.5	1918	2.74	23.2	1.8	1.16	-1.90
31MC	18.5	1914	2.01	19.7	-1.7	1.29	-1.63
31MC	19.5	1909	2.00	19.7	-1.7		
31MC	20.5	1905	2.49	22.1	0.7	1.25	-1.85
31MC	21.5	1900	2.00	19.7	-1.7	1.42	-1.57
31MC	22.5	1896	2.64	22.8	1.4		
31MC	24	1888	2.33	21.4	0.0	1.35	-2.02
31MC	25.5	1877	2.43	21.8	0.4	1.07	-2.24
31MC	26.5	1870	2.32	21.3	-0.1		
31MC	28.5	1857	2.69	23.0	1.6	1.17	-2.08
31MC	29.5	1850	1.97	19.5	-1.9	1.15	-1.44
31MC	30.5	1843	2.55	22.4	1.0		
31MC	31.5	1836	2.10	20.2	-1.2	1.28	-1.82
31MC	32.5	1829	2.34	21.4	0.0		
31MC	33.5	1822	2.34	21.4	0.0		
31MC	34.5	1815	2.51	22.2	0.8	1.34	-1.63
31MC	35.5	1808	2.75	23.2	1.8	1.31	-1.85
31MC	36.5	1801	2.22	20.8	-0.6		
31MC	37.5	1794	2.48	22.1	0.7		
31MC	38.5	1788	2.75	23.2	1.8		
31MC	39.5	1781	2.79	23.4	2.0		
31MC	40.5	1774	2.29	21.2	-0.2		
31MC	41.5	1767	2.72	23.1	1.7		
31MC	43	1756	2.53	22.3	0.9	1.29	-1.70
31MC	44.5	1746	2.89	23.8	2.4		
31MC	45.5	1739	2.63	22.7	1.3		
31MC	47	1729	2.37	21.6	0.2	1.43	-1.90
31MC	48.5	1718	2.03	19.9	-1.5		
31MC	49.5	1711	2.41	21.8	0.4		

Appendix 5.2 continued

core	depth in sediment (cm)	Age	Mg/Ca Averaged	Temp (˚C)	Temp anomaly (˚C)	δ13C (PDB, per mil)	δ18O (PDB, per mil)
34GGC	1	1620	2.36	21.5	0.1		
34GGC	2.5	1615	2.50	22.2	0.8		
34GGC	5	1606	2.64	22.8	1.3		
34GGC	7	1599	2.06	20.0	-1.4		
34GGC	9	1592	2.82	23.5	2.1		
34GGC	11	1584	2.62	22.7	1.3		
34GGC	13.5	1573	2.82	23.5	2.1		
34GGC	15	1567	2.40	21.7	0.3		
34GGC	16	1563	2.61	22.7	1.2		
34GGC	19	1551	2.00	19.7	-1.7		
34GGC	21	1542	2.11	20.3	-1.1	1.37	-1.86
34GGC	22	1538	2.14	20.4	-1.0	1.34	-1.75
34GGC	23	1534	2.21	20.8	-0.6		
34GGC	25	1526	2.48	22.1	0.7	1.38	-1.89
34GGC	27	1517	2.57	22.5	1.1	1.45	-1.93
34GGC	29	1509	2.28	21.1	-0.3	1.34	-2.17
34GGC	31	1501	2.29	21.2	-0.2	1.35	-1.84
34GGC	33	1492	2.19	20.7	-0.7		
34GGC	35	1484	2.32	21.4	-0.1	1.41	-1.50
34GGC	37	1476				1.40	-1.65
34GGC	39	1468	2.79	23.4	2.0	1.41	-1.93
34GGC	41	1459	2.39	21.7	0.3	1.34	-1.69
34GGC	43	1451	2.17	20.6	-0.8	1.33	-2.17
34GGC	45	1443	2.99	24.2	2.8	1.15	-2.03
34GGC	47	1434	2.15	20.5	-0.9	1.26	-1.98
34GGC	49	1426	3.06	24.4	3.0	1.27	-2.19
34GGC	51	1418	2.29	21.2	-0.2	1.13	-1.77
34GGC	52	1414	2.99	24.2	2.7		
34GGC	53	1409	2.48	22.1	0.7	1.09	-2.04
34GGC	55	1401	2.60	22.6	1.2	1.38	-2.00
34GGC	57	1393	2.49	22.1	0.7	1.38	-1.68
34GGC	59	1385	2.82	23.5	2.1		
34GGC	61	1376	2.54	22.3	0.9	1.14	-1.63
34GGC	63	1368	2.47	22.0	0.6	1.29	-1.82
34GGC	65	1360	2.19	20.7	-0.7	1.50	-1.65
34GGC	67	1351	2.37	21.6	0.2	1.17	-2.30
34GGC	69	1343	2.13	20.4	-1.0	1.24	-2.08
34GGC	71	1335	2.56	22.4	1.0	1.09	-2.20
34GGC	73	1326	2.41	21.7	0.3	1.32	-1.96
34GGC	75	1318	2.53	22.3	0.9	1.56	-1.90
34GGC	77	1310	2.48	22.1	0.6		
34GGC	79	1302				1.18	-2.44
34GGC	81	1293	2.63	22.7	1.3	0.98	-2.38
34GGC	83	1285	2.91	23.8	2.4		
34GGC	85	1277	2.52	22.3	0.8		
34GGC	87	1268	2.45	21.9	0.5		
34GGC	89	1260	2.77	23.3	1.9		
34GGC	91	1252	2.70	23.0	1.6	1.18	-2.00
34GGC	93	1243	2.99	24.2	2.8	1.25	-2.07

Appendix 5.2 continued

core	depth in sediment (cm)	Age	Mg/Ca Averaged	Temp (˚C)	Temp anomaly (˚C)	δ13C (PDB, per mil)	δ18O (PDB, per mil)
34GGC	95	1235	2.20	20.8	-0.6	1.36	-2.13
34GGC	97	1227	2.34	21.4	0.0	1.23	-1.79
34GGC	99	1219	2.83	23.5	2.1	1.09	-2.10
34GGC	101	1210	2.81	23.5	2.1	1.47	-1.83
34GGC	103	1202	2.50	22.2	0.8	1.24	-2.12
34GGC	105	1190	2.94	24.0	2.6	1.15	-2.28
34GGC	107	1178	2.71	23.1	1.7	1.20	-2.24
34GGC	109	1167	2.60	22.6	1.2	1.15	-2.15
34GGC	111	1155	2.65	22.8	1.4		
34GGC	113	1143	3.02	24.3	2.9	1.20	-2.04
34GGC	115	1131	2.72	23.1	1.7	1.05	-2.11
34GGC	117	1119	2.64	22.8	1.4	1.13	-2.39
34GGC	119	1108	2.62	22.7	1.3	1.14	-2.40
34GGC	121	1096	2.57	22.5	1.1	1.19	-2.24
34GGC	123	1084	3.32	25.3	3.9		
34GGC	125	1072	3.16	24.8	3.4	1.28	-2.08
34GGC	127	1060	2.89	23.8	2.3	1.00	-2.34
34GGC	129	1049	2.91	23.8	2.4	0.99	-2.34
34GGC	131	1037	2.86	23.6	2.2	1.04	-2.26
34GGC	133	1025	2.42	21.8	0.4	1.09	-1.82
34GGC	135	1013	2.44	21.9	0.5	1.07	-2.18
34GGC	137	1002	3.00	24.2	2.8	0.92	-2.22
34GGC	139	990	2.52	22.3	0.8	1.05	-2.17
34GGC	141	978	2.55	22.4	1.0	1.33	-2.08
34GGC	143	966	2.38	21.6	0.2	1.29	-2.08
34GGC	145	954	2.49	22.1	0.7	1.11	-1.96
34GGC	147	943	2.66	22.9	1.5	1.11	-2.03
34GGC	149	931				1.28	-2.25
34GGC	151	919	2.30	21.3	-0.1	1.14	-2.12
34GGC	153	907	2.36	21.5	0.1	1.11	-2.13
34GGC	155	895	2.50	22.2	0.7	1.16	-2.16
34GGC	157	884	2.01	19.8	-1.6	1.03	-2.07
34GGC	159	872	2.22	20.9	-0.6	1.11	-2.08
34GGC	161	860	2.25	21.0	-0.4	1.15	-2.18
34GGC	163	848	2.40	21.7	0.3	1.29	-2.00
34GGC	165	836	2.11	20.3	-1.1	1.15	-2.28
34GGC	167	825	2.01	19.8	-1.6		
34GGC	169	813	2.00	19.7	-1.7	1.11	-1.85
34GGC	171	801	2.41	21.8	0.3		
34GGC	173	789	2.11	20.3	-1.1		
34GGC	175	777	2.64	22.8	1.4	1.21	-1.62
34GGC	177	766	2.39	21.7	0.3	1.15	-1.89
34GGC	179	754	2.26	21.0	-0.4	1.13	-2.18
34GGC	181	742	2.42	21.8	0.4	1.25	-1.48
34GGC	183	730				1.26	-1.88
34GGC	185	718	2.35	21.5	0.1	1.08	-2.09
34GGC	187	707	2.16	20.5	-0.9	1.09	-2.18
34GGC	189	695	2.12	20.3	-1.1	1.10	-2.00
34GGC	191	683	2.35	21.5	0.1	1.16	-1.77
34GGC	193	671	2.52	22.3	0.8	0.92	-1.53
34GGC	195	659	2.89	23.8	2.4	1.12	-2.07

Appendix 5.2 continued

core	depth in sediment (cm)	Age	Mg/Ca Averaged	Temp (˚C)	Temp anomaly (˚C)	δ13C (PDB, per mil)	δ18O (PDB, per mil)
34GGC	197	648	2.34	21.4	0.0	1.12	-1.76
34GGC	199	636				0.82	-2.23
34GGC	201	626	3.24	25.0	3.6	1.09	-1.97
34GGC	203	618	2.82	23.5	2.1	1.23	-2.00
34GGC	205	611				1.20	-1.96
34GGC	207	603				1.00	-2.09
34GGC	209	595				1.08	-2.00
34GGC	211	587				0.83	-2.28
34GGC	213	580	2.85	23.6	2.2	0.94	-2.34
34GGC	215	572	2.84	23.6	2.2	1.05	-2.06
34GGC	217	564	2.70	23.0	1.6	1.27	-2.13
34GGC	219	556	2.56	22.4	1.0	1.10	-2.37
34GGC	221	549	2.26	21.0	-0.4	0.82	-2.43
34GGC	223	541	2.43	21.9	0.5	1.11	-2.19
34GGC	225	533	2.62	22.7	1.3	1.09	-2.47
34GGC	227	525	2.89	23.8	2.4	1.04	-2.30
34GGC	229	518				0.88	-2.08
34GGC	231	510	2.22	20.8	-0.6	1.13	-2.09
34GGC	233	502	2.10	20.3	-1.2	1.04	-1.90
34GGC	235	494	2.35	21.5	0.1	1.04	-2.22
34GGC	237	487	2.08	20.1	-1.3	0.90	-2.02
34GGC	239	479				0.99	-1.99
34GGC	241	471	2.35	21.5	0.1	0.84	-2.23
34GGC	243	463	2.20	20.8	-0.6	1.09	-2.11
34GGC	245	456	2.10	20.2	-1.2	0.97	-2.02
34GGC	247	448	1.97	19.5	-1.9	1.16	-2.06
34GGC	249	440	2.37	21.6	0.2	0.92	-1.98
34GGC	251	432	2.20	20.7	-0.7	1.01	-2.16
34GGC	253	425	2.21	20.8	-0.6	1.22	-2.21
34GGC	255	417				1.09	-2.06
34GGC	257	409	2.25	21.0	-0.4	1.14	-2.16
34GGC	259	401				1.12	-1.96
34GGC	261	394	2.00	19.7	-1.7	1.12	-2.00
34GGC	263	386	2.31	21.3	-0.1		
34GGC	265	378	2.02	19.8	-1.6		
34GGC	267	370	2.43	21.8	0.4	1.24	-2.33
34GGC	269	363	2.13	20.4	-1.0	1.16	-1.97
34GGC	271	355	2.13	20.4	-1.0	1.07	-2.16
34GGC	273	347				1.12	-1.96
34GGC	275	339	2.51	22.2	0.8	0.96	-2.30
34GGC	277	332	1.81	18.6	-2.8		
34GGC	279	324	2.01	19.8	-1.6		
34GGC	281	316				1.16	-2.04
34GGC	283	308	2.77	23.3	1.9	1.20	-1.97
34GGC	285	301	2.48	22.1	0.7	1.27	-1.68

Appendix 5.3. Interpolated temperature and $\delta^{18}O_C$ values used to calculate $\delta^{18}O_{sw}$ using the N. dutertrei equation from Farmer et al. 2007.

year	temp	δ18Oc (PDB, per mil)	δ18Osw (SMOW, per mil)
360	20.39	-2.04	-0.63
370	21.77	-2.31	-0.63
380	20.16	-2.19	-0.83
390	20.48	-2.05	-0.63
400	20.24	-1.97	-0.59
410	20.99	-2.15	-0.62
420	20.86	-2.12	-0.62
430	20.76	-2.18	-0.69
440	21.56	-1.98	-0.35
450	19.71	-2.05	-0.77
460	20.52	-2.07	-0.64
470	21.37	-2.21	-0.61
480	21.90	-1.99	-0.29
490	20.73	-2.11	-0.63
500	20.59	-1.99	-0.54
510	20.87	-2.09	-0.59
520	23.17	-2.15	-0.19
530	23.15	-2.40	-0.45
540	21.95	-2.22	-0.51
550	21.30	-2.42	-0.83
560	22.71	-2.26	-0.40
570	23.45	-2.08	-0.07
625	24.81	-1.97	0.30
635	23.55	-2.21	-0.18
645	21.87	-1.87	-0.17
655	22.88	-1.95	-0.06
665	23.06	-1.82	0.11
675	22.02	-1.61	0.12
685	21.31	-1.81	-0.22
695	20.33	-2.00	-0.61
705	20.51	-2.15	-0.72
715	21.20	-2.12	-0.55
725	21.56	-1.97	-0.34
735	21.69	-1.72	-0.06
745	21.60	-1.66	-0.01
755	21.10	-2.15	-0.60
765	21.65	-1.91	-0.25
775	22.56	-1.68	0.16
840	20.71	-2.19	-0.72
850	21.60	-2.03	-0.38
860	21.02	-2.18	-0.65
870	20.88	-2.10	-0.59
880	20.09	-2.07	-0.72
890	21.07	-2.12	-0.58
900	21.91	-2.15	-0.44
910	21.46	-2.13	-0.51

Appendix 5.3 continued

year	temp	δ18Oc (PDB, per mil)	δ18Osw (SMOW, per mil)
920	21.33	-2.13	-0.54
930	22.02	-2.24	-0.51
940	22.70	-2.08	-0.22
950	22.40	-1.99	-0.18
960	21.88	-2.02	-0.32
970	21.86	-2.08	-0.38
980	22.35	-2.10	-0.30
990	22.30	-2.17	-0.39
1000	23.94	-2.21	-0.11
1010	22.52	-2.19	-0.36
1020	21.84	-1.98	-0.28
1030	22.58	-2.00	-0.17
1040	23.70	-2.28	-0.22
1050	23.83	-2.34	-0.26
1060	23.76	-2.34	-0.27
1070	24.57	-2.13	0.10
1080	25.14	-2.13	0.21
1090	23.90	-2.20	-0.10
1100	22.56	-2.30	-0.46
1110	22.71	-2.40	-0.54
1120	22.79	-2.38	-0.50
1130	23.06	-2.14	-0.21
1140	23.98	-2.06	0.05
1150	23.41	-2.07	-0.07
1160	22.71	-2.12	-0.26
1170	22.73	-2.18	-0.31
1180	23.19	-2.25	-0.29
1190	23.96	-2.28	-0.17
1200	22.48	-2.15	-0.33
1210	23.43	-1.84	0.16
1220	23.19	-2.05	-0.09
1230	21.19	-1.92	-0.35
1240	22.74	-2.10	-0.23
1250	23.26	-2.02	-0.04
1300	22.46	-2.43	-0.62
1310	22.06	-2.17	-0.43
1320	22.16	-1.91	-0.16
1330	22.04	-2.06	-0.33
1340	21.16	-2.12	-0.57
1350	21.40	-2.26	-0.66
1360	20.73	-1.66	-0.18
1370	22.11	-1.77	-0.03
1380	22.87	-1.64	0.25
1390	22.60	-1.67	0.17
1400	22.55	-1.96	-0.12
1410	22.37	-2.02	-0.23
1420	22.05	-1.88	-0.15
1430	22.53	-2.09	-0.26
1440	22.99	-2.01	-0.10
1450	20.98	-2.15	-0.63

Appendix 5.3 continued

year	temp	δ18Oc (PDB, per mil)	δ18Osw (SMOW, per mil)
1460	21.83	-1.71	-0.02
1470	23.09	-1.85	0.09
1480	21.86	-1.57	0.12
1490	20.89	-1.62	-0.11
1500	21.16	-1.83	-0.27
1510	21.28	-2.14	-0.56
1520	22.34	-1.92	-0.13
1530	21.38	-1.83	-0.23
1540	20.37	-1.82	-0.42
1730	21.71		
1740	22.87	-1.78	0.11
1750	23.21	-1.72	0.24
1760	22.58	-1.77	0.07
1770	22.22	-1.82	-0.06
1780	23.21	-1.64	0.32
1790	22.81	-1.80	0.09
1800	21.07	-1.48	0.06
1810	22.97	-2.12	-0.21
1820	21.66	-2.19	-0.53
1830	21.26	-2.22	-0.64
1840	21.50	-2.15	-0.52
1850	19.65	-2.08	-0.82
1860	22.58	-2.00	-0.16
1870	21.38	-1.85	-0.25
1880	21.72	-1.71	-0.04
1890	21.77	-1.58	0.10
1900	19.87	-1.76	-0.46
1910	19.69	-1.72	-0.45
1920	22.56	-1.90	-0.07
1930	22.19	-1.87	-0.11
1940	21.23	-1.74	-0.16
1950	19.82	-1.82	-0.53
1960	23.73	-1.92	0.15

Appendix 6: DSDP 262 Stratigraphy

Deep Sea Drilling Project (DSDP) hole 262 is located on the axis of the Timor Trough south of West Timor (10˚52'S, 123˚51'E). The *Globigerinoides ruber* $\delta^{18}O$ record of was generated in order to better constrain the original biostratigraphy by Heirtzel et al. [1974] which appeared in the initial core report The $\delta^{18}O$ stratigraphy constrains the age model through Marine Isotope Stage (MIS) 7, however, dolomitization of the sediments affects $\delta^{18}O$ values preventing the use of $\delta^{18}O$ stratigraphy below ~250 m (Figure 5.1). The $\delta^{18}O$ stratigraphy shows extended interglacials with high sedimentation rates during MIS 5 (~270 cm/kyr) and MIS 7 (~135 cm/kyr), whereas the glacial periods are extremely condensed relative to the interglacials. Both the Holocene and stage 5e are truncated by a turbidite. Using the $\delta^{18}O$ stratigraphy the 4.5 m graded sand occurs during MIS 5d and has an age of ~110 ka. The last appearance of *Pseudoemiliania lacunose*, which is based upon decrease abundance at ~270 m depth, corresponds to ~460 ka, suggesting substantially reduced sedimentation rates after 220 m. Heirtzler et al. [1974] reported the first occurrence of *Globorotalia truncatulinoides* at 337 m, which is now dated at 1.93 Ma [*Lourens*, 2004; *Wade et al.* 2011]. The biostratigraphy will appear in a paper titled, "A sedimentary record of arc-continental plateau collision at Timor in the Banda Arc" by Brandon Duffy.

References

Heirtzler, J. R. and Scientific Party, 1974. DSDP Reports and Publications, *Initial Reports*, College Station, TX (Ocean Drilling Program). doi:10.2973/dsdp.proc.27.105.1974

Lourens, L. J. (2004). Revised tuning of Ocean Drilling Program Site 964 and KC01B (Mediterranean) and implications for the δ18O, tephra, calcareous nannofossil, and geomagnetic reversal chronologies of the past 1.1 Myr.*Paleoceanography*, *19*(3).

Wade, B. S., Pearson, P. N., Berggren, W. A., & Pälike, H. (2011). Review and revision of Cenozoic tropical planktonic foraminiferal biostratigraphy and calibration to the geomagnetic polarity and astronomical time scale. *Earth-Science Reviews*, *104*(1), 111-142.

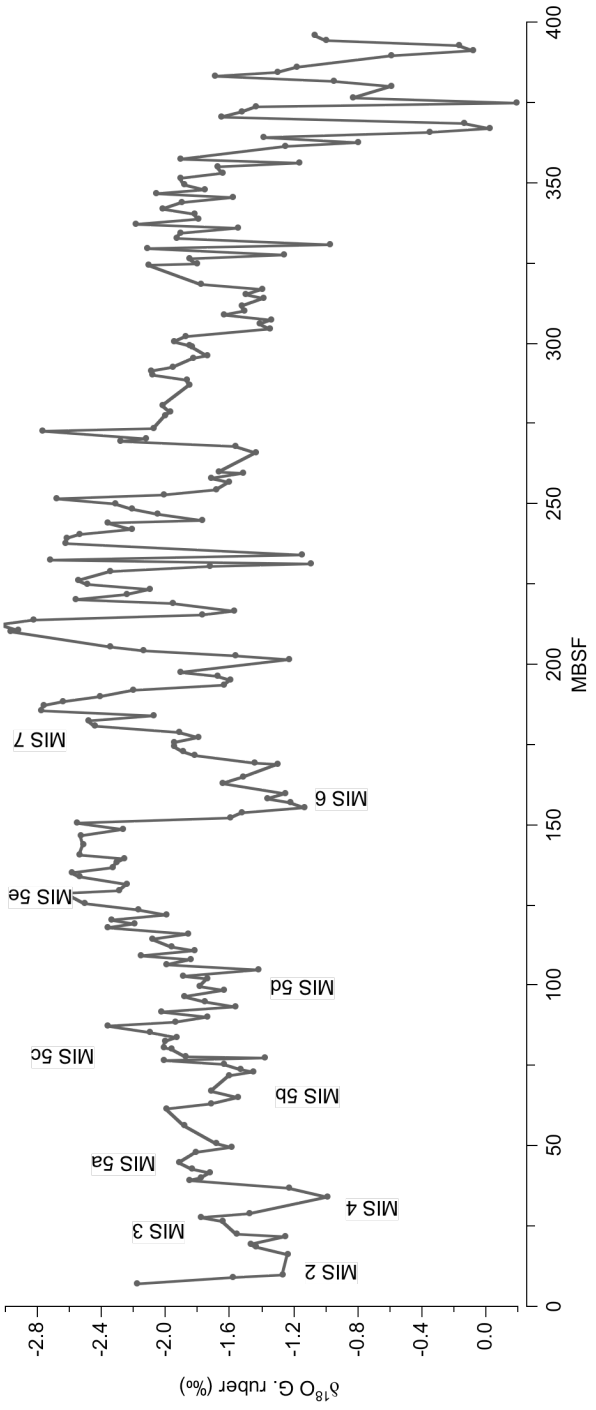

Figure 6A.1. The $\delta^{18}O$ of *G. ruber* from DSDP 262 with the MIS shown until MIS 7, after which the $\delta^{18}O$ is unreliable due to dolomitization.

Appendix 7: Additional Figures

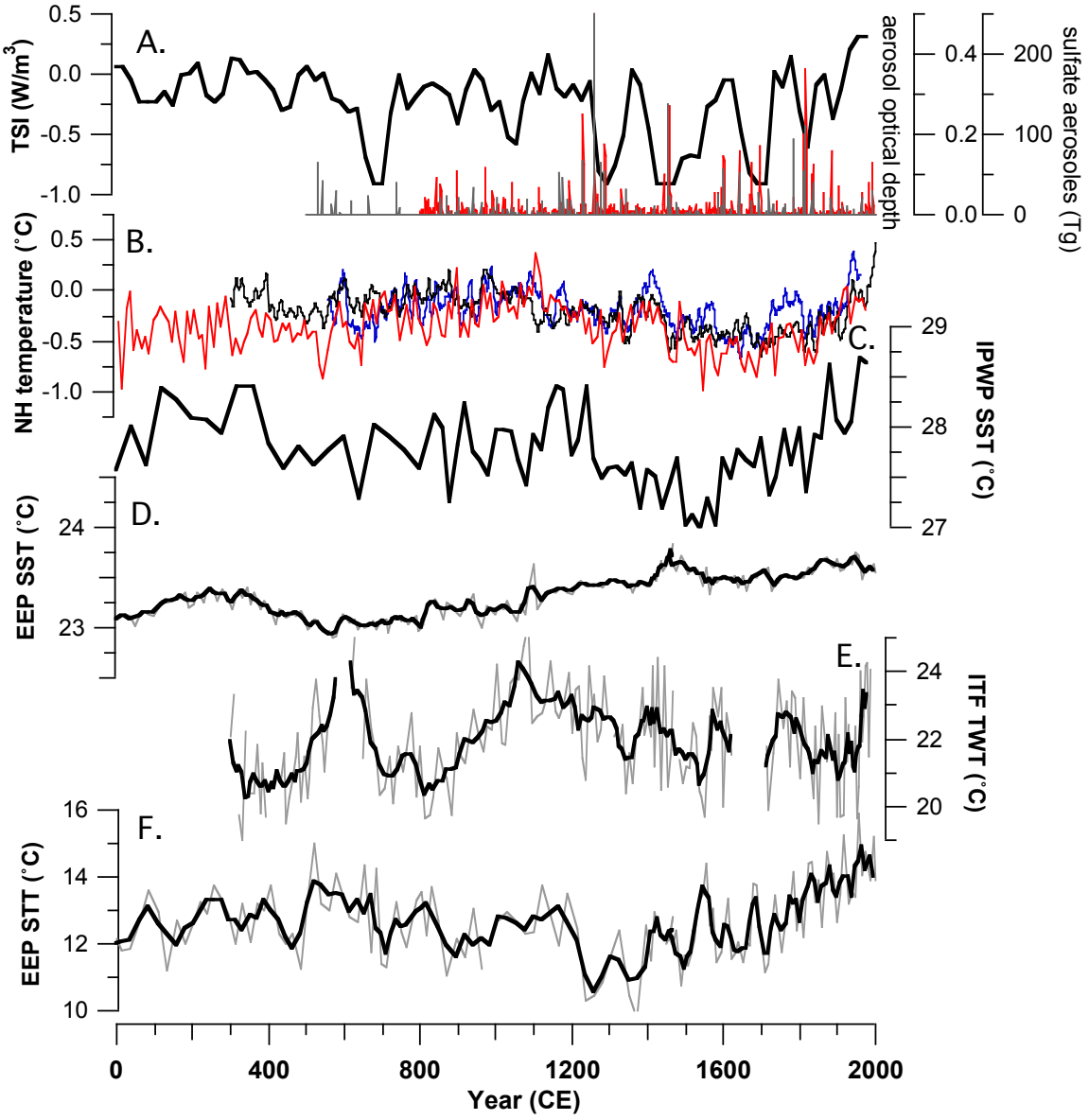

Figure 7A.1 The records from the last 2,000 years generated for this dissertation are plotted along with (A) radiative forcings, TSI [*Steinhilber et al.* 2011] and volcanic eruption reconstructions [*Gao et al.* 2009 (grey) *Crowley and Unterman* 2013 (red)], (B) Northern Hemisphere temperatures anomalies [*Mann et al.* 2008 (black), *Moberg et al.* 2005 (red), *Hegerl et al.* 2007 (blue)] and (C) Indo-Pacific-Warm-Pool SST [*Oppo et al.* 2009]. (D) The Eastern Equatorial Pacific SST, (E) Indonesian Thoughflow thermocline water temperatures (TWT) and (F) EEP subthermocline temperatures (STT)

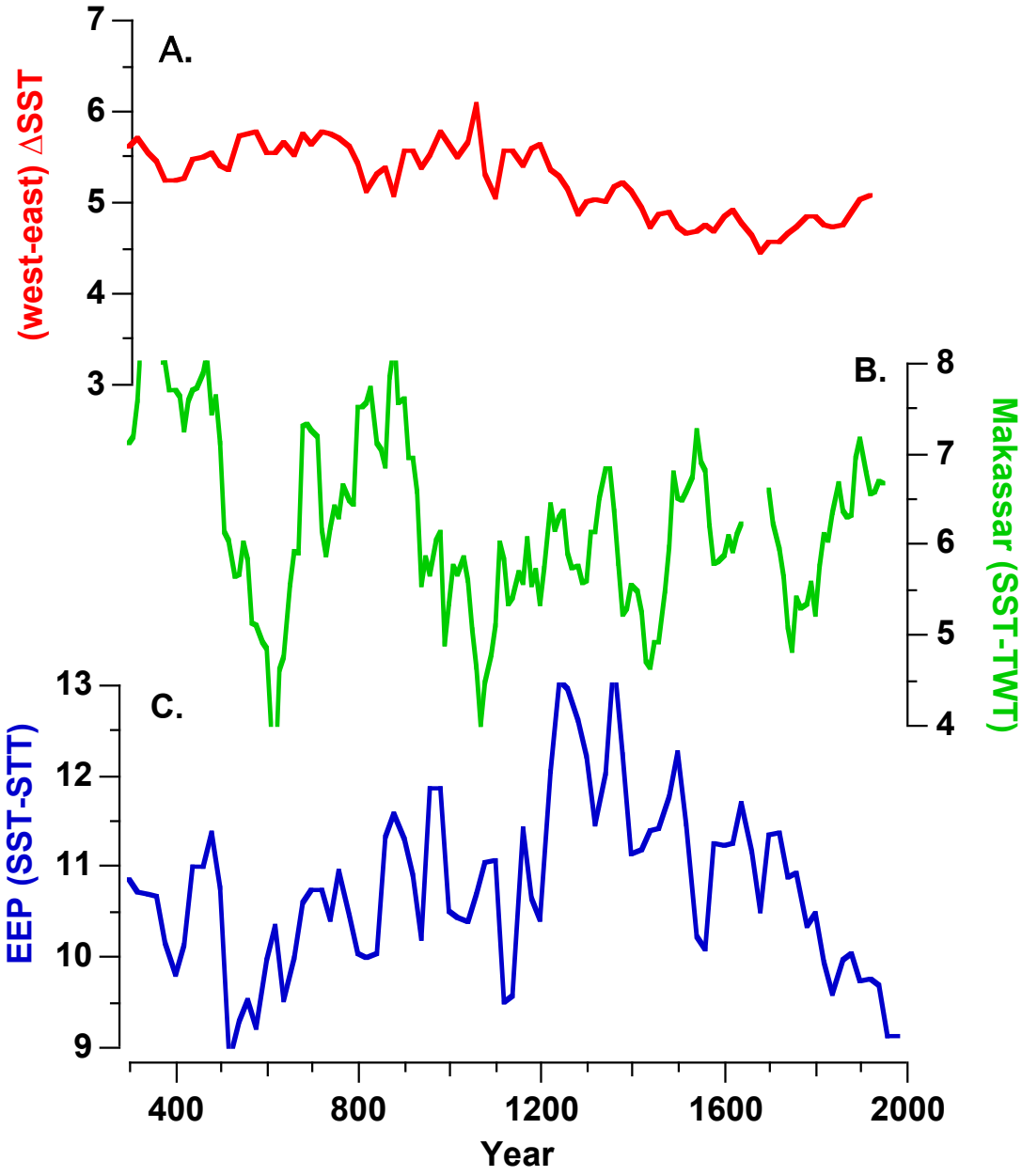

Figure 7A.2 (A) The difference between SST from the IPWP and SST from the EEP (Chapter 4). (B) The difference between SST [*Oppo et al.* 2009] and thermocline temperatures (75-100 m) in the Makassar Strait (Chapter 5) (C) The difference between SST and subthermocline (100-130 m) temperatures in EEP (Chapter 4).

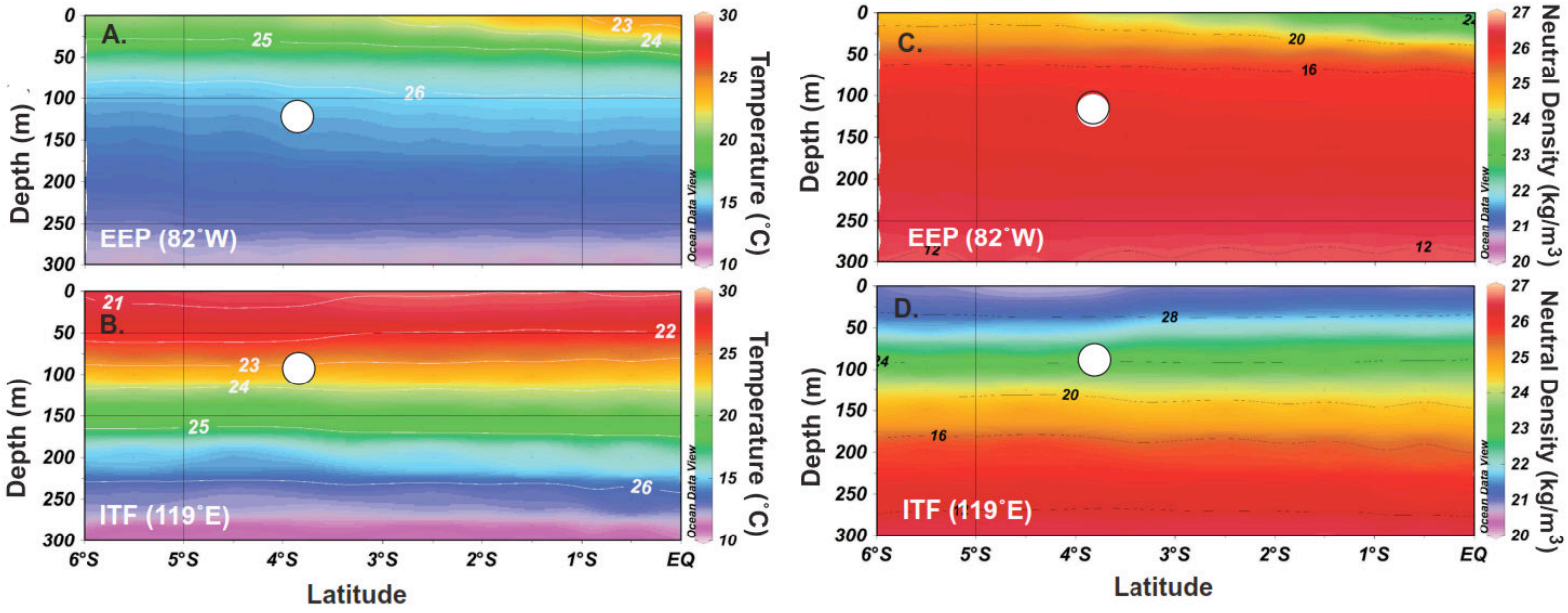

Figure 7A.3 The four panels are density and temperature profiles near the (A,C) EEP and (B,D) ITF core sites to illustrate how the calcification depth of *N.dutertrei* varies based on these properties at the two locations. (A, B) Neutral density contours are plotted on temperature sections and (C, D) temperature contours are plotted on top of density sections. The white circles are plotted at the approximate latitude of the core sites and depth at which *N. dutertei* is thought to calcify